GALVANIC SYNTHESIS AND *IN SITU* SPECIATION OF METHANE OXIDATION CATALYSTS

A Thesis Submitted to the

College of Graduate and Postdoctoral Studies

In Partial Fulfillment of the Requirements for the Degree of

Master of Science

in the Department of Chemistry

University of Saskatchewan

Saskatoon

By

WILLIAM GWYN BARRETT

Permission to Use

The included work is presented in partial fulfillment of the Master of Science Program for the University of Saskatchewan. I agree that the Libraries of this University may present this work freely for the public. Furthermore, Dr. Robert Scott, or, in his absence, the Head of the Department or Dean of the College from which this work is derived has my permission to allow this thesis to be used or copied for scholarly purposes, at their discretion. This thesis can not be published or presented for financial gain without my permission. All uses of this thesis require recognition to the original author as per accepted academic honesty protocol.

Requests to copy or utilize this material may be addressed to:

Head

Department of Chemistry

University of Saskatchewan

170 Thorvaldson Building, 110 Science Place

Saskatoon, Saskatchewan, S7N 5C9

Canada

Or

Dean

College of Graduate and Postdoctoral Studies

University of Saskatchewan

116 Thorvaldson Building, 110 Science Place

Saskatoon, Saskatchewan S7N 5C9

Canada

Abstract

The focus of this thesis is the methane oxidation reaction, catalyzed by Pd nanoparticles on a metal oxide support. This thesis presents a synthesis strategy for dispersing Pd catalysts on metal oxide supports and *in situ* speciation of these catalysts, therefore, will be presented in two parts. Firstly, a unique synthetic process will be presented for the synthesis of metal nanoparticles on metal oxide supports: galvanic deposition. Following this, *in situ* X-ray Absorption Spectroscopy (XAS) analysis of supported Pd nanoparticles is performed in order to determine speciation of both the metal and support during methane oxidation reactions.

In Chapter 2 a synthetic procedure for the synthesis of Pd on SnO is presented and the resulting materials are thoroughly characterized. The synthetic procedure is termed galvanic deposition and involves a spontaneous galvanic reaction between the Pd salt and metal oxide. A case study will be presented targeting a Pd on SnO_2 catalyst, synthesized via Pd(II) salts and SnO. The case study is finalized with the characterization of galvanically synthesized Pd/SnO_2 catalysts at competitive dispersions with modern literature. The chapter will include an argument for the use of the technique, a discussion of the specific problems for the technique and will finish with an exploration of the generality of the technique.

Chapter 3 discusses *in situ* XAS work performed at the Canadian Light Source on Pd-based catalysts for methane oxidation reactions. *In situ* Pd speciation on a variety of metal oxide supports is followed at temperatures up to 450 ^{o}C. The Pd, PdO, and $Pd(OH)_2$ equilibrium is of interest as the presence of PdO is required for methane oxidation, the presence of Pd is beneficial for methane oxidation and the presence of $Pd(OH)_2$ has been shown to passivate methane oxidation catalysts. Direct measurements of $Pd(OH)_2$ *in situ* have remained elusive in literature. This work presents

speciation and quantification of Pd, PdO, and $Pd(OH)_2$ on three diverse Pd on metal oxide systems at both the Pd K and L_3 edges. Quantification allows comparison and analysis of Pd speciation *in situ* and thereby provides a tool necessary to further understand metal-metal oxide structure-property relationships.

Acknowledgments

A variety of people assisted the writing of this thesis, and all their support is appreciated. First and foremost, Dr. Robert Scott provided the opportunity to attempt my Master of Science of which I am eternally grateful. Furthermore, he has continuously assisted, mentored and labored over my work. Without him, this thesis wouldn't be possible.

Dr. Natalia Semagina, of the Chemical Engineering Department at the University of Alberta, has been a collaborator on this thesis. Her group, specifically Dr. Jing Shen, a post doctoral fellow, and Somaye Nasr, a PhD candidate, have been fundamental in much of the work. Their engineering perspective enlightened this project.

These people provided professional help, were instrumental in the completion of this work and their assistance and guidance is appreciated:

- Dr. Yongfeng Hu, Dr. Qunfeng Xiao of the SXRMB beamline and Dr. Ning Chen and Dr. Weifeng Chen of the HXMA beamline at the Canadian Light Source have been instrumental in the experimental design and procedures in much of the *in situ* work presented.
- Dr. Danielle Covelli, Laboratory Manager at the Saskatchewan Structural Sciences Center has been extremely helpful in the X-Ray Photoelectron Spectroscopy experiments and very receptive to discussions about the XPS work presented.
- Rhonda Sobchishin of the Western College of Veterinary Medicine, Transmission Electron Microscopy lab assisted with TEM imaging and provided advice and help in the TEM images included in this document.

- Xin Zhang of Simon Fraser University's 4D labs was fundamental in the HAADF and EDX imaging presented.

The University of Saskatchewan staff, colleagues and faculty have all greatly influenced this document and I have great appreciation for their teaching, administration and friendship. Dr. Adrian Clarke, Dr. Valerie MacKenzie and Dr. Alexandra Bartole-Scott have guided my growth throughout this process and their experiences, anecdotes and rationalizations have centered my work.

Dr. Robert Scott's Group, particularly Brandon Chivers, have assisted in day to day activities and helped rationalize and discuss ideas frequently. Their help will never be forgotten, and their friendship will be cherished.

Lastly, the last two years of my life have been largely influenced by those people outside academia. Specifically, I am grateful for the patience and support of Kaitlyn Cummer, my partner throughout my time in academia.

Table of Contents

List of Tables

List of Figures

List of Abbreviations

a%	Atomic Percent
AR	As Received
BE	Binding Energy
CLS	Canadian Light Source
DFT	Density Functional Theory
E	Energy
EDX	Energy Dispersive X-Ray Spectroscopy
EDX	Energy Dispersive X-Ray Spectroscopy
EELS	Electron Energy Loss Spectroscopy
EELS	Electron Energy Loss Spectroscopy
EWS	Electron Withdrawing Species
EXAFS	Extended X-Ray Absorption Fine Structure
GD	Galvanic Deposition
GRR	Galvanic Replacement Reaction
HAADF	High angle annular dark field imaging
HAADF	High Angle Annular Dark Field
HXMA	Hard X-Ray Micro-Analysis
KE	Kinetic Energy
LCF	Linear Combination Fitting
LMCT	Ligand to Metal Charge Transfer
M/MO	Metal supported on Metal Oxide
MLCT	Metal Ion to Ligand Charge Transfer

MO	Metal Oxide
MS	Mass Spectrometry
NP	Nanoparticle
PCW	Powder Cell for Windows
Pd/Al_2O_3	Palladium supported on Aluminium Oxide
Pd/CoO_x	Palladium Supported on Cobalt Oxide
Pd/SnO	Palladium supported on Tin(II) Oxide
Pd/SnO_2	Palladium supported on Tin(IV) Oxide
PXRD	Powder X-Ray Diffraction
SMSI	Strong Metal Support Interactions
SXRMB	Soft X-Ray Microcharacterization Beamline
TEM	Transmission Electron Microscopy
TGA	Thermogravimetric Analysis
TPR	Temperature Programmed Reduction
TPR-MS	Temperature Programmed Reduction characterized by Mass Spectrometry
UHV	Ultra-High Vacuum
w/w%	Weight-Weight Percent
WMSI	Weak Metal Support Interactions
XANES	X-Ray Absorption Near Edge Structure
XAS	X-Ray Absorption Spectroscopy

Chapter 1

1.1 Introduction

This chapter will contain a discussion of specific areas of the research in order to provide a baseline of fundamental knowledge to the reader such that they can more critically analyze the science thereafter. Each subchapter presents current understanding of the subject to the extent that the information pertains to the reader with respect to the thesis.

Catalysts are continually more prevalent and necessary in society. The synthesis, characterization, design and *in situ* speciation of these particles is paramount for the efficient use of materials. Chapter 1 will introduce the reader to the topic, and provide the information required to understand and critique this thesis. Chapter 1 will include a discussion about natural gas as the cleanest hydrocarbon for future energy systems and will then point out the difficulty with natural gas and solutions to solve this issue responsibly. Following is a discussion about catalysts, their synthesis and nuances in catalyst design, with a focus on methane oxidation catalysts. This precedes discussion about challenges specific to Pd catalysts in methane oxidation environments and solutions to these adversities. The chapter will then discuss characterization methods with an emphasis on *in situ* techniques and their relevance to the subsequent chapters.

1.2 Combustion of Natural Gas

Energy resource predictions for the future vary, however, current perception is that renewables alone will not be able to supply the world with sufficient energy in the future.[1] Hydrocarbons will most likely be a part of both the short and long term energy strategy, and thus responsible use of hydrocarbon fuels is paramount. Natural gas is a mixture of volatile hydrocarbons, primarily methane (75 %) but also contains ethane, propane, butane and other chemicals at various concentrations depending on where and how the resource is collected.[2] It is the most responsible of carbon fuel sources due to the efficiency of its combustion and has been implemented in power plants and natural gas vehicles.[3] Although energy requirements in the United States and Canada continually increase, energy related carbon dioxide emissions have gone down since natural gas power plants have become more prevalent. This fact in the United States is correlated to a dramatic decrease in the use of inefficient hydrocarbon based fuel sources such as coal.[3] In Canada this is due to replacing coal and oil fuels with natural gas.[4]

As with most hydrocarbon combustion techniques carbon dioxide is produced during the combustion of methane and released to the environment. Concentrations of greenhouse gases in the environment is a global problem which many are trying to fix in a variety of ways. The unique difficulty with natural gas as a fuel source is that methane released to the environment has a 21 times greater greenhouse potential than carbon dioxide.[5] Greenhouse potential, or global warming potential, is calculated based on a variety of variables including the energy storage of a molecule, the time in which it can persist in the atmosphere, and its concentration.[6] Exhaust gases from natural gas combustion can contain low amounts of methane below flammability limits. Therefore, protocols are required to ensure flue gas does not release methane to the environment.

1.3 Methane oxidation Catalysts

One way to prevent the release of natural gas to the environment is the oxidation of methane, often referred to as catalytic combustion. A variety of catalysts exist for the catalytic combustion of methane including metals such as Pb, Mn, Pt, and Pd and other systems such as perovskites.[7, 8] The expected operating environments for these catalysts is adverse and a variety of challenges have to be overcome:[9]

- Low operating temperatures (<500 ^{o}C)
- Large amounts of water vapour
- Excess of oxygen (*i.e.* methane burning in lean conditions)
- Large amounts of carbon dioxide
- Low concentrations of methane (500-1000 ppm)
- Presence of SO_x and NO_x compounds

Pd-based catalysts have generated the most interest primarily for their relatively low ignition temperatures (the temperature at which catalytic activity begins) and high stability.[7] Therefore, this thesis will primarily be focusing on Pd based systems, and the difficulties of this specific system will be expanded on and discussed below.

1.3.1 Utilization of Nanoparticle Properties

Although no clear correlation between Pd particle size and reaction rate has been established (when normalized for surface Pd available), Pd oxidation of methane is almost exclusively done by Pd nanoparticles supported on a metal oxide.[9, 10] Notably, in other systems, when corrected for available active sites, there are correlations between particle size and catalyst activity.[11] This does

not seem to be the case for Pd. However, nanoparticle use is consistent in the field for one primary reason: size efficiency. The active region of any catalyst is the region able to interact with the substrate, which, in the case of a heterogenous catalyst, is the surface of the catalyst. Therefore, exploitation of the high surface area to volume ratio of nanoparticles is paramount in that it dramatically increases the sites available for catalysis and dramatically reduces the amount of wasted material. This is a fundamental rule of geometry known as the Square-Cube law, which simply points out that as a shape expands the surface area grows by the square and the volume grows by the cube.[12]

1.3.2 Modern Pd Nanoparticle Synthesis

Pd is notable for its catalytic activity and is commonly utilized as a nanomaterial, to compensate for its high cost. Synthesis of Pd nanoparticles is typically bottom up. Although, top down processes exist, *i.e.* techniques that start with large particles and making them smaller, bottom up processes are more common. Chemical reduction of metal salts in the presence of stabilizing ligands have been a common methodology for modern nanoparticle synthesis, such as the widely known Brust-Shiffrin method (which was originally used for thiolate stabilized Au nanoparticle synthesis).[13, 14] These processes start with a Pd salt and reduce that salt in the presence of an organic capping ligand. Two primary variables exist: the reducing agent and the capping ligand, with many possible species to use in both categories.[15]

- Reducing Agent: The reducing agent reduces the metal salt. Use of different reducing agent species, ranging from carbon monoxide to sodium borohydride, and the concentration of the reducing agent, manipulates the rate the salt is reduced. Reduced metal atoms will bond

to one another in solution, thereby a system with only a reducing agent will form large, non-uniform metal particles.[16]

- Capping Ligand: The capping ligand passivates the particles, preventing aggregation. Different capping ligands range in type of bonding (covalent or electrostatic), size of the ligand (polymers to low molecular weight molecules), and added function (stabilization and/or particle shape control).[16, 17]

The manipulation of the reducing agent and capping ligand gives control of the final size (and possibly functionality and shape) of the nanoparticle.[17] Typically, low concentrations of strong reducing agents coupled with high concentrations of high affinity capping ligands produce small nanoparticles.

The catalytic properties of nanoparticles are dependent on the size,[18] shape,[19] and composition.[20]

- Size has multiple impacts on activity. As discussed previously nanoparticles inherently are more of an efficient use of materials due to the Square-Cube law. However, as particles get smaller other phenomena due to particle size can also be beneficial to activity. Khoa *et al.* showed one effect of particle size influencing catalytic performance by utilizing ultra-violet photoelectron spectroscopy of Au nanoparticles supported on graphene oxide.[11] They found that smaller Au nanoparticles on graphene oxide reduced the work function of the graphene oxide when comparing 5, 20, and 40 nm Au nanoparticle samples. Reducing the work function means electrons are more readily liberated from the catalyst and therefore catalytic activity was seen to be a function of particle size, with an increasing rate of reduction of o-nitroaniline seen as the Au particle size decreases, even after the rate was normalized by the number of active sites.[11]

- Shape is another important parameter for two different reasons: surface area to volume ratio and exploitation of shape dependent phenomena. As stated previously, surface area to volume ratio increases as particles become smaller, due to the Square-Cube law. Morphology also has influence on the surface area to volume ratio. For example, an atomically thin sheet morphology would have significantly larger surface area to volume ratio compared to spherical morphology. This is merely a geometric consideration. Specific morphologies can also expose nuanced active sites, as presented by Radha *et al.*.[21] They synthesized tetrahedral, cubic, and "near spherical" Pt nanoparticles at comparable sizes, ~ 5 nm, and found varying activation energies for the redox reaction between hexacyanoferrate(III) and thiosulfate ions dependant on particle morphology. They associated these differences based on the amount of edges and corners present in the particles. These edges and corners are more readily perturbed thereby creating defect sites which in some catalytic systems are more catalytically active. As predicted the more facets the morphology contained the lower the activation energy.
- Composition of a nanoparticle is impactful specifically regarding the ligand species and its affinity to the metal. Affinity must be high enough to prevent particle aggregation, but low enough to allow substrate-catalyst interactions. To show this, Xue *et al.* utilized three similar capping ligands for Pd nanoparticle synthesis: 3-hydoxybutanoic acid, 3-aminobutanoic acid and 3-chlorobutanoic acid.[22] The carboxylic group of butanoic acid is the interaction site of the Pd nanoparticle and capping ligand. However, by varying the β-substituent of butanoic acid (a non-binding substituent) the affinity of the butanoic acid for Pd varies and therefore different activities were seen for the dehydrogenative oxidation of

cyclohexanone to phenol. Furthermore, different stabilities were seen corresponding to the variable interactions of the metal and ligand.

- The organic ligand in the nanoparticle composition has a further role when targeting supported metal nanoparticles. Synthesized nanoparticles are commonly supported on a metal oxide and used as a heterogeneous catalyst. Traditionally, this is for catalyst recovery and stability, yet other benefits can exist due to metal-surface interactions that will be discussed later. Nanoparticles dispersed in solution and used for catalysis can be difficult to recover. Commonly an inert, cheap metal oxide is used to support the particles, such as silica or alumina. While supported nanoparticle catalysts can be made directly via wetness impregnation routes by reducing metal salts on oxide supports, this route typically does not allow for control of nanoparticle sizes and compositions. An alternative technique in the synthesis of supported nanoparticles is to suspend previously synthesized nanoparticles in a minimum amount of volatile liquid and add this to dry metal oxide producing a slurry. The liquid is boiled off and due to the nanoparticle capping agent, the particle can adhere to the metal oxide nanoparticles. The system is usually calcined and, in this process ideally the organics are all removed. However, even after calcination typically organic species can still be present and sintering of nanoparticles at high temperatures can lead to a loss of nanoparticle size control.

The specific drawback to conventional modern nanoparticle synthesis method is the capping agent. Capping ligands are a required complication of conventional supported nanoparticle synthesis. The necessity of these ligands has been exploited as a benefit utilizing specific ligands

to synthesize specifically-shaped and -sized particles. However, the ligands bring complications to the synthesis of heterogeneous catalysts based on supported nanoparticles. A capped nanoparticle can be viewed as a core-shell particle: metal nanoparticle core with a ligand shell.[23] This ligand shell will interact with the catalyst, the substrate and the environment, each of which is possibly detrimental to catalytic activity:

- Ligand-Substrate Interaction: The substrate will interact with the ligand before being able to get to the catalyst. With careful consideration shells of ligand surrounding the catalyst can be utilized to promote selectivity by preventing the substrate catalyst interaction. Although it can be used positively, it can also be detrimental towards the interaction of the substrate with the catalyst.[24] Specific considerations must be taken into account varying from substrate-ligand reactivity to substrate-ligand polarity complicating the process.
- Ligand-Solvent Interaction: The polarity of the ligand has to be considered due to its interaction with the solvent. Ideally, the ligand will be entirely solvated, making channels that will allow the movement of substrate to and from the particle. However, changes in the chemical environment around the particles may cause the ligand to collapse around the nanoparticle, isolating the particle from interacting with the substrate.[23]
- Ligand-Catalyst Interaction: The capping ligand must bind somehow to the catalyst. These binding sites will cover at least a portion of the active sites on the catalyst surface. However, more considerable effects are possible including poisoning of the catalyst entirely. Also, strong chemical interactions between the two species may exist, as is seen in the case of thiolate groups with Pd. Although thiolates can be an effective capping ligand for Pd nanoparticles they are typically represented as forming PdS_x shells which are covered by the thiolate moieties.[25]

1.3.3 Galvanic Synthesis of Nanomaterials

Synthetic routes to synthesize nanoparticles without ligands are of interest. Exploitation of galvanic interactions seems a likely route towards this goal. To this point spontaneous galvanic interactions in nanomaterial synthesis, specifically Pd nanoparticles, have not been thoroughly utilized as seen in Chen *et al.*'s review of Pd nanoparticle synthesis in which galvanic synthesis was mentioned in only one context: galvanic replacement reaction (GRR) (also referred to as galvanic exchange reaction and displacement deposition).[26] Simply, GRRs take advantage of spontaneous redox reactions to exchange metals on the surface of metal nanoparticles to create bimetallic metal nanoparticles. For example, Qiu *et al.* utilized GRR to create Fe-Pd thin films by first synthesizing Fe thin films, and then exploited the galvanic potentials of Pd(II) (0.95 V) and Fe^0 (-0.44 V) (redox potentials reported against standard hydrogen electrode) to synthesize Pd-Fe bimetallic thin films.[27] Due to the synthetic technique of GRR unique particle morphologies are possible leading to synthesis of hollow or core-shell catalysts. For example, our group has shown that $Fe@Fe_xO_y/Pd$ nanoparticles can be made in which Pd galvanically reacts with external FeO surfaces, or with Fe cores inside hollow spheres of Fe_3O_4.[28-30]

Galvanic reactions involving pure metal oxide nanoparticles are rare.[31] A GRR of Mn_3O_4 with Fe(II) to form hollow Fe_2O_3 nanocages was well characterized by Oh *et al.* who presented the reaction as occurring in three steps as seen in Figure 1.1.[32] Deposition on the surface happens first, causing hole expansion due to the Kirkendall effect as interior atoms migrate to the surface.[33] Inside deposition occurs as fissures in the metal oxide particle allow deposition on the interior of

the system. Wall thickening occurs as time proceeds and the deposited atoms become the dominant species in the particle.

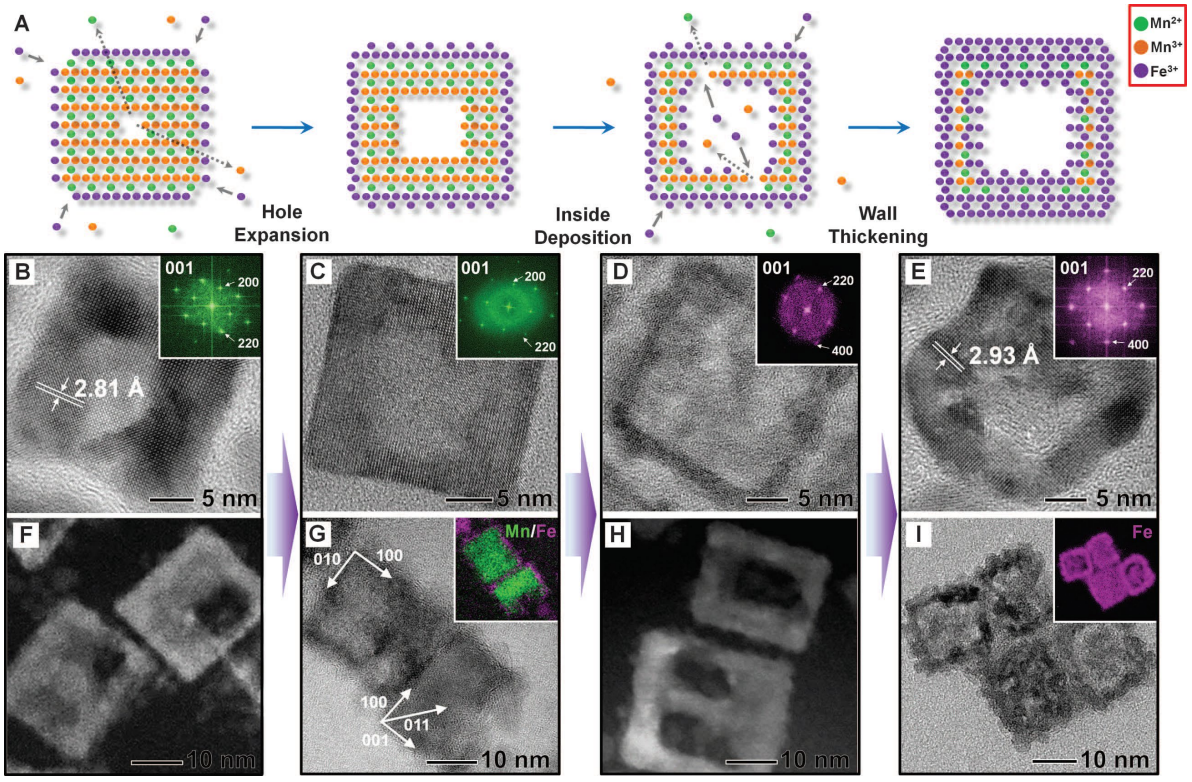

Figure 1.1. Galvanic Replacement Reaction as presented by Oh *et. al.* a) Illustration of the galvanic replacement reaction b to e) TEM images of Mn_3O_4 nano cubes with varying iron (II) perchlorate concentrations: b) 0.4 M c) 0.6 M d) 1.0 M e) 1.6 M. Insets depict associated diffraction patterns calculated via Fourier Transform. f and h) High-Angle Annular Dark Field Scanning TEM of above image. g and i) TEM image and (inset) energy filtered TEM image of above image. From Oh, M. H. *et. al.* Galvanic Replacement Reactions in Metal Oxide Nanocrystals, *Science* **2013,** *340* (6135), 964-968. Reprinted with permissions from AAAS.

Most galvanic exchange systems are metal on metal systems or metal on metal oxide nanoparticles, while typical industrial catalysts consist of metal nanoparticles on metal oxide supports. Using galvanic exchange, synthesis of metal on metal oxide systems typically utilized by industry seems plausible. The targeted galvanic system in this thesis is a metal oxide nanoparticle decorated by metal nanoparticles deposited via galvanic interactions. Galvanic

deposition will target the synthesis of metal nanomaterials on the surface of metal oxides. Rather than do complete galvanic exchanges, sub-stoichiometric amounts of a second metal will be added to the support to allow for it to be galvanically dispersed on the metal oxide support. To do this specific metal oxide supports must be used in order to exploit galvanic potentials. These supports, termed exotic supports, can be selectively chosen for specific properties that may be beneficial to particular reactions.

1.3.4 Exotic Supports

Conventional supports for heterogeneous catalysts are Al_2O_3 and SiO_2. These metal oxides are likely prevalent in the literature as they are inert, cheap, and work for a large number of systems. The inert characteristic of these metal oxides is favorable as, typically, the metal oxide is not intended to take part in the catalytic reaction. SiO_2 and Al_2O_3 are cheap materials to purchase and are available with a variety of surface areas and pore sizes. However, a variety of other metal oxides exist, with a variety of different properties. These "exotic" metal oxides vary including examples like La_2O_3, ZrO_2, and Fe_2O_3 and are selected for a variety of properties. The properties range from recoverability to the ability to participate as co-catalysts in reactions via phenomena including spillover or co-reaction sites.[28, 34, 35] In the case of methane oxidation, oxygen mobility in the lattice and redox behaviour of the support has been shown to have strong benefits.[35-39] Conventionally the primary source of the oxygen has been in the flue gas stream, however, with exotic oxide supports a new source for activated oxygen is available from the metal oxide.[35] Species such as ZrO_2, SnO_2, CeO_2 and Co_2O_3 which have nonstoichiometric states available are particularly suited for this contribution.

D. Ciuparu *et al.*, utilized temperature programmed isotopic exchange to monitor oxygen movement throughout an *in situ* catalytic system.[35] Comparing Pd on zirconia and alumina supports they found even in the absence of oxygen gas, methane oxidation is possible as the support provides oxygen to the Pd to oxidize methane. Comparably, Pd/ZrO_2 significantly outperformed Pd/Al_2O_3. Pd/ZrO_2 was able to remain at consistent methane oxidation for over 90 methane pulses, juxtaposed to Pd/Al_2O_3 systems which almost dramatically declined in activity, approaching 0 methane conversion after 35 cycles. Furthermore, likely due to this oxygen donating phenomena, Pd/ZrO_2 was shown to have significantly higher activity (80 % methane conversion vs Pd/Al_2O_3 at 50 % methane conversion) for methane oxidation reactions in the presence of air under the same conditions.

1.3.5 Strong Metal Support Interaction

Due to the metal nanoparticle size, their interaction with the metal oxide is consequential to the electronic properties of the whole particle. This can be visualized as surface-surface electronic interactions (such as a Schottky barrier), with the support surface being "infinite" and the nanoparticle surface comprising the whole of the particle. Two important interactions exist: electronic and chemical.[40] The presence of these interactions is related to a plethora of factors including the electronegativity of the metal comprising the nanoparticle, the metal oxide surface speciation and atomic mobility of atoms within the metal oxide.[40] For the purpose of this thesis two metal – metal oxide interactions will be discussed: Weak Metal Support Interactions (WMSI) and Strong Metal Support Interactions (SMSI). This is a functional simplification of work performed and reviewed by Fu *et al.*[40] and discussed by Pan *et al.*[41]. SMSI is defined as occurring

when the electronic properties are tuned or changed in the metal nanoparticle due to the interaction with the metal oxide; on the other hand WMSI occurs when the metal is attached to the metal oxide but its underlying electronic characteristics are not significantly effected.[41] The morphology of the materials can also be affected, due to the electrophobicity or electrophilicity of the metal and metal oxide interaction. Electrophilic interactions are seen in SMSI, while in WMSI electrophobic interactions are typical. Pan *et al.* define three mechanisms of SMSI:[41]

- Electronic Effects – Interaction between the two species creates unique, local charge redistribution. This has an effect on the equilibria present on the surface of the supported nanoparticle. Metal-Semiconductor contact theory is used to model such interactions and explains changes in the d-band population, Fermi level, work function, and changes in the density of states.[42]
- Geometric Effect – The mobility and morphology of a metal species on a metal oxide is due to the favourability of electronic interactions between the surfaces. This can be conceptualized as hydrophobic vs hydrophilic surfaces. Water on a hydrophilic surface would flatten and spread whereas on a hydrophobic surface would bead and agglomerate. Similar effects are seen with metal nanoparticles on metal oxides. This effect was shown by Gonzalez-DelaCruz *et al.* who deposited cubic Ni nanoparticles on CeO_2.[43] After heating in reducing gases the Ni homogenously distributed on the support, synthesizing thin sheets of Ni dispersed on the CeO_2. This was modelled via EXAFS, discussed below, showing the coordination going from an initial large nanoparticle with a first shell coordination number (CN) of 12 to a low CN of 6 indicating a change to a particle morphology with dramatically increased surface area. This "wetting" of the CeO_2 surface by Ni indicates SMSI.

- Bifunctional Effect – The metal nanoparticle and metal oxide support can both provide sites for catalysis. These sites can be shared or migrating intermediate species may move from one site to another. This effect includes many site possibilities from dual site pathways, such as spillover mechanisms, and single, shared sites termed boundary or perimeter sites. The water gas shift reaction ($CO + H_2O \rightleftharpoons CO_2 + H_2$) is a reaction that proceeds through a bifunctional site. Kalamaras *et al.* showed this using Pt/TiO_2 catalysts and isotopic labelling experiments, showing that the CO adsorbs to Pt, diffuses to the metal-support interface at which point, labile oxygen from the support reacts with the Pt-adsorbed CO, synthesizing CO_2.[44]

1.3.6 Pd Speciation and the Challenges of $Pd(OH)_2$

As discussed previously, the focus in this thesis is on Pd as the active catalyst for methane oxidation reactions. However, the situation is complicated by reaction conditions. Standard reaction conditions vary, however, for the purposes of this work standard conditions will refer to temperatures above 300 ºC and below 600 ºC in humid air with trace methane. Be aware that the situation is further complicated by method of preparation, gaseous environment, and support species used.

Around and within the standard reaction conditions three Pd species are expected to exist: Pd, PdO, and $Pd(OH)_2$.[9] In methane/air mixtures, the active catalyst for methane oxidation is typically PdO, however, Pd presence on a PdO surface has been shown to improve catalytic activity.[45] A Pd $\rightleftharpoons$ PdO equilibrium can exist in the catalytic region, but at temperatures above 200 ºC and below 600 ºC in air, PdO is the dominant thermodynamic species and thereby typically is the most prominent of the three species in this temperature region.[9, 46] Below 450 ºC, H_2O competes for

PdO active sites creating a surface passivating layer of $Pd(OH)_2$.[47] The presence of $Pd(OH)_2$ is sometimes referred to as hydrous-PdO in the literature; *i.e.* it can be thought of as a surface species rather than a unique phase that exists in bulk.[48, 49] The specific temperature of the $PdO \rightleftharpoons Pd(OH)_2$ equilibrium is manipulated by a variety of factors and is strongly dependent on the catalytic system and will be the subject of Chapter 3.

A likely pathway of the *in situ* production of $Pd(OH)_2$ is expressed in Equation 1.1 and Equation 1.2. Water competes for active sites, creating $Pd(OH)_2$, and thus creating the limiting factor for the ignition temperature of the catalyst. Due to the production of water during the catalytic combustion of methane, $Pd(OH)_2$ passivation is not an issue that can be solved solely by removing water from the feed.[50] The effect of $Pd(OH)_2$ formation has been explored and is known in the field as water inhibition.[51] Burch *et al.* concluded that the dehydroxylation of Pd hydroxide was likely the rate determining step in the methane oxidation reaction.[52] However, they were not able to directly characterize the $Pd(OH)_2$ species.

$$2\,Pd_{(s)} + O_{2(g)} \leftrightarrows 2\,PdO_{(s)} \qquad (1.1)$$

$$PdO_{(s)} + H_2O_{(g)} \leftrightarrows Pd(OH)_{2(s)} \qquad (1.2)$$

In situ characterization of the hydroxide species has remained elusive. Albers *et al.* studied Pearlman's Catalyst, typically defined as $Pd(OH)_2$/carbon and thoroughly speciated the sample.[49] Via a range of specific measurement techniques aimed at identifying and characterizing the hydroxide, they concluded that the catalyst is more accurately described as $C/PdO/OH/H_2O$; that is carbon supported hydroxylated PdO with surface hydration.[49] Although the exact species is controversial the effect and synthesis of hydrous PdO, $Pd(OH)_2$, and $C/PdO/OH/H_2O$ are

presumably the same species. Herein this species will be referred to as $Pd(OH)_2$, however, work is done while being aware of the complexities described above.

1.3.6.1 Possible Solutions to $Pd(OH)_2$

The immediate reaction to the problem of water inhibition may be to dry the flue gas feed in a system. However, since methane oxidation produces water on the catalyst surface, this solution is moot. A chemical solution to the problem must be made. Three solutions in particular have had successes:

- PdPt Bimetallic Species: Bimetallic species are Pd nanoparticles which have low concentrations of a co-metal incorporated in them. Specifically PdPt catalysts have been researched by our group[53, 54] and others.[55] These species incorporate small amounts of co-metals into the nanoparticle in order to manipulate electronic properties in much the same way as SMSI manipulates the electronic properties of the metal.[56] Our group findings have shown that the presence of Pt dramatically lowers the amount of Pd that is oxidized, and thereby hydrated, during methane oxidation.[53, 54]
- Exotic Supports: Manipulations of the metal from the support has been shown to change the electronic and therefore catalytic properties, as discussed in 1.3.4 above, and referred to as Strong Metal Support Interactions. Utilization of specific strong metal/metal oxide interactions can assist with the resilience of the catalysts to humidity.[57]
- Cocatalyst: Addition of a third species to assist in a specific role has also been shown. Pd(0) to PdO oxidation can be a limiting factor for methane oxidation after water passivation, therefore, once water passivation is solved by bimetallic catalysts and/or SMSI, readily

oxidizing Pd(0) species becomes a priority. For example, Osman *et al.* utilized $PdPt/TiO_2/ZSM\text{-}5$ to show 100% methane conversion by 300 ºC, a very low temperature for total methane oxidation.[58] This system utilized H-ZSM-5(80), a high surface area, acidic zeolite, to help continually reoxidize Pd(0).

This thesis will be focusing on the utilization of exotic supports in order to manipulate electronic characteristics of Pd and thereby dehydrate the PdO species at low temperatures in order to reduce ignition temperatures for methane oxidation.

1.4 Characterization

The following section will be composed of specific analytical techniques utilized in this research that the reader may not have a working understanding of. The research is specifically focused on heavy metal nuclei therefore X-ray techniques are exploited. X-ray photoelectron spectroscopy (XPS) is used to thoroughly analyze surface layers. X-ray absorption spectroscopy (XAS) is utilized for bulk analysis with high sensitivity. The intent in the following subchapters is to describe the ability of the techniques such that the reader can gain a working understanding of these techniques to support an understanding of the thesis thereafter. The discussion will be focused on the catalyst system described above, Pd on metal oxide supports.

1.4.1 X-Ray Photoelectron Spectroscopy

XPS techniques are performed by photons emitted by a monochromatic light source (typically Al K-alpha 1486.6 eV) at a sample stored under ultra high vacuum (UHV). The photon collides with the sample, releasing a photoelectron, as per the photoelectron effect. The kinetic energy of the released photon can be detected and, using the relationship expressed in Equation 1.3, the

binding energy can be calculated, allowing for an understanding of the speciation of the atom that released the electron.[59]

$$E_{\text{Incident Photon}} = KE_{\text{Photoelectron}} + BE + \phi \qquad (1.3)$$

Since the energy of the incident photon is known, and the kinetic energy of the photoelectron is measured, the binding energy and work function (ϕ) are the two remaining variables, both descriptive of the species. The work function is commonly compensated for artificially, simplifying the relationship to Equation 1.4.[60]

$$E_{\text{Incident Photon}} = KE_{\text{Photoelectron}} + BE \qquad (1.4)$$

Equation 1.4 shows the relationship used in XPS. Recognize that in this relationship either Kinetic Energy or Binding Energy could be reported and used for speciation. Although both are accurate, reporting Kinetic Energy comes with an inherent complication: different incident photon energies (differing due to the use of different light sources) would produce different kinetic energies of the photoelectron in the same sample. Therefore, it is most common to report the Binding Energy, which is not dependent on the incident photon energy. However, KE is measured, due to this, XPS data is commonly shown with binding energy decreasing left to right on the x axis.

Incident X-ray photons penetrate over 1000 Å into the surface, however, XPS is still understood as a surface sensitive technique.[61] This is due to the fact that a released photoelectron has to make its way to the detector. Surface photoelectrons can do this uninhibited, but photoelectrons emitted from deeper in the material will interact with the material. The distance a photoelectron can move within the material is proportional to, λ, the inelastic mean free path. The

inelastic mean free path is defined as the average distance that a photoelectron travels through the material between inelastic collisions.[61]

Inversely, this can be thought of as the escape depth: the thickness from which half the photoelectron intensity is derived.[62] The mean free path is generalized to be about 20 Å in most materials, however, it does vary dramatically between materials. This phenomenon is depicted in Figure 1.2.

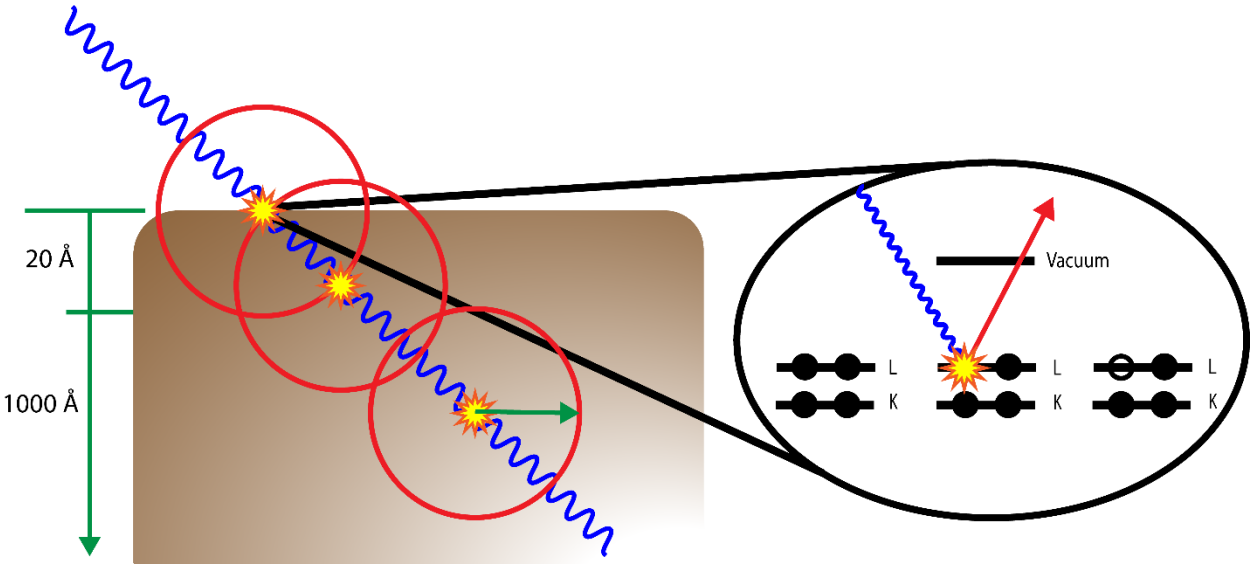

Figure 1.2. X-Ray Photoelectron Spectroscopy schematic showing incident photon penetration depth (blue), photoelectron emission (yellow stars) and photoelectron maximum possible path travelled (red circle).

XPS is a valuable technique for characterizing surfaces but has two primary challenges for this research. Firstly, due to the fact that XPS is typically surface sensitive, a complete picture of the system can not be depicted by XPS alone. Secondly, as mentioned previously, XPS is typically performed in UHV. Although *"in situ"* setups are accessible for XPS (for example, via moving the sample to a second environmentally controlled chamber), the actual measurement has to be

performed under UHV and typically without temperature regulation. This means the *in situ* measurements targeted by this research cannot easily be performed using XPS because exposing the catalyst surface to UHV could likely change the surface species. However, with these considerations in mind XPS is still used as a surface characterization technique throughout this work and used to complement XAS work.

1.4.2 Synchrotron X-Ray Absorption Spectroscopy

Synchrotron radiation is electromagnetic radiation produced by accelerating and changing the path of charged particles at relativistic speeds using electromagnetic fields.[63] Synchrotron radiation is an asset as it provides a wide spectral array of intense, in phase light.[63] Two primary synchrotron radiation characteristics are particularly relevant to this research: brilliance and coherence. Brilliance is defined as the amount of photons emitted per second, which is relevant to the experimenter as a high flux of incident photons.[64] Such high brilliance allows filtering of incoming light to target very specific wavelengths still with high fluxes, thus reducing noise or signal overlap from other elements. Coherence is the phase relationship of the light; perfectly coherent light has all waves synchronized. To the experimenter coherence will be seen as a vast reduction in background noise.[65]

Typically, transmission detectors are used in which incident and transmitted photon intensity are used to compute the absorbance of the sample. Although common this experimental technique has major drawbacks for the experimenter. The sample loading must be in a specific concentration window to ensure enough X-rays are absorbed by the sample, while ensuring that a significant number of X-rays are still being transmitted through the sample for reliable data collection. This window is narrow and can be complicated by a variety of factors such as scattering. Fluorescence

detection instead measures fluoresced photons from the sample. As these are very high energy photons, not photoelectrons as discussed in XPS, the particle size is insignificant compared to the penetration depth. This aids in experimental design as the analyte fluoresced photons can be specifically targeted. Fluorescence detectors can also be manipulated to increase or decrease the signal merely by moving them closer to or further from the sample. This luxury allows the experimenter to quickly alter the setup to accommodate the sample, rather than altering the sample to accommodate the setup, as necessitated by transmission XAS measurements.

The complication associated to fluorescence detectors is the self absorption effect. IUPAC defines this as: The reabsorption of luminescence by the analyte and interfering impurities within the excitation volume.[66] However, with high energy radiation this definition does not work as the absorption and fluorescence energies tend to be dramatically different. In this thesis the term self-absorption will be referring only to high energy systems, therefore an operational definition must be instated: Self-absorption is the attenuation of the white line intensity at the absorption edge due to the reduction in interaction volume that occurs when the radiation energy passes the absorption edge.[67] This has been more precisely termed attenuation factor,[68] however, colloquially is still referred to as self absorption. With large sample sizes (thick films or pellets) or high concentrations the self absorption effect is increased.[69-71] To mitigate self absorption effects sample sizes and loadings are reduced as much as possible.

1.4.2.1 XANES

XANES, X-ray Absorption Near-Edge Structure Spectroscopy, is highly sensitive to oxidation state and coordination chemistry.[72] XANES spectroscopy measures electron transitions confined to a specific atom. Figure 1.3 presents a Co(III) K edge X-Ray Absorption Spectroscopy (XAS)

spectra. The spectrum is defined into three regions: pre-edge, XANES and the Extended X-ray Absorption Fine Structure (EXAFS). The pre-edge region is before the edge, the vertical region, and is used to normalize and define intensity zero for the data set. It is the horizontal line on the far left absorption edge. The XANES region is the subsequent region. It includes the edge (the inflection point, E_0), the white line (first allowable transition) and *ca.* 30 eV after the edge, defined differently depending on the element and edge. On the edge is E_0, indicated with an arrow. E_0 is typically the last inflection point on the edge and is used to define the energy of the edge. E_0 is dependent on the element, its oxidation state and its coordination environment. Also, E_0 is used when referencing positions on the XAS spectrum, in which case E_0 is defined as 0 eV. In this nomenclature the XANES region would be defined as approximately -20 eV to 30 eV. XANES also includes specific features that are due to atomic transitions. These include pre-edge features, indicated by the arrow in the inset, which are forbidden transitions and therefore are significantly lower in intensity, as they are dramatically less likely to occur. XANES features such as the white line occur at the maxima in the graph, which is the first allowed transition. Multiple XANES features can be present in different species, and thus each XANES spectra can be thought of as a fingerprint of a particular chemical species. Following the XANES region is the EXAFS region. In this region photoelectrons have been ionized from the absorbing atom, and the scattering of those photoelectrons from neighbouring atoms attenuates the absorption spectrum.

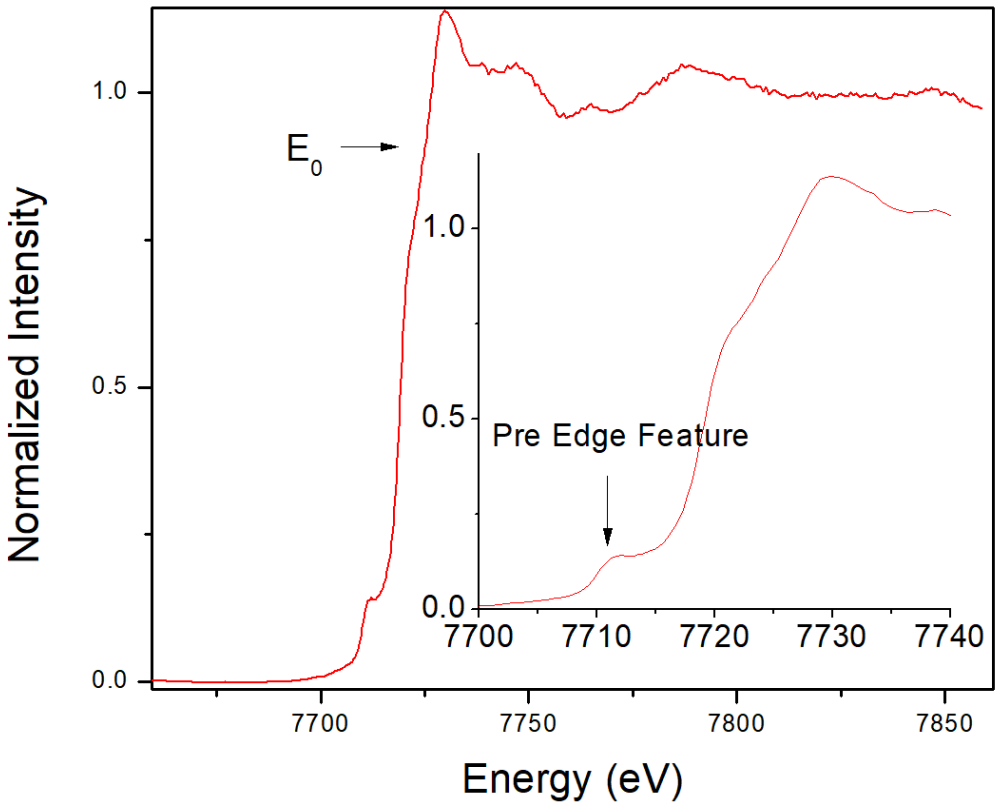

Figure 1.3. Co(III) K edge X-Ray absorption spectrum. The inset shows a magnified view of the pre edge and XANES regions.

XANES was utilized as a tool to measure Pd/SnO_2 materials by Wagner *et al.* using Pd L_3-edge white line features.[73] The white line of the L_3 edge, or the $2p_{3/2}$ to 4d transition, of Pd increases in intensity as the electron density of the Pd decreases.[74] Wagner *et al.* utilized this phenomenon to determine the relative amount of Pd (II) vs Pd (0) in Pd/SnO_2 in order to understand the speciation of Pd/SnO_2 for methane gas detection.[73] Although a qualitative correlation between Pd oxidation state and sensor response was attained, the *ex situ* experimental design was not able to determine a quantitative correlation between sensor response and Pd oxidation state. This was due to the attempt of "freezing" the current oxidation state of the sample, a process discussed below as

catalyst fossilization. Furthermore, complications with nanomaterial vs. bulk properties of Pd further complicated attempts to quantify their measurements. Although interesting results were attained, the authors concluded that *in situ* X-ray Absorption Spectroscopy techniques would be required for a systematic correlation of oxidation state vs. sensor response. However, with their available equipment, this was not accessible at the time.

1.4.2.2 *In situ* X-Ray Absorption Spectroscopy

With modern characterization techniques a very thorough understanding of a system can be attained. However, understanding a system under measurement conditions may be misleading as the system may be altered in different environments. Conventional spectroscopy characterization, or *ex situ* characterization, measures samples at specific stages in the creation and use of the material. For example, for a methane oxidation catalyst an experimenter may measure the catalyst before activation, after activation, and after catalysis. This measures the catalyst before and after a reaction, not during, creating an understanding of the catalyst that is arguably irrelevant to the actual function of the catalyst. A process known as catalyst fossilization attempts to close this gap by removing a catalyst during catalysis and isolating it in inert atmospheres and/or low temperatures, then measuring the material.[19] Although better, this method still negates the adverse conditions of the typical catalytic environment by removing the catalyst from the environment. Changes are anticipated to occur in the catalyst once it has been removed from its catalytic environment. Methane oxidation catalysts are intended to operate at temperatures ranging from ambient to 600 ^{o}C under humid methane/air gas flows. These environments have pervasive impacts on the species of the catalyst which mitigates the understanding attainable by the

application of common *ex situ* techniques. Understanding of these systems in these environments necessitates immersing the sample in the expected environment during a measurement, referred to as an *in situ* measurement. *In situ* techniques are becoming more common in all fields as these techniques become more accessible allowing scientists to learn much more specific information about materials under the conditions in which they are typically used.

XAS at synchrotrons is an excellent technique for *in situ* experiments, because of the benefits of synchrotron light, as discussed previously. High energy XAS measurements do not require vacuum or other specific environment conditions, allowing a variety of environments to be applied to a material without disturbing the measurement. When exploited these conditions are especially well suited for *in situ* techniques and, therefore, a variety of techniques have been applied. Measurement of heterogenous catalysts in soft X-ray environments is complicated by the immersion in gases that may scatter or absorb incident and fluoresced photons. This is a specific adversity for soft X-rays, defined generally as X-rays with energies below 4000 eV, which are scattered by common gases enough to significantly impact measurements.[75] In this case the analyte is commonly immersed in He in the cell during the measurement. This is similar to the concept of catalyst fossilization, albeit, the delay time between immersion in specific environment and the measurement under He is on the order of minutes, not hours or days. Furthermore, the temperature is not changed, as it is with catalyst fossilization work.

A variety of *in situ* XAS techniques exist with differing complications and benefits. Grunwaldt *et al.* utilized XAS to measure the oxidation state of Pd and Zr in both a Pd-Zr alloy and Pd/ZrO_2 catalyst in methane combustion environments, focusing on the K-edge of each species.[76] With the technique they were able to determine that both species were oxidized simultaneously, and they

determined that Pd is primarily PdO in methane combustion environments. No quantification of species was presented in their study.

Dr. Scott's group has worked on the characterization of methane oxidation catalysts via *in situ* XAS utilizing XANES and EXAFS of the K edge of Pd.[53, 54] The group was able to collect satisfactory EXAFS data up to 300 ºC at which point thermal disorder prevented modeling of the EXAFS data, a required step for the understanding of EXAFS information. However, the XANES region was reliable up to and beyond 600 ºC, as it is significantly less sensitive to thermal disorder. Previous group work struggled in distinguishing between PdO and $Pd(OH)_2$ and instead focused on changes in the oxidation state, Pd(0) vs Pd(II).[54] Linear combination analyses of XANES data allowed for quantification of the relative species present in the system.

1.4.2.2.1 Linear Combination Fitting

Collected XAS data is an amalgamation of multiple data sets from different atoms. These atoms are the same element but can be of the same or different species, producing the same or different spectra. Linear Combination Fitting (LCF) is a way to deconvolute these spectra. Certain constraints can be used to assist the fitting in a variety of ways. This discussion will only discuss how the fitting was performed within this work; a variety of different methods exist. LCF is a technique based on using a linear combination of reference datasets which are adjusted to reduce the R-factor of the fit. Linear combination is the summation of multiple vectors, v_n, multiplied by scalars, c_n, in order to produce a new vector, "fit," as can be seen in Equation 1.5.

$$c_1 v_1 + \cdots + c_n v_n = \text{fit} \qquad (1.5)$$

In the case of the LCF the vector, v, is a sample standard spectrum given a scalar, c, between 0 and 1. Colloquially the word "weighting" is used in position of scalar, as the scalar is the weighting that the vector contributes to the fit. This produces a vector "fit" which is compared to the data vector, "data." The difference between the fit and the experimental data is evaluated by the R-factor, presented in Equation 1.6. LCF works to reduce R-factor by varying the scalars.

$$\frac{\sum((\text{data}-\text{fit})^2)}{\sum(\text{data}^2)} = \text{R} - \text{factor} \qquad (1.6)$$

It should be noted that the scalars do not have to be forced to equal 1 (though this is a possible constraint in some programs). Upon completion the weighting is manually summed and expected to equal 1. If it does not this is a sign of either missing standards or poor quality data being used for the LCF.[67] Not adding the constraint that the scalars have to add up to one increases the confidence in the data set as a sum to ~1 suggests that all required atomic species have been accounted for and spectra are well calibrated. If the sample does not sum to ~1 this suggests problems in the fitting, including not fitting the appropriate number of species. In this work values of ~1 with low R-Factors was deemed enough assurance that all species were being fit. In the cases where the sum was not ~1 reviews of literature were taken to determine an appropriate library of standards to ensure accurate fitting.

Secondly, note the energy of the edge, E_0, should not be a variable in the fitting. E_0 defines the inflection point of the edge, which is specific to different species. Therefore, allowing variation in E_0 allows the movement of spectra in energy space to force an overlay, possibly creating artificially improved fits.[67] Instead, data should be properly calibrated before doing the LCF as the position of E_0 is not arbitrary.

Summarily, specific care and prudence in choosing appropriate libraries of standards is required to attain useful results. LCF is a powerful tool that must be utilized with caution to ensure conclusions reached from LCF are meaningful.

1.4.3 Temperature Programmed Reduction

Temperature programmed reduction (TPR) is an experimental technique that follows the reduction of materials, as a function of temperature. It belongs to a group of temperature programmed techniques including reduction, desorption, and oxidation which were utilized first in the late 1960s and became more widespread in the 1980s.[77] Summarily, the class of techniques consists of a heating element containing the sample, through which a gas can be passed and the exhaust gas can be analyzed for concentration of a variety of species.[77] Further discussion will focus on the TPR technique. A typical setup flows reducing gas mixtures, typically forming gas (5 % H_2 in He), through a tube furnace containing the material of interest. The exhaust gases are then measured for concentration of hydrogen and/or water typically by a thermal conductivity detector or by mass spectrometry (MS). Decrease of the H_2 concentration and increases in the water content in the effluent gas is correlated to the amount of reduction of the material and the temperature at which it occurs. MS detectors are more efficient at this task than thermal conductivity detectors as it is beneficial that the detector distinguishes between water and hydrogen, a simple task for MS. Information gleaned from TPR can be used in a variety of ways. For this thesis TPR-MS will be used to follow the reduction of metal oxides and metals to particular oxidation states for synthetic purposes.

1.4.3.1 Chemisorption

Chemisorption is an analytical technique that exploits the interaction between a gas and an analyte in order to calculate the surface area of the analyte. This thesis will focus on utilizing chemisorption to analyze metals supported on metal oxides, and therefore this discussion will focus on this aspect. Secondly the specific chemisorption technique utilized is pulse chemisorption, therefore this technique will be the focus of the discussion.

A sample containing a metallic species is inserted into a tube with controlled gas feed and a detector for effluent gases, in our case a thermal conductivity detector. The system is initially calibrated, without analyte, to have a known signal for each pulse of CO gas. 0.1 to 1.0 g of the analyte is added to a thin quartz or steel tube. The system is then degassed at increased temperature and filled with an inert gas such as Ar. Then CO gas is pulsed into the system at which point it preferentially binds to a metal (not a metal oxide support) and thereby less CO gas reaches the detector. The difference between the peak of the CO calibration standard and the CO when the metal is in the flow is the amount of CO adsorbed to the metal.

Chemisorption experiments are used to calculate dispersion and particle size. Dispersion is calculated using Equation 1.7 where n_S is the number of surface atoms and n_T is total atoms of the metal.[78] n_s is calculated by the stoichiometric relationship between the adsorbed gas and the metal, for Pd and CO this is a 1:1 relationship.[79] n_T is calculated separately from the chemisorption experiment in a variety of ways, such as elemental analysis.

$$\text{Dispersion} = \text{D} = \frac{n_S}{n_T} \qquad (1.7)$$

From dispersion data, the particle size can be estimated. Calculations for supported particle size from dispersity are based on Equation 1.8 (a variety of equations are available), where d is particle size, ρ_s is surface site density, W_m is molecular weight, N_A is Avogadro's Number, ρ_m is atomic density and D is dispersion. This calculation of particle size comes with a variety of assumptions including morphology, and availability of all surface sites for CO absorption. Larger errors are seen measuring smaller particles, as a sphere becomes less accurate at describing the particle morphology at small sizes.[80]

$$d = \frac{(5\times10^{10})\,\rho_s\,W_m}{N_A\,\rho_m\,D} \qquad (1.8)$$

1.5 Objectives

This thesis intends to contribute towards the work of methane oxidation catalysis in two ways. First, a novel synthetic route to synthesize supported metal/metal oxide catalysts, galvanic deposition, is introduced, characterized and discussed. The intent of the method is to simplify and improve on current synthetic techniques for making highly disperse metal clusters and/or nanoparticles on metal oxide supports. In the second half of the thesis, an analysis of Pd speciation in methane oxidation environments is performed for Pd nanoparticles on a variety of different metal oxide supports. A method is presented to follow and quantify the species of Pd *in situ* and show that we can distinguish $Pd(OH)_2$ from PdO using *in situ* XANES techniques.

Chapter 2 will discuss galvanic deposition (GD) as an alternative strategy to synthesize methane oxidation catalysts. GD is a method that can allow one to decorate metal nanoparticles on metal oxide particles. It has a variety of benefits including synthetic simplicity and lack of organic

molecules in the synthesis. As discussed previously, modern metal/metal oxide synthetic techniques that give controlled nanoparticle sizes and compositions often necessitate prefabricating the nanoparticles with a ligand shell, which is used to prevent aggregation and to adhere the nanoparticle on the metal oxide. GD, on the other hand, can occur without the use of organic ligands. Optimization of the technique to allow for control of nanoparticle size would allow a simple route for active supported nanoparticle catalysts to be synthesized. This is predicted to synthesize competitively small nanoparticles, with high dispersion, such that galvanic deposition can be another tool in the supported metal nanoparticle synthesis repertoire.

Chapter 3 will aim to further understand the chemistry of methane oxidation catalysts by *in situ* XANES. This technique can allow quantitative understanding of methane oxidation catalyst speciation *in situ*, both for the metal oxide, and metal. The quantification of the speciation of Pd species, including $Pd(OH)_2$, will allow scientists to better understand a fundamental issue of methane oxidation: water poisoning. *In situ* XAS coupled with linear combination fitting is able to follow Pd speciation during methane oxidation reactions. The influence of the metal oxide support on the *in situ* Pd-PdO-$Pd(OH)_2$ speciation is poorly understood in literature and is enlightened by the use of this technique. The XAS measurements are corroborated by a variety of more conventional characterization techniques. The investigation into the speciation of supported Pd nanoparticles *in situ* on a variety of supports is expected to show significant differences in Pd speciation as a function of temperature due to the metal oxide support the Pd is on. Following this investigation is made to attempt to answer why the Pd speciation is so affected by these different supports.

Finally, Chapter 4 will summarize the experimental work and conclusions drawn from the experimental work. Chapter 4 will also show how the contributions of this thesis are important to the methane oxidation catalysis field and present ideas for future studies.

Chapter 2 Galvanic Deposition[1]

2.1 Introduction

Conventional, modern nanoparticle synthesis techniques are becoming well understood, however, a variety of difficulties are inherent to the procedure.[13-15] Two general approaches to supported metal nanoparticle catalysts on metal oxides are common: wetness impregnation and colloidal synthesis and activation.[81] Impregnation methods are pervasive and among the most widespread methods in literature. Simply, a metal precursor is dissolved in a minimal amount of liquid, added to the metal oxide and the metal oxide is then dried. This yields a metal salt on a metal oxide and due to capillary action, the liquid, and thereby the salt, is generally concentrated in pores of the metal oxide. Thermal treatment is then required to reduce the metal salt to a zerovalent metal, yielding metal nanoparticles on the metal oxide support. Due to the randomness of the interactions between the metal salt and metal oxide, highly polydisperse nanoparticles are generally synthesized.[81] Colloidal metal-metal oxide supported nanoparticle synthesis requires the synthesis of colloidal nanoparticles followed by the adhesion of the particles to a support, and commonly the subsequent calcination of the system, a step utilized to remove organics and increase interaction between the metal and metal oxide. Colloidal synthesis produces the most monodisperse nanoparticles,[81] however, detrimentally, at least two organic species are used in this process, a reducing agent, and a protecting/binding ligand. The protecting ligand can be removed in the calcination process, causing side products, incomplete combustion, and particle sintering to

[1] Pd/FeO work shown in this chapter was performed by Jonathon Trach, a summer student of Dr. Andrew Grosvenor and Dr. Robert Scott, who was working under my supervision in the summer of 2018. TPR and chemisorption work was performed by Dr. Jing Shen a post doctoral fellow for Dr. Natalia Semagina, in the University of Alberta Chemical Engineering Department.

occur all of which can have deleterious effects that can retard catalytic activity.[23] Ligands remaining on the nanoparticle surface can cause mass transfer problems as they block catalytic sites, but other problems can also persist such as catalytic side reactions and poor adherence of the nanoparticles to the support.[24, 25] Ligand-substrate, ligand-solvent and ligand-catalyst interactions have all been shown to have negative effects on catalysis, and are more thoroughly discussed in Chapter 1.[23-25] Nanoparticle sintering, via Ostwald Ripening or particle migration and coalescence also occurs during the calcination step. This leads to the formation of larger nanoparticles with less surface area, which are typically less catalytically efficient.[82] Alternative routes to make supported-nanoparticle catalysts that allow for high dispersity and uniform deposition of catalytic nanoparticles on supports are needed. Spontaneous galvanic reactions, in which metal salts directly react and reduce onto a solid metal-oxide support, allow a reaction pathway that does not require these organic stabilizing species which can interfere with the catalytic system.

Galvanic reactions have been used in nanochemistry, however, have not been thoroughly explored in the metal on metal oxide support context.[32] In order for the galvanic deposition reaction to occur only two reagents are required: the metal salt and the metal oxide. The metal salts role does not change: the source of active catalyst. However, the metal oxide takes on additional roles, acting both as a reducing agent and stabilizer. The targeted particle will consist of a metal oxide support decorated by the active catalyst. The synthetic procedure looks to take advantage of Strong Metal Support Interaction (SMSI) phenomena. Chapter 1 discusses this more in depth, briefly: SMSI effects increase interactions between the two surfaces, and alter the electronic properties of the catalyst.[41]

Herein a case study will be presented with a targeted product of Pd nanoparticles dispersed on SnO_2 supports. Pd/SnO_2 is utilized in gas sensing,[83] electrochemical reduction of CO_2 to

methanol,[84] and Pd/SnO_2 is also known to be an interesting humidity-tolerant catalyst for low temperature methane oxidation.[85] This catalytic reaction is the target catalytic reaction for this thesis and is discussed thoroughly both in Chapters 1 and 3. Galvanic routes exist for the synthesis of Pd/SnO_2, by first synthesizing SnO which has a spontaneous galvanic reaction with Pd(II) salts. When mixed this leads to the reduction of Pd(II) salts and the oxidation of the SnO surface. The presented synthetic technique utilizes no organic ligands, occurs in a one pot synthesis in less than an hour, has a direct metal, metal oxide interaction and a comparable dispersion to colloidal synthesized Pd/SnO_2. To show the generality of the protocol, the galvanic deposition process was also applied to the Pd/FeO system.

2.2 Experimental

2.2.1 Materials

Tin(II) oxide (≤ 60 micron particle size, powder, (97 %)), $[Fe(acac)_3]$ (99.9%), potassium palladium (II) tetrachloride (99.99 %), oleylamine (technical grade, 70%) and Pearlman's Catalyst ($Pd(OH)_2$/Carbon, 20 wt. % loading) were purchased from Sigma Aldrich. Oleic acid (99 %) was purchased from Alfa Aesar. Eighteen MΩ•cm Milli-Q water (Millipore, Bedford, MA) was used for synthesis. All gases were purchased from Praxair.

2.2.2 Methods

2.2.2.1 Reduction of SnO

Approximately 1 g of as received SnO was calcined in a Lindberg/Blue M tube furnace at 250 ºC for 12 h with a 1 h ramp up and 1 h ramp down time, while the system was purged with, and under constant flow of, forming gas (5 % H_2 in N_2). The SnO was then removed and kept under an argon blanket for storage.

2.2.2.2 Galvanic Deposition and Oxidation of Pd/SnO to PdO/SnO_2

The relative amounts of K_2PdCl_4 and SnO were varied to give different Pd loadings, however, a typical experiment is as follows: 0.0027 g of K_2PdCl_4 was dissolved in 25 mL of Milli-Q water with stirring. After the Pd(II) salt dissolved, 0.2200 g of SnO powder was added to the solution while stirring at approximately 900 rpm and left stirring for 1 h. At this point stirring was stopped and the Pd/SnO powder was allowed to settle. The water was removed by pipette and the Pd/SnO was dried under high vacuum in a Schlenk line setup. The system was washed three times with approximately 10 mL of water and dried again with the Schlenk setup. The Pd/SnO sample was inserted into an open tube, tube-furnace (Lindberg Blue) for 16 h at 650 ºC in air, in order to synthesize PdO/SnO_2. Upon removal the targeted 0.4 w/w% catalyst is a light tan color, while higher Pd loadings had a darker tan-brown colour.

2.2.2.3 FeO synthesis

$Fe(acac)_3$ (1.4 g, 4.0 mmol), oleic acid (8 mL, 25 mmol), and oleylamine (12 mL, 35 mmol) were mixed and stirred in a three-necked flask. The mixture was degassed via a high vacuum pump

(Schlenk apparatus) followed by Ar bubbling over 3 cycles, removing oxygen and water. Under an Ar blanket, the mixture was heated at 120 ºC with vigorous stirring for 2 h, the solution was then heated to 220 ºC, using a heating mantle. The solution remained at this temperature for 30 mins before it was heated, at a heating rate of 2 ºC/min, to 300 ºC and kept at 300 ºC for 30 min. The heating mantle was removed, and the solution was allowed to cool to room temperature under ambient conditions. The FeO nanoparticles were separated from the solution by the addition of ethanol (20 mL) followed by centrifugation to collect the solid material. The nanoparticles were redispersed in hexane and precipitated out by ethanol. The product was stored under nitrogen in hexane.[86]

2.2.2.4 Chemisorption

Pd/SnO samples were reduced at 100 ºC in 10 % H_2/Ar for 1 h. Samples were then cooled under helium (20 mL/min) to room temperature (30 min cooling process). A 3 % CO/He (25 mL/min) and He carrier gas (50 mL/min) gas mixture at room temperature was purged through the system for dynamic CO pulse chemisorption analysis. Thermal conductivity detector (TCD) quantifies the amount of CO gas adsorbed by the sample. Assuming, negligible metal oxide adsorption of CO and assuming 1:1 CO:Pd stoichiometry, the surface amount of surface Pd can then be calculated from the amount of CO gas detected. Following chemisorption of Pd/SnO the system was heated to 650 ºC overnight under static air to give PdO/SnO_2. The sample was reduced again at 100 ºC in 10 % H_2/Ar for 1 hr, synthesizing Pd/SnO_2, cooled to room temperature under He and the dynamic CO chemisorption experiment was repeated.

2.2.2.5 Thermogravimetric Analysis

TGA experiments were performed using a TA instruments TGA Q5000IR with a heating rate of 10 ^{o}C/min under air flow.

2.2.2.6 UV-Vis Spectroscopy

A Cary 50 spectrometer was used for UV-Vis spectroscopy measurements. Measurements were taken with a step size of 1.0 nm from 200 to 1100 nm at a scan rate of 600 nm/min. Baseline correction was used using the same solvent as the analyte and the same 1.0 cm pathlength quartz cuvette used for the measurements. Compared spectra were normalized to set the absorbance at 600 nm to zero, which removed baseline height differences, caused by different scattering between samples.

2.2.2.7 X-Ray Diffraction

XRD was performed using a Rigaku Ultima IV X-Ray Diffractometer at University of Saskatchewan, Saskatchewan Structural Sciences Centre. A Cu 1.54056 Å light source was used. Continuous scanning from 20 to 80 degrees 2θ with a 0.02 degree 2θ step size was utilized. XRD data is analyzed by Powder Cell for Windows, PCW.[87]

2.2.2.8 X-Ray Photoelectron Spectroscopy

XPS was performed using a Kratos AXIS Supra system at the University of Saskatchewan, Saskatchewan Structural Sciences Centre. A 500 mm Rowland circle monochromated Al K-α

(1486.6 eV) source was utilized in tandem with a hemi-spherical analyzer and spherical mirror analyzer. A 300 x 700 micron spot size was used. High resolution scans (presented) utilized 0.05 eV step sizes with a pass energy of 20 eV. The accelerating voltage was 15 keV with an emission current of 15 mA. XPS calibration was performed using adventitious carbon 1s peaks which were calibrated at 284.8 eV. XPS data was analyzed using CasaXPS software.

2.2.2.9 Transmission Electron Microscopy

TEM was performed using a Hitachi HT7700, with energy dispersive spectroscopy and high resolution capabilities. Samples were prepared via drop casting particles suspended in hexane on to carbon-coated 200 mesh copper grids (purchased from Electron Microscopy Sciences, Hatfield, PA).

2.3 Results and Discussion

As can be seen in Equation 2.1 the galvanic deposition reaction is simple and requires no organic compounds such as ligands (for adhering or passivating nanoparticle growth) or reducing agents (for reducing metal salts to nanoparticles). This dramatically simplifies the reaction process and reduces the species remaining in solution. The reaction proceeds in three phases: reduction of the SnO surface, synthesis of Pd/SnO_x and oxidation of Pd/SnO_x which will be discussed chronologically.

$$SnO \xrightarrow{250\,℃,\ 16\,hrs} SnO + K_2PdCl_4 \xrightarrow{RT,\ water,\ 60\,mins} Pd/SnO_x \xrightarrow{620\,℃,\ 16\,hrs} PdO/SnO_2 \quad (2.1)$$

The reaction is anticipated to occur due to the standard potential for the reaction as shown in Equation 2.2. Pd(II) salts and surface Sn(II) species will spontaneously react giving Pd(0) and Sn(IV). A more precise galvanic potential would be attained if data was available for specific species: for example the galvanic potential of K_2PdCl_4 is different than that of Pd(II) and SnO is different than Sn(II). However, with the large standard potential calculated the reaction was predicted to be spontaneous even with slight changes in the half potentials.[88]

$$\begin{array}{c} Pd^{2+} + 2e^- \rightarrow Pd\ E^0 = 0.951\ V \\ \underline{Sn^{2+} \rightarrow Sn^{4+} + 2e^-\ E^0 = -0.151\ V} \\ Sn^{2+} + Pd^{2+} \rightarrow Sn^{4+} + Pd\ E^0 = 0.800\ V \end{array} \qquad (2.2)$$

2.3.1 XPS Characterization of Sn standards

An understanding of surface species is required to understand the reaction. Tin oxide was characterized using XPS to satisfy this requirement. Figure 2.1 presents XPS data for Sn, SnO, and SnO_2 standards. Note only the SnO_2 sample showed a dominant single species. Assignments were based on standards and literature precedents. Figure 2.1A shows the XPS of Sn metal after Ar sputtering in the XPS chamber in order to create a clean surface. The $3d_{5/2}$ peak at 484.9 eV was assigned as Sn(0) metal. The following two fitted peaks at 485.7 eV and 486.9 eV were assigned as SnO, and SnO_2, respectively (The $3d_{3/2}$ peak was not fit but has contributions from all three species as well).[89] Figure 2.1C shows the SnO_2 standard, which shows a single $3d_{5/2}$ peak at 486.6 eV which dominates the spectra. This information allowed the fitting of Figure 2.1B, SnO. Although shipped as SnO the received reagent shows three Sn species on the surface. This is likely due to air oxidation, and/or the disproportionation reaction of SnO forming SnO_2 and Sn.[90] Knowing the ~486.6 eV peak to be SnO_2, the lower binding energy oxide must be SnO, at

~485.5 eV. These results are in agreement with literature.[91, 92] It is noted that due to the peak overlap precise quantification of these species is difficult.

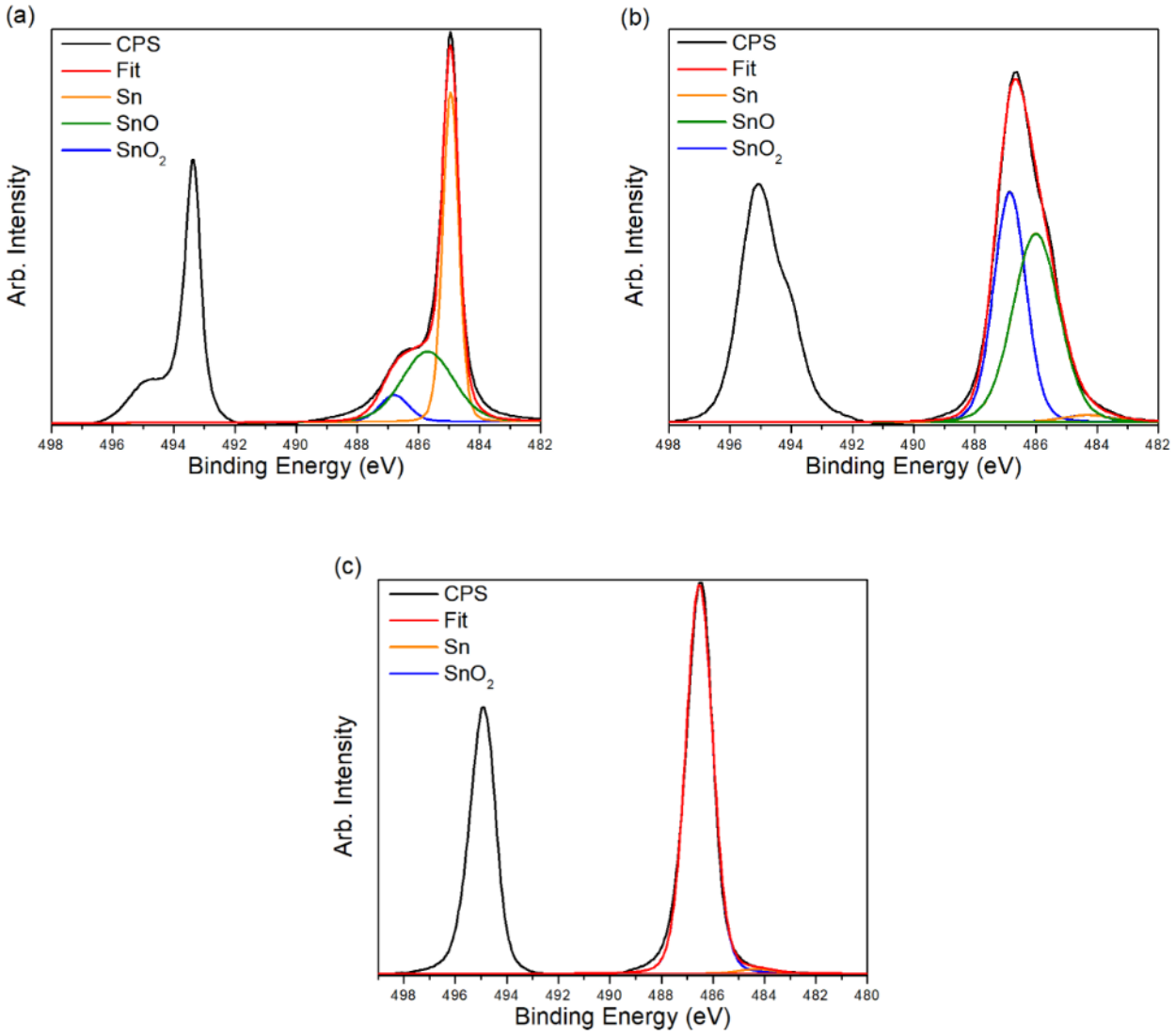

Figure 2.1. XPS Spectra of a) Sn metal standard b) SnO standard and c) SnO_2 standard. CPS indicates the plot of the experimental data in counts per second.

2.3.2 Phase 1: Reduction of SnO

Figure 2.2 presents characterization of SnO immediately before the experiment was conducted. Figure 2.2A shows the powder X-ray diffraction (PXRD) pattern for the sample, as well as the PXRD patterns for SnO and SnO_2. PXRD shows that the sample is predominantly SnO (85 %), although peaks due to SnO_2 (15 %) are also present, presumably due to air oxidation of the sample.

Figure 2.2B shows the 3d XPS spectra of the SnO sample used in the experiments which can be deconvoluted into three peaks: Sn (38 %), SnO (16 %), and SnO_2 (46 %). The significant decrease in SnO concentration from the as-received sample, Figure 2.1B, and the presence of Sn(0) is likely due to disproportionation ($2Sn^{2+} \rightarrow Sn^0 + Sn^{4+}$) and air oxidation of the sample, as this sample has been stored for approximately four weeks before use in the reaction.

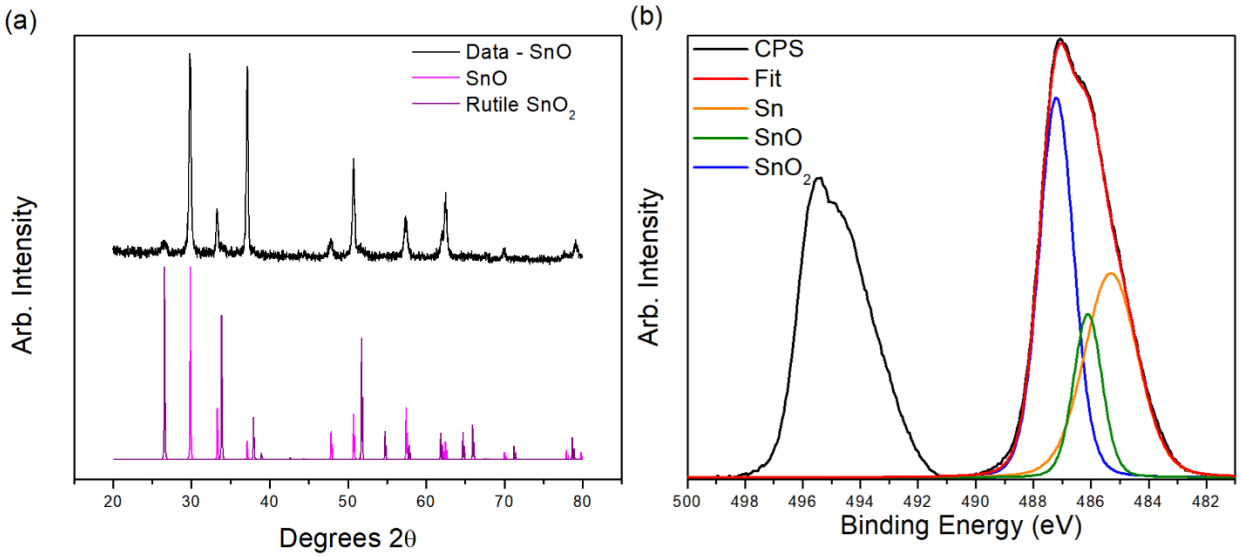

Figure 2.2. a) PXRD patterns of SnO (top-black) and SnO and SnO_2 models (below-colored) and b) XPS of SnO sample before use.

As the intended reaction involved the interaction of Sn(II) and Pd(II) on the surface, attempts to synthesize a pristine SnO surface were made. Figure 2.3 shows the temperature programmed reduction (TPR) of SnO in the presence of a reducing gas. Two features are seen in the TPR plot; a small feature at 250 ºC followed by a large upward curve starting around 350 ºC. These features quantify consumption of H_2, indicating reduction. The 250 ºC peak indicates marginal reduction of the SnO sample, likely the accessible SnO_2 surface species, while the larger feature at 350 ºC and beyond likely indicates bulk reduction of SnO to Sn. With this information, a calcination step at 250 ºC under H_2 was used in order to reduce the surface of the SnO.

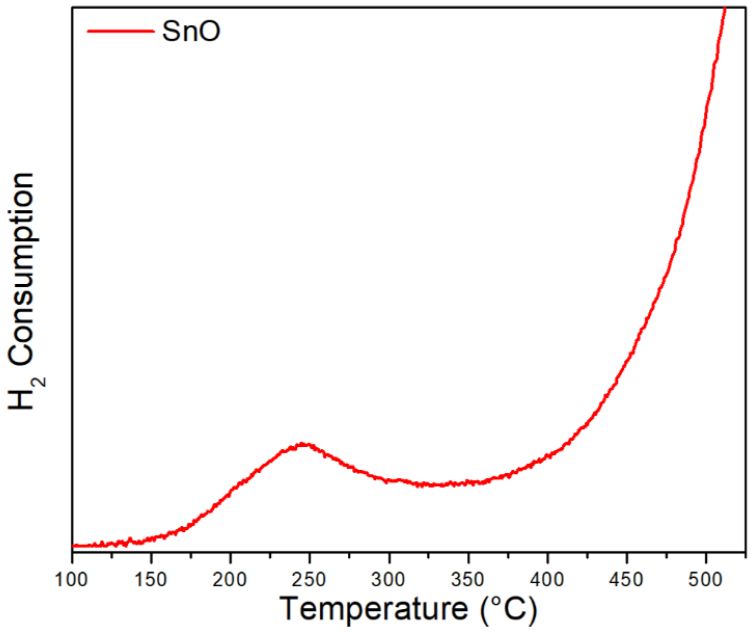

Figure 2.3. Temperature Programmed Reduction of SnO.

Figure 2.4 presents characterization of the SnO sample after exposure to H_2 at 250 ºC. Figure 2.4A shows the PXRD spectra of the sample, and only a marginal reduction of the SnO_2 is seen (13 % vs 15 % previously). However, Figure 2.4B shows the XPS spectra of the treated sample

and shows that the surface is now composed primarily of SnO (SnO at ~486.4 eV, 77.73 %, SnO_2 at ~487.1 eV, 8.42 %, Sn at ~485.5 eV, 13.8 %). Reduction of SnO_2 in this environment was anticipated, however, it is noted that the Sn(0) surface concentration also dramatically declined during the reduction step, which was unexpected. This may have occurred due to the reversal of the disproportionation reaction discussed previously (*e.g.* comproportionation).

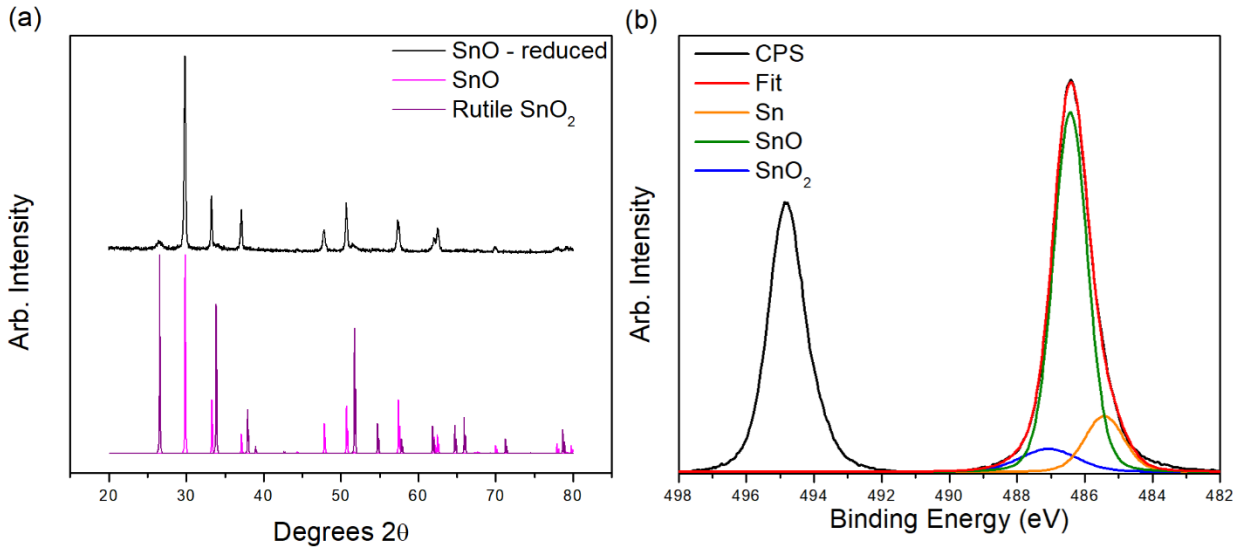

Figure 2.4. Characterization of SnO treated by H_2 at 250 °C; a) XRD patterns of sample and SnO and SnO_2 standards, and b) Sn 3d XPS spectra of reduced SnO.

2.3.3 Phase 2: Galvanic Deposition

After the pre-reduction step, the SnO samples were added to solutions containing K_2PdCl_4 for galvanic deposition reactions. The reaction can be followed by UV-Vis spectroscopy of the Pd species, as shown in Figure 2.5. The concentration of Pd(II) in solution drops rapidly, at the first

available measurement time a dramatic change has occurred as seen by the metal ion to ligand charge transfer (MLCT) transition at 428 nm.[93] 10 seconds indicates a measurement performed as immediantly after addition of SnO to the solution as practical. The sample had to be extracted, centrifuged and measured which was performed immediantly after adding SnO. The reaction rate slows rapidly, possibly due to surface oxidation of SnO competing with the galvanic reaction. Early experiments attempted to use anoxic solvents including freeze pump thaw water and Ar-purged dichloromethane and found no advantages in terms of the relative amount of Pd reduction. As such, the anoxic solvent process was not investigated much further. The rate at which the SnO is passivated by oxidation to SnO_2 is why it is imperative to add the SnO to the Pd(II) solution, as SnO in water will quickly oxidize to a passified particle.

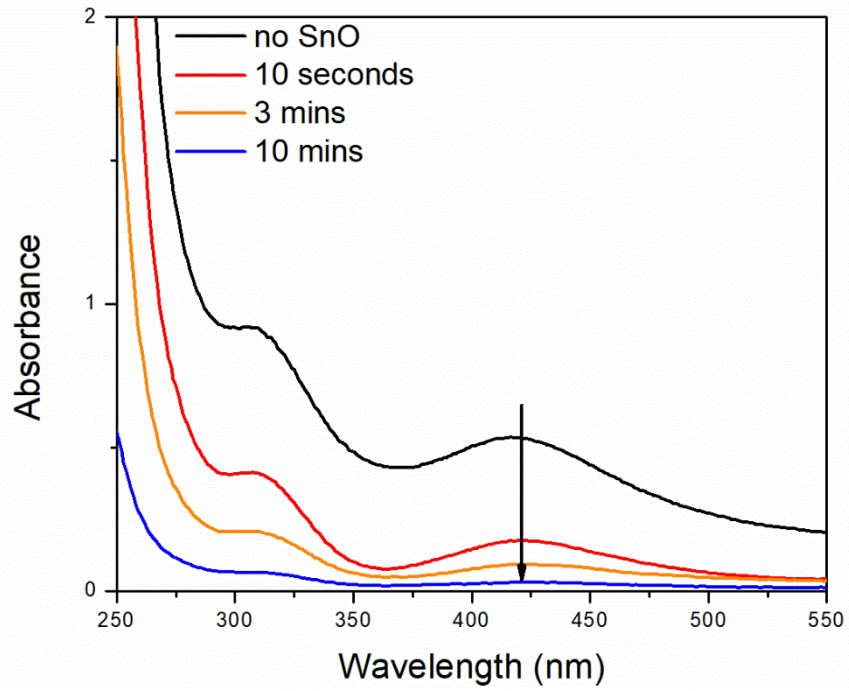

Figure 2.5. UV-vis spectra of aqueous K_2PdCl_4 solution before and after SnO addition.

The reaction was followed by UV-Vis calibration curves, presented in Figure 2.6. Due to the dramatic change in concentrations and the saturation limit of the UV-Vis detector, three features had to be used at varying concentration ranges: the peak at 428 nm (metal-ligand charge transfer MLCT) from 12.5 to 2.5 mM, the peak at 307 nm (another MLCT)[93] from 2 to 0.5 mM and the peak at 208 nm (ligand to metal charge transfer)[94] from 0.5 to 0.024 mM, as shown in Figure 2.6B. As discussed previously the 428 nm and 307 nm peaks are due to MLCT transitions of $PdCl_4^{2-}$. The final peak at 208 nm is due to LMCT of the hydrolysis product of K_2PdCl_4, which is $PdCl_3(H_2O)^-$.[94, 95] These calibration curves allowed following the Pd concentration during the reaction and therefore quantification of the amount of Pd that was removed from solution in each reaction. This quantification is used in future calculations.

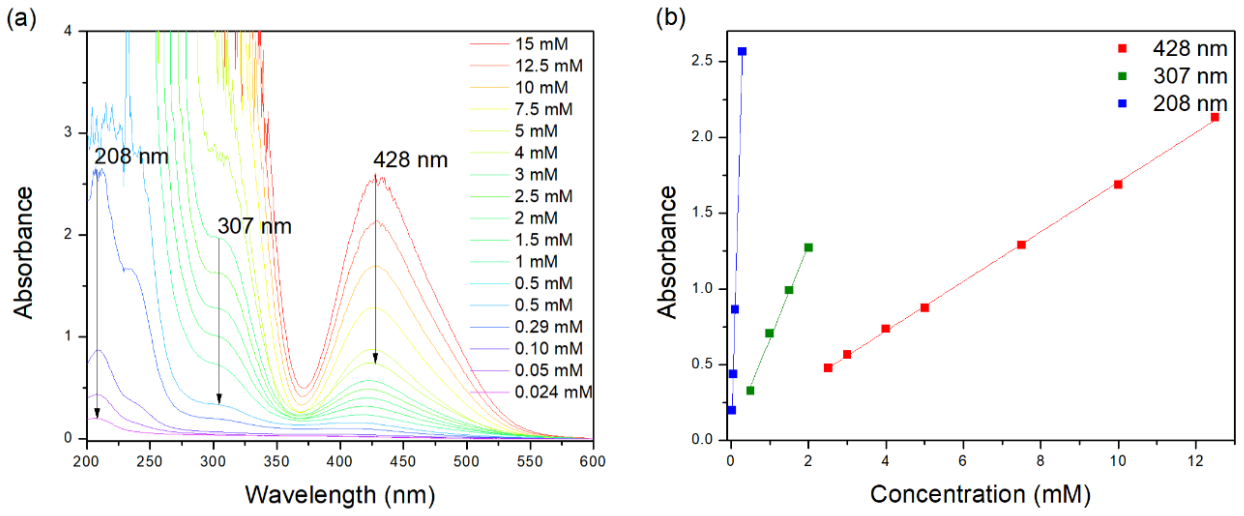

Figure 2.6. a) UV-Vis spectra of aqueous K_2PdCl_4 solutions at varying concentrations, and b) calibration curves for K_2PdCl_4 in water.

Galvanic deposition was performed at three concentrations of Pd in solution along with similar amounts of SnO in each case: Sample 1: 6.0 mM, Sample 2: 0.6 mM, Sample 2-AR (sample-2

using SnO that was not reduced, *i.e.* as-received): 0.6 mM and Sample 3: 0.06 mM. Figure 2.7 presents the UV-Vis results before and after each trial. Sample 2-AR is followed to show the necessity of the previous reduction step. The "before" is measured before SnO was added to the solution. "After" is measured after the reaction has occurred and the Pd/SnO_x has been removed by centrifuge. Recognize that not all of the Pd(II) salt reacted, due to a competitive rate of surface oxidation synthesizing a passivating layer. Also, it is noted that it is possible that the Pd(II) salts may also be being removed from solution by surface adsorption to the SnO particle, perhaps in oxidized regions creating Pd adatoms on SnO_2.[96] This possibility will be discussed later utilizing XPS.

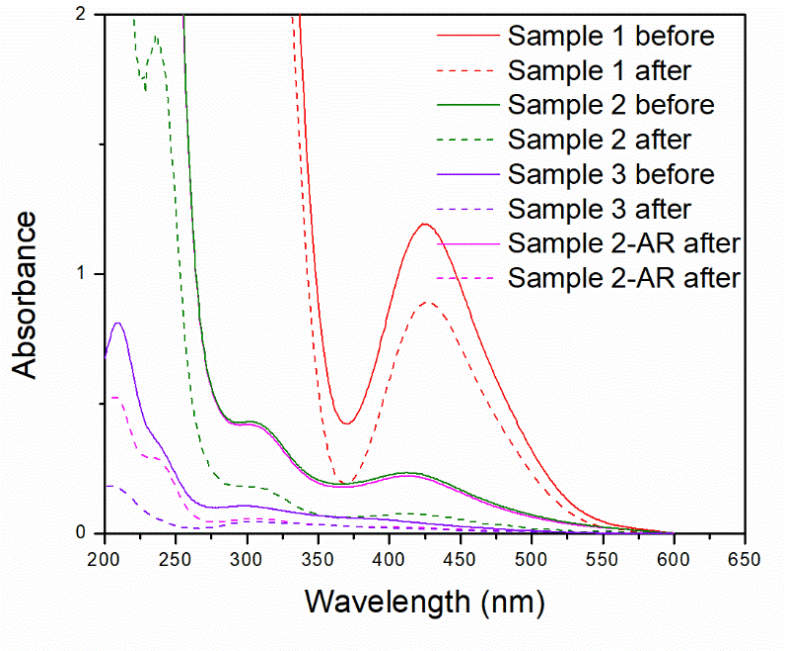

Figure 2.7. UV-Vis spectra of K_2PdCl_4 solutions before and after addition of SnO

Table 2.1 presents the initial and final concentrations of K_2PdCl_4 determined from UV-Vis experiments, along with the mass of Pd that was removed from solution and deposited on the SnO

material. Although the same amount of SnO was added to each sample, in the same volume, for the same amount of time, varying amounts of the Pd were deposited on the particle. This would suggest that varying Pd(II) concentrations could synthesize varying Pd loadings on the SnO, however more work would be required to determine this. Notably, a similar control example to Sample 2 was also attempted tagetting Pd/SnO_2 using SnO that had not been reduced (i.e. was used as received), Sample-2AR. This would be benefiical as it would simplify the synthetic process, however, without reducing the SnO, it was anticipated that less Pd salt would be reduced because less SnO is available on the surface. Perplexingly this was not seen, as this material had the highest incorporation of Pd. This sample was then characterized with the others and will be discussed further.

Table 2.1 Sample names and Pd concentrations used for the galvanic deposition reactions.

	SnO treatment	**Concentration Pd Initial (mM)**	**Concentration Pd Final (mM)**	**Mass Pd Incorporated (mg)**
Sample 1	reduced	6.84	5.04	3.83
Sample 2	reduced	0.61	0.21	0.85
Sample 3	reduced	0.09	0.02	0.15
Sample 2-AR	as received	0.74	0.03	1.51

Characterization of the product was performed by XPS. Three Pd species are anticipated to be possible in this work: Pd, PdO and $Pd(OH)_2$. $Pd(OH)_2$ is a controversial species and was discussed thoroughly in Chapter 1 and will be thoroughly analyzed in Chapter 3. XPS of Pearlman's Catalyst, $Pd(OH)_2$/Carbon, which has a $3d_{5/2}$ peak at ~337.8 eV, was used as a standard for this species as presented in Figure 2.8A.[49] Figure 2.8B presents Pd 3d XPS of a PdO/SnO_2 species. Recognize three peaks, representing Pd (~335.5 eV), PdO (337.0 eV) and Pd(OH)2 (337.9 eV). These values coincide with expected literature values.[97]

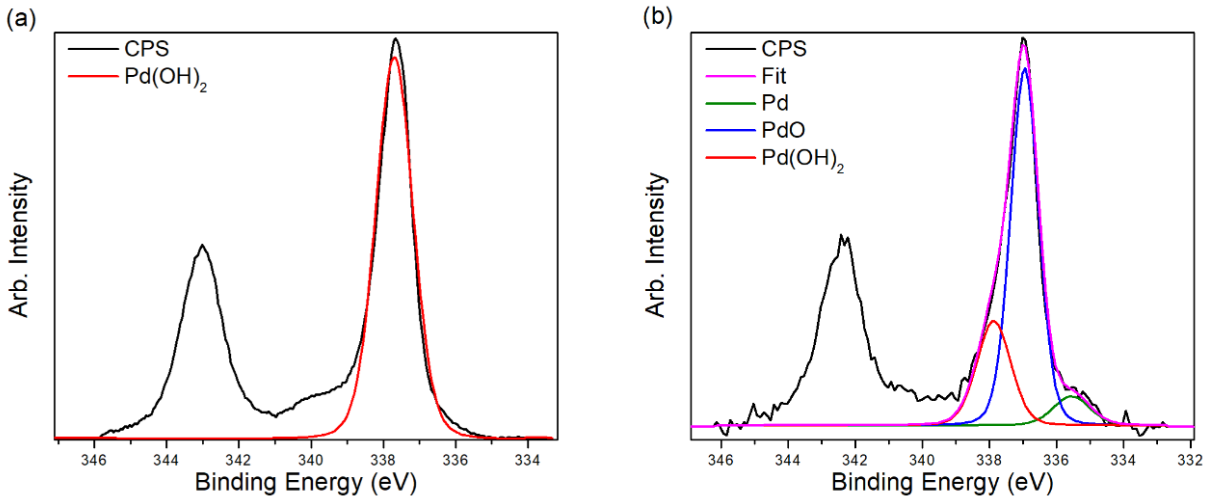

Figure 2.8. Pd 3d XPS standards of a) $Pd(OH)_2$/Carbon b) PdO/SnO_2

Similar results were found for all four concentrations, therefore, only Sample 2 is presented here. Figure 2.9A presents PXRD of the Pd/SnO_x sample. PXRD fitting suggests 76 % SnO, 24 % SnO_2 and 0 % Pd species. Due to the low amount and possibly low crystillinity of Pd deposited in this sample there is no signficant PXRD peaks for the Pd species. Figure 2.9B shows the Sn 3d XPS results, sensitive only to surface species; three $3d_{5/2}$ contributions are seen: SnO_2 (487.4 eV, 85.6 %), SnO, (486.1 eV, 11.5 %), and Sn (484.9 eV, 2.9 %). The large amount of SnO_2 seen in the XPS is likely primarily due to surface oxidation by dissolved oxygen in solution, along with a secondary oxidation due to the galvanic reaction with Pd. The large amount of SnO_2 on surface explains why further spontaneous galvanic interactions did not occur. Figure 2.9C shows the Pd 3d XPS results; the Pd $3d_{5/2}$ peak could be fit to three species; Pd (335.4 eV, 56.2 %), PdO (336.5 eV, 15.1 %) and $Pd(OH)_2$ (337.7 eV, 28.7 %). The majority of the Pd signal by XPS is Pd(0), which shows that the galvanic reaction is likely occuring. However, Pd(II) salts adsorbed

to the surface could also show a decrease in Pd salt concentration by UV-Vis but should then show strong Pd(II) features in the XPS. Adsorbed Pd(II) salts likely account for some of the species defined as $Pd(OH)_2/PdO$, though it is likely that ambient Pd oxidation by air also leads to some $Pd(OH)_2/PdO$ formation. Cl is present in the XPS survey spectrum of Pd/SnO_x, indicating some Cl species are still present, either as adsorbed ions or still coordinated with Pd salts.

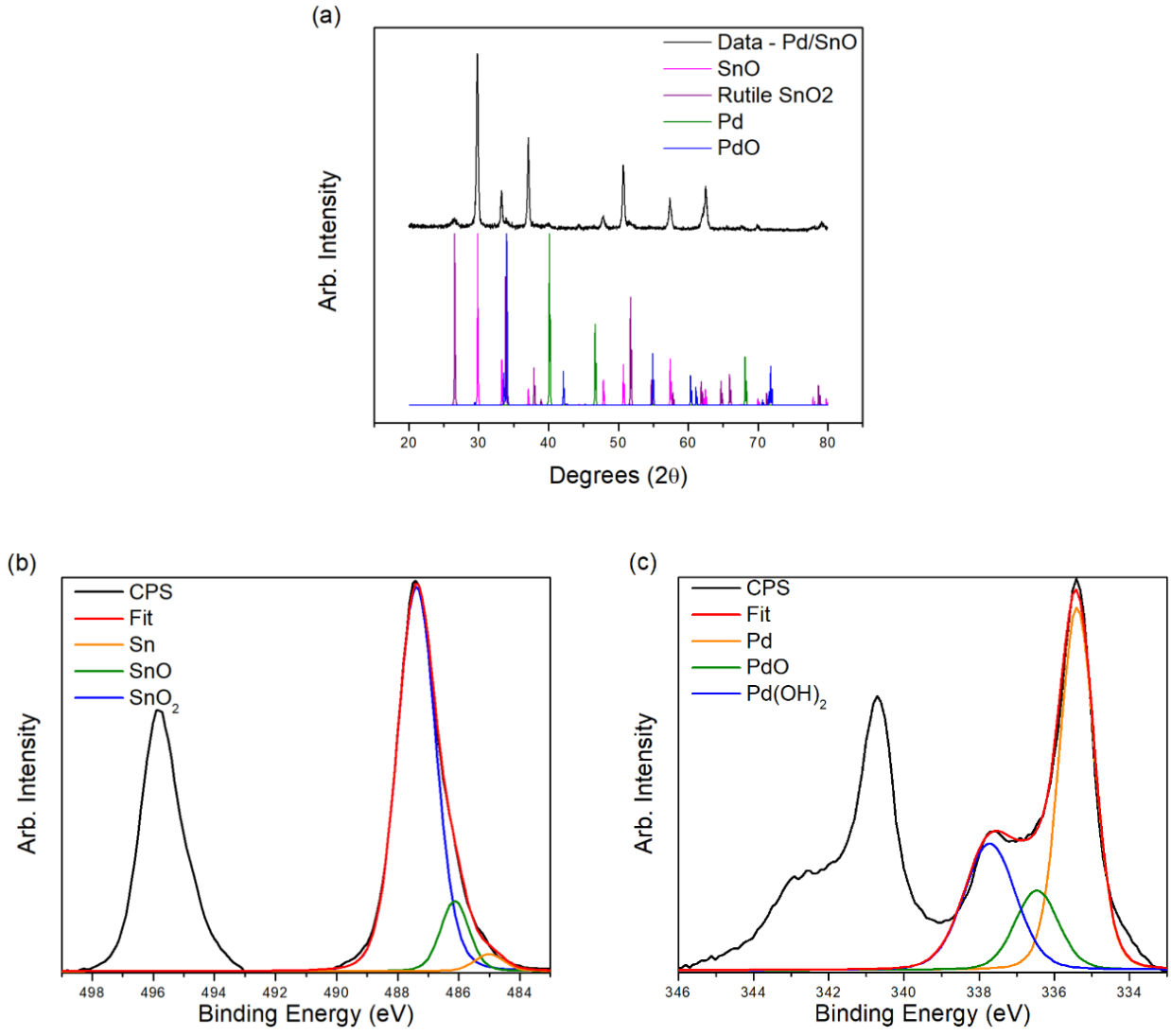

Figure 2.9. a) PXRD of Pd/SnO_x b) Sn 3d XPS of Pd/SnO_x and c) Pd 3d XPS of Pd/SnO_x. The Pd/SnO_x sample shown is Sample 2.

CO Chemisorption data is presented in Table 2.2. CO chemisorption relies on CO adsorption to metals, and not to metal oxides. Therefore, before each CO chemisorption measurement, the sample was fully reduced to Pd metal using forming gas (5 % H_2 in N_2) at 100 ºC. Dispersion results measure the total CO adsorbed by the sample and thus measures the number of available surface Pd sites (assuming 1:1 Pd:CO stoichiometry). This value is divided by the total Pd amount, to give dispersion. The higher the dispersion, the smaller the average Pd nanoparticle size. Overall Pd mass calculations were based off of calculated loading from the calibration curves discussed above. Particle size measurements from dispersion data are rough calculations, which have many built-in assumptions, a typical assumption is that the Pd nanoparticles are hemispherical particles. However, varying particle shapes are possible, especially with the galvanic deposition method and with the interaction between the metal and metal oxide.[41, 98] A second assumption is that all Pd surface sites are available for CO bonding. If secondary adsorbates such as chloride are on the surface, this will lower dispersity data and suggest that the system has larger NP sizes. This means potentially signficant errors are associated with the particle size calculations, although they still allow simple comparisons between samples. Although CO Chemisorption has these issues it was the best available technique as electron microscopy, the more conventional technique to analyze particle size, was not readily useable due to the small atomic number difference of $_{46}$Pd and $_{50}$Sn. The consequence of the small difference is that in conventional electron microscopy the contrast between the two atoms is nearly indistinguishable.

The results in Table 2.2 show that dispersion increases and particle size decreases with decreasing concentration of Pd on the SnO. With less Pd in the solution it is anticipated that smaller particles would be synthesized. However, two anomalies were also seen. Firstly, the calculated particle sizes are very large, suggesting that adsorbed Cl is not being removed in the reduction step

and could be problematic. Secondly, the untreated SnO sample had the highest dispersion, and thus the smallest particle size. This is investigated further in the following section.

Table 2.2 CO Chemisorption data of Pd/SnO_x at different loadings.

	Particle Size (nm)	**Dispersion (%)**
Sample 1	334.6	0.33
Sample 2	137.8	0.81
Sample 3	60.8	1.84
Sample 2-AR	53.6	2.09

2.3.4 Phase 3: Oxidation of Tin (II) Oxide

Thermogravimetric analysis (TGA), presented in Figure 2.10, was utilized to determine the oxidation temperatures required to oxidize the catalyst from Pd/SnO_x to Pd/SnO_2, a more conventional catalyst. This is done to synthesize a catalyst that can be compared to other synthesis methods in literature. Two notable features are seen in the TGA data, a small mass increase with plateau at 450 ^oC, which is the oxidation of Pd to PdO and a significantly more dramatic feature beginning around 500 ^oC, which corresponds to the oxidation of SnO to SnO_2. From this graph, it was determined that calcination at 650 ^oC for 16 h should be sufficient to completely oxidize the SnO in the sample. This process also oxidizes the Pd, giving a final product of PdO/SnO_2.

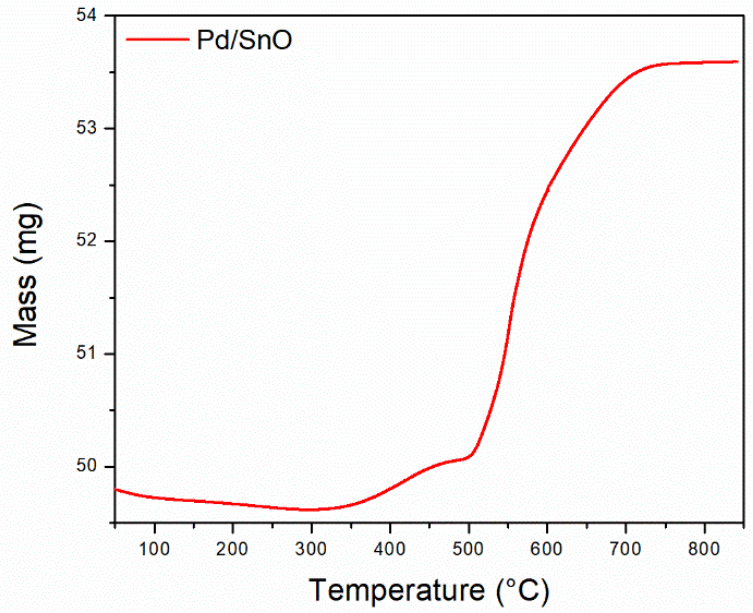

Figure 2.10. Thermogravimetric analysis of Pd/SnO_x (Sample 2).

After heating the sample at 650 ºC for 16 h, the sample was characterized by XRD and XPS. Figure 2.11A shows the PXRD pattern for sample 1, which shows that the product is a composite of PdO and SnO_2. Quantification of the PXRD pattern gives the following atomic percentages: SnO (5.6 a%), SnO_2 (92.6 a%), PdO, (1.6 a%) and Pd (trace). This represents a 1.3 w/w % $Pd:SnO_2$. While the concentration of Pd species are below the reliable detection limits of XRD, they were consistently modeled by XRD software and are in fair agreement with the calculated Pd to SnO_2 w/w % of 1.6 % (which was calculated based off calibration curves and SnO mass used). Figure 2.11B shows the 3d Sn XPS spectra of the sample, which shows a dominant peak for SnO_2 at 487.1 eV. Figure 2.11C shows the 3d Pd XPS data, depicting small amounts of both Pd (335.5 eV, 7.3 %) and $Pd(OH)_2$ (337.9 eV, 24.1 %) with the remainder present as PdO (337.0 eV, 68.6 %). The Pd is likely an artefact formed by X-ray photoreduction of the PdO.[99] $Pd(OH)_2$

species are likely synthesized when cooling the PdO/SnO_2 species back to room temperature, at which point water may adsorb to the surface and produce $Pd(OH)_2$.

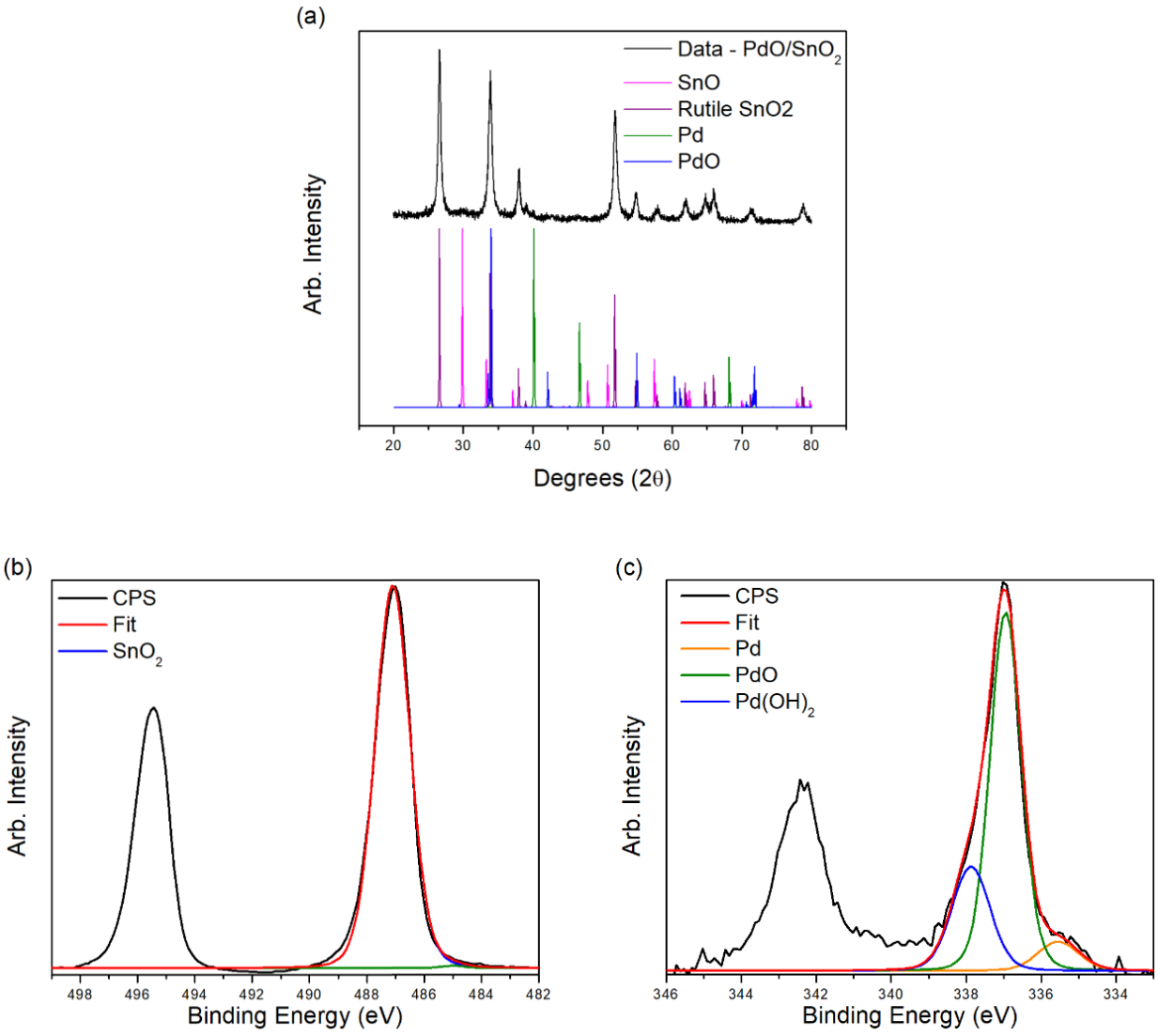

Figure 2.11. Characterization of Pd/SnO_2 treated by air at 650 ºC a) PXRD b) Sn 3d XPS and c) Pd 3d XPS.

Finally, CO Chemisorption was performed on the Pd/SnO_2 product (after another reduction of the PdO to Pd), and results are shown in Table 2.3. Compared to the Pd/SnO_x sample, the Pd dispersion became greater, and thus the calculated particle size became smaller after the oxidation

step, as predicted by SMSI.[41] This is likely due to a strong metal-metal oxide interaction between the two surfaces, allowing the Pd to "wet" the SnO_2 surface. Notably, the benefit of pre-reducing SnO is seen at this stage: the final Pd dispersion is significantly higher in the pre-reduced SnO samples. It is not clear why dispersion data shows such dramatic changes; Pd particle dispersion is likely not increasing solely due to Pd particles fragmenting into smaller particles upon heating. Due to the favorable Pd-SnO_2 interactions the particles are likely to be wetting the surface, creating a thinner particle geometry which would be perceived as a decrease in particle size and increase in particle dispersion by the chemisorption process. This wetting process may be a possible reason for the increase in dispersion. Also, the Pd/SnO_x sample showed Cl in the XPS survey spectrum and the Pd/SnO_2 did not, which is beneficial as chloride ions may retard catalytic activity. Chloride anions adsorbed on the Pd surface are likely skewing the chemisorption data for the Pd/SnO_x, whereas the Pd/SnO_2 dispersion results are a truer picture of the relative Pd dispersion. These dispersion values are similar to modern literature values for dispersed Pd on SnO_2 catalysts, which vary from 1-40 % dispersion.[100,46, 101]

Table 2.3 CO Chemisorption of Pd/SnO_x and Pd/SnO_2.

	Pd/SnO_x		**Pd/SnO_2**	
	Particle Size (nm)	**Dispersion (%)**	**Particle Size (nm)**	**Dispersion (%)**
Sample 1	334.6	0.33	42.3	2.65
Sample 2	137.8	0.81	8.7	12.94
Sample 3	60.8	1.84	4.9	22.91
Sample 2-AR	53.6	2.09	14.8	7.59

2.4 Galvanic Deposition: Pd/Fe_2O_3

Pd/SnO_2 was the case study of the galvanic deposition method as presented above. However, the protocol can be applied to a variety of systems. Herein, is a brief discussion of the synthesis of Pd/Fe_2O_3. This is done to show the generalizability of the galvanic deposition protocol. FeO nanoparticle synthesis was conducted using a thermal decomposition method of $Fe(acac)_3$ in an oleic acid/oleylamine solvent. Similar to the SnO system, an immediate concern was surface oxidation of the FeO nanoparticles. Figure 2.12 shows XRD, XPS and TEM analysis before Pd addition. XRD shows the presence of Fe_3O_4 and FeO which was corroborated by XPS. The $2p_{3/2}$ Fe XPS was fit using an established literature procedure.[102] The presence of Fe_3O_4 was not expected, however, two possible pathways have been suggested for it: the Fe_3O_4 may be a side product of the reaction, or it may form from surface oxidation of FeO which occurred either by remnant oxygen in the reaction mixture or exposure to air between the synthesis and measurement. The prevalence of both Fe(II) and Fe(III) in a ratio close to that of Fe_3O_4 in the XPS suggests that Fe_3O_4 comprises most of the surface of the particles. The TEM image of the nanoparticles shows that the FeO particles are relatively monodisperse at 6.1 ± 1.4 nm and uniform in shape.

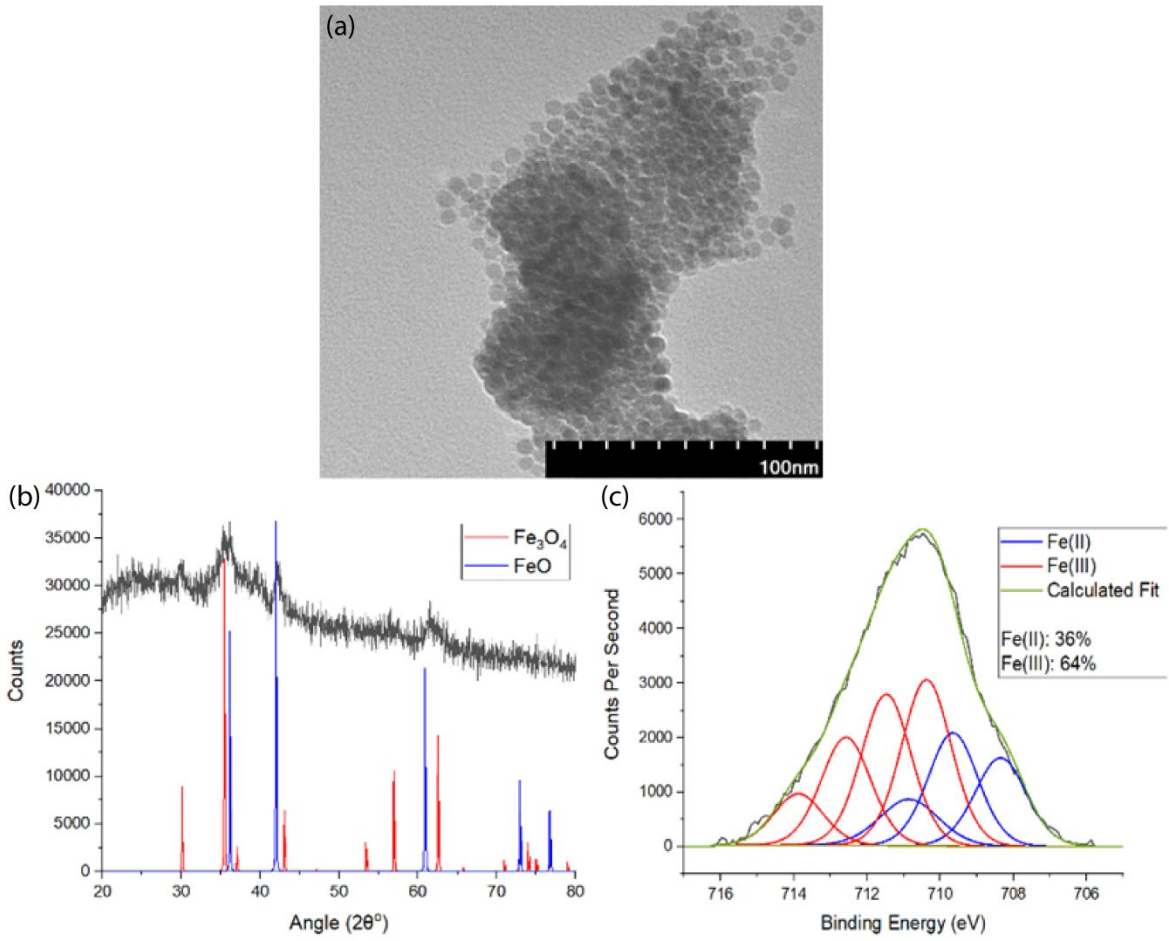

Figure 2.12. Characterization of FeO nanoparticles; a) TEM, b) XRD, and c) Fe $2p_{3/2}$ XPS.

Figure 2.13 contains the characterization data for the Pd/FeO product. Counterintuitively, the Fe 3d XPS data suggests the Fe was reduced in this process, however, XPS of Pd 3d shows Pd metal was deposited on the FeO particles. Furthermore, as seen in TEM, the Fe oxide nanoparticles have also slightly expanded in size to 7.8 ± 1.3 nm. The surface reduction of the FeO may be attributable to the synthetic process, however, Pd(II) salts are being reduced by the FeO, thereby it was anticipated that the FeO would be oxidized. As can be seen in the TEM image small particles approximately 1.5 ± 0.5 nm are seen decorating the FeO nanoparticles. Due to their size and relative electron density these small particles are believed to be synthesized Pd nanoparticles.

However, they seem to be localized in several areas of the sample. Therefore, while Pd/Fe oxide was produced, showing the generalizability of the galvanic deposition protocol, it is apparent more work needs to be done to ensure that well-dispersed samples can be made by this technique.

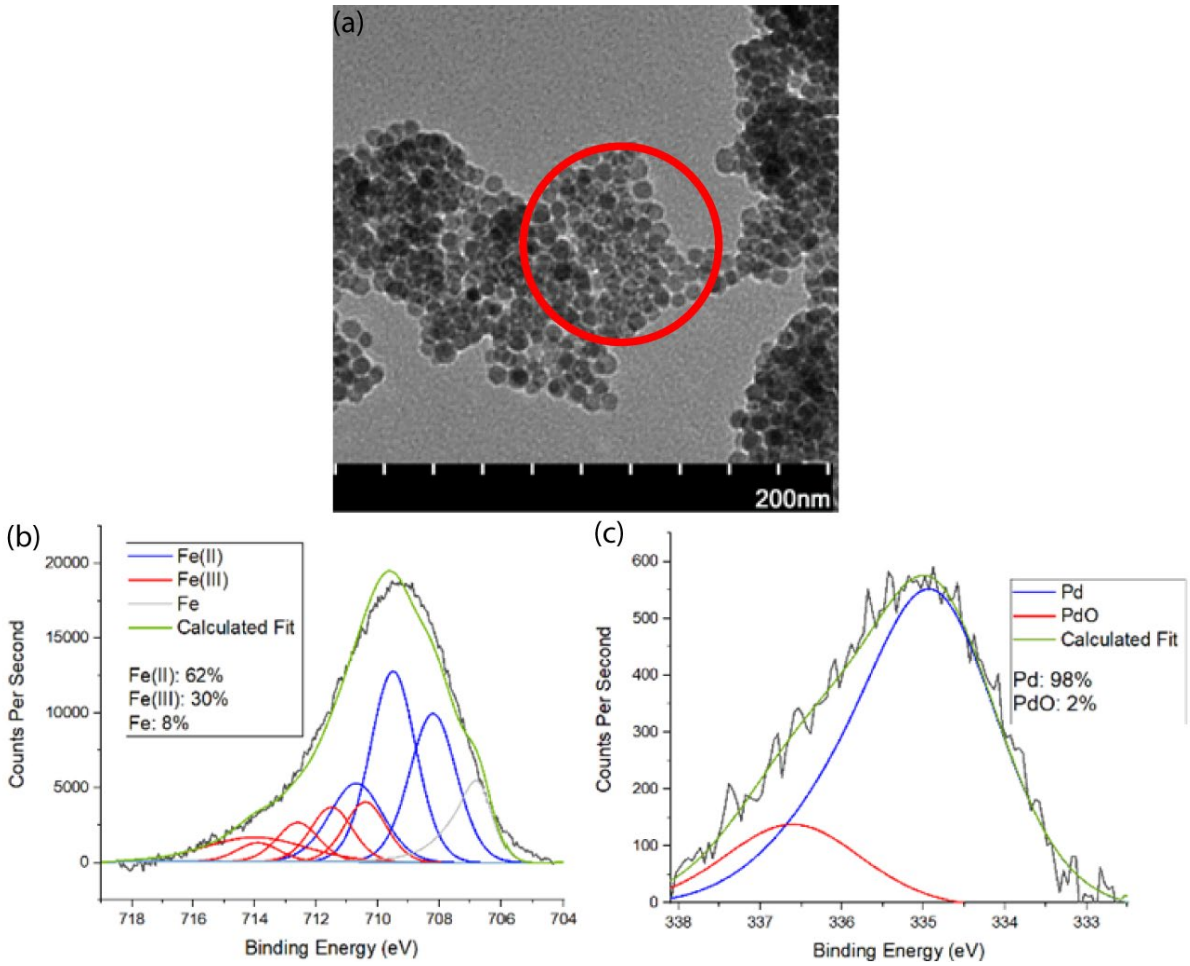

Figure 2.13. Characterization of Pd/FeO nanoparticles ; Fe $3p_{3/2}$ XPS, Pd 3d XPS and TEM.

2.5 Conclusions

Galvanic deposition, involving a spontaneous redox reaction between a metal oxide and a metal salt, is a novel synthesis technique designed to simply and cleanly decorate metal oxide supports with metal nanoparticles. The deposition of Pd(II) salts onto SnO materials was used to test the galvanic deposition concept. Surface reduction of Sn (II) oxide was analyzed using TPR. XPS, XRD and chemisorption data of the final Pd/SnO_x all confirmed that galvanic deposition of Pd was taking place. Chemisorption data suggested that large Pd nanoparticles were on the support, which was now primarily SnO_2 on the surface. Final oxidation to Pd/SnO_2 was performed, and characterization of the products showed a beneficial morphology change of the Pd during the oxidation step, leading to the synthesis of highly dispersed Pd on SnO_2. Data for an analogous Pd/FeO synthesis was also briefly presented in order to show the generalizability of the galvanic deposition protocol.

Chapter 3 *In Situ* Speciation of Methane Oxidation Catalysts[2]

3.1 Introduction

Energy resource requirements for the future will vary, however, renewables alone will likely not be feasible as the only source of energy. [1] Petroleum, coal and natural gas, collectively referred to as hydrocarbon fuel sources, will most likely be a part of both the short and long term energy strategy: responsible use of these hydrocarbons is paramount. When quantified in gram carbon emitted per energy extracted, natural gas, is the most responsible of these hydrocarbons due to the efficiency of its combustion and has been implemented successfully in power plants and natural gas vehicles.[103, 104] Yet, a complication of methane is that it has 21 times more of a greenhouse gas potential than carbon dioxide.[5] Therefore, the responsible use of natural gas requires mitigating the amount of methane released to the environment. Efficient and complete combustion is the primary strategy, but effluent gases still contain methane, so a technique is necessary to oxidize this methane to carbon dioxide before release.

Pd and Pt are the most studied active catalysts for methane oxidation, in this study the focus will be on Pd catalysts.[9] Multiple difficulties for this catalyst exist, among them is the expected environmental conditions that the catalyst will operate in. A benefit of combusting methane in these environments is its ability to be burnt lean, i.e. in the presence of an excess of air, thus

[2] This project was performed in collaboration with Dr. Natalia Semagina's group at the University of Alberta's Chemical Engineering Department. Synthesis of Pd/Al_2O_3 and Pd/SnO_2 was performed by Dr. Jing Shen, a post doctoral fellow of Dr. Natalia Semagina. Pd/CoO_x was synthesized by Somaye Nasr, a PhD candidate with the group. Temperature Programmed Reduction and catalytic activity experiments were performed by Dr. Jing Shen. Pd/Al_2O_3 Pd K edge data was collected by Dr. Kee Eun, a previous group member, while data processing was performed by myself. All other XAS work and the writing of this chapter was performed by myself.

The Pd/SnO_2 related work has been accepted and published (Barrett, W.; Shen, J.; Hu, Y.; Hayes, R. E.; Scott, R. W. J.; Semagina, N., Understanding the role of SnO_2 support in water-tolerant methane combustion: In situ observation of $Pd(OH)_2$ and comparison with Pd/Al_2O_3. ChemCatChem, https://doi.org/10.1002/cctc.201901744) and the Co work is in the process of being written for publication.

reducing the amount of NO_x and SO_x expected as compared to the burning of heavier hydrocarbons.[105] However, a catalyst is still required to oxidize flue gas methane before release into the environment. Implementation of the catalyst into the gas stream of natural gas vehicles or natural gas power plants will present a variety of temperatures and mixed gas species. Pd catalysts are well-known to be poisoned by water due to the reversible reaction of $PdO + H_2O \rightleftharpoons Pd(OH)_2$.[105] PdO, is the active catalyst for methane oxidation. Below approximately 500 ºC $Pd(OH)_2$ is produced, forming a passivating layer, retarding catalytic activity.[106, 107] The water desorption temperature varies dramatically depending on catalyst design.[37] Therefore, systems can, and should, be designed to overcome this adversity.

The oxidation of methane to carbon dioxide produces water, so drying effluent gases before catalysis is not a complete solution as produced water can adsorb to the surface.[108] Therefore, catalyst design becomes the most feasible solution to the $Pd(OH)_2$ problem. Some successes have been found through synthesis of bimetallic Pd species.[109] This work focuses on the alternative use of supports that allow for strong Pd-metal oxide interactions, otherwise known as the Strong Metal Support Interaction (SMSI) effect.[41] Previously supports such as Al_2O_3 or SiO_2 have been used as these supports are common, inexpensive and inert. However, the use of redox-active supports such as SnO_2 and CoO_x have been shown to have beneficial effects as they can activate oxygen at moderate temperatures.[50] Sekizawa *et al.* discussed low methane oxidation on Pd/SnO_2 catalysts recognizing that the catalytic activity was highly dependent on the synthesis and design of the catalyst. They contrasted the system against Pd/Al_2O_3 for work under humid conditions and, although poisoning was seen it was dramatically lower than the water poisoning of the Pd/Al_2O_3 system.[85] Ercolino *et al.* described the benefits of a Pd/Co_3O_4 catalyst, recognizing relatively low total methane oxidation temperatures (compared to Pd/Al_2O_3) and that the Co_3O_4 assisted catalytic

activity by generating active oxygen species in the catalytic environment.[110] The difficulty becomes quantifying the differences between the Pd-PdO-$Pd(OH)_2$ equilibrium on a variety of supports in methane oxidation environments. Because the supports are influencing the catalytic activity is it presumed that they are influencing this equilibrium, and thereby it becomes necessary to quantify this equilibrium on a variety of supports *in situ* in order to compare the metal oxide contribution to the catalyst.

This work presents and discusses the use of *in situ* X-ray absorption spectroscopy (XAS) at both the Pd L and K edges to compare and quantify the Pd-PdO-$Pd(OH)_2$ equilibrium on different metal oxide supports. Pd nanoparticles on three different supports are compared: Al_2O_3, SnO_2, and CoO_x. Sn L-edge and Co K-edge XAS are also examined to determine whether changes in the Pd chemistry are linked to changes in the chemistry of the underlying support. Distinguishing between PdO and $Pd(OH)_2$ *in situ* poses challenges primarily due to the similarities in oxidation states. However, the long-range coordination environment of PdO and $Pd(OH)_2$ are different and therefore X-Ray Absorption Near Edge Spectroscopy (XANES), a component of XAS, is a powerful tool to differentiate the species. Linear Combination Fitting (LCF), a statistical method for fitting weighted components to experimental data, has been utilized as a tool to extract the species abundance information from the collected data.

3.2 Experimental

3.2.1 Materials

Palladium (II) acetate ($Pd(AcO)_2$), poly N-vinylpyrrolidone (PVP, average molecular weight 40,000), gamma alumina (γ-Al_2O_3, average pore size 58 Å, SA 155 m^2/g), tin dioxide (SnO_2, 325 mesh, 99.9 % trace metals basis), tin(II) oxide (SnO, ≤ 60 micro particle size, powder, 97 %)

were purchased from Sigma-Aldrich. Ethylene glycol (>99.9 %) was purchased from Fischer Scientific. Cobalt powder, spherical -100+325 mesh 99.8 %, cobalt(II) oxide, 95 %, and lithium cobalt(III) oxide, 97 %, was purchased from Alfa Aesar. 1000 ppm methane in nitrogen and 5 % hydrogen in nitrogen and all other gases were purchased from Praxair.

3.2.1.1 Pd/MO Wet Impregnation

PVP-stabilized Pd nanoparticles were synthesized by a polyol reduction method,[111] with minor modifications.[57] To prepare Pd nanoparticles, $Pd(AcO)_2$ precursor (0.4 mmol, 0.090 g in 20 mL dioxane) and PVP (16 mmol, 1.776 g, PVP/Pd molar ratio 40/1) were dissolved in 200 mL ethylene glycol, under vigorous stirring, in a 500 mL three-neck round bottom flask. The solution was stirred and refluxed for 3 h under air environment. The dark brown colloidal solution of PVP-Pd nanoparticles obtained after reaction was cooled down naturally to room temperature. Pd nanoparticles were deposited on commercial oxide supports (SnO_2, γ-Al_2O_3 and Co_2O_3) by cold acetone precipitation with desired Pd loading of 0.3 w/w %. After the deposition process, Pd/SnO_2, Pd/γ-Al_2O_3 and Pd/Co_2O_3 catalysts were washed three times by acetone to remove ethylene glycol completely, followed by drying in an oven at 60 °C overnight. Prior to combustion reactions and catalyst characterization, all samples were calcined at 550 °C for 16 h in a furnace under static air. The dispersions for each system measured by CO Chemisorption were: Pd/SnO_2 16 %, Pd/Al_2O_3 40 % and Pd/CoO_x 12 %.

3.2.2 Methods

3.2.2.1 Temperature Programmed Reduction

Temperature Programmed Reduction (TPR) was performed using an Autochem unit with 5 % H_2/He flow at 20 mL/min at temperature ramping rates of 10 ºC/min. Hydrogen consumption was quantified by mass spectrometry. 0.5 g loadings were used.

3.2.2.2 X-Ray Photoelectron Spectroscopy

XPS was performed using a Kratos AXIS Supra system at the University of Saskatchewan, Saskatchewan Structural Sciences Centre. A 500 mm Rowland circle monochromated Al K-α (1486.6 eV) source was utilized in tandem with a hemi-spherical analyzer and spherical mirror analyzer. A 300 x 700 micron spot size was used. High resolution scans (presented) utilized 0.05 eV step sizes with a pass energy of 20 eV. The accelerating voltage was 15 keV with an emission current of 15 mA. XPS calibration was performed using adventitious carbon 1s peaks calibrated at 284.8 eV. XPS data was analyzed with CasaXPS.

3.2.2.3 *In situ* Characterization of Methane Oxidation Catalysts

An *in situ* X-ray Absorption Spectroscopy (XAS) cell was used at the Canadian Light Source (CLS) on the SXRMB and HXMA beamlines. This cell allows measurements of materials through transmission and/or fluorescence measurements at different temperatures and in different gaseous environments using both hard and soft X-Rays. The Pd L edge and K edge spectra were collected on the Soft X-ray Microcharacterization Beamline (SXRMB) and the Hard X-ray Microanalysis (HXMA) beamline, respectively, at the Canadian Light Source. Sn L and Co K edge data were collected on the SXRMB beamline. In the case of SXRMB (Pd L and Co K edge) data, the system was immersed in He, without changing the temperature, immediately before the measurements

were taken in order to reduce scattering on the incident and fluorescing photons, and *in situ* conditions were resumed immediately after data collection. After normalization and energy calibration data was analyzed by linear combination fitting (LCF) using IFEFFIT in the Demeter software package (Athena).[67] Three species were used as references for the fitting: reduced Pd on metal oxide, oxidized PdO on metal oxide (support dependent *i.e.* Pd/SnO_2 standards were PdO/SnO_2 and Pd/SnO_2), and Pearlman's Catalyst $Pd(OH)_2/C$. The fit boundaries were set from -15 to +40 eV covering the X-Ray Absorption Near Edge Structure (XANES) region of the XAS spectra, sums were not forced to equal 1 (as another reliability check of the LCF data) and E_0 was fixed after the calibration and alignment of data.

The cell allows *in situ* data collection using the setup presented in Figure 3.1. At the top and bottom of the cell are two platinum heaters (red), contained in ceramic plates to assist in heat distribution. Each of these heaters has a respective thermocouple and a third thermocouple is above the bottom heater, where the sample is placed. The cell has three windows, two in line with the beamline for transmittance measurements and one perpendicular to the beamline for fluorescence measurements. The sample holder is designed to hold a pellet at a 45-degree angle such that photons can be detected by the fluorescence detector and, at the same time, transmittance measurements can be conducted. This is beneficial as both detection measurements have their limitations and therefore the best measurement for the specific sample can be determined once the sample and equipment has been set up. The cell is airtight, each window being covered with film and the lid has an O ring and screws that create a seal. The lid and bottom of the cell have plumbing to allow gases to be introduced to the cell. The whole cell is cooled via a water cooling pump that moves water throughout the cell body such that the cell is cool to the touch even when the inside of the cell is at 450 ºC. Flanges can also be added to the cell which connect with the beamline.

This is used in soft X-Ray measurements, as the flanges can be filled with He. Even in this configuration, the cell can be filled with reaction mixture gases to immerse the catalyst in the environment of interest leading up to the measurement. The cell is then immersed in He immediately before measurements at energies below 4 keV (soft X-Rays, SXRMB beamline). In Figure 3.1A the schematic is presented which includes the He tank, in the case of hard X-Rays the setup is almost the same, however, does not include the He tank.

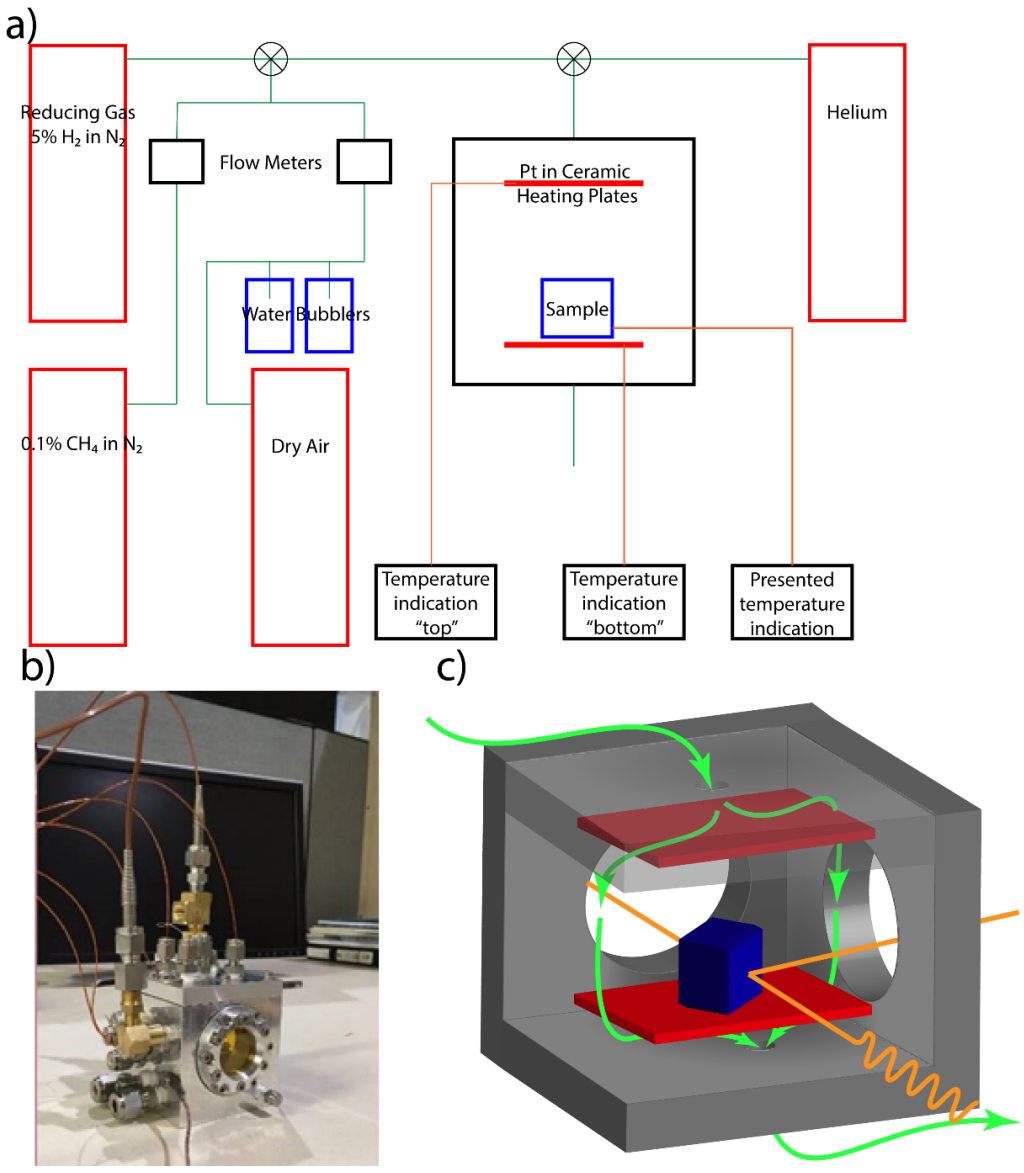

Figure 3.1. a) Depiction of experimental set-up b) image of cell c) graphic of cell in which green arrows indicate gas flow and orange arrows indicate the path of X-Ray radiation.

The sample was loaded into the *in situ* cell which was then sealed and heated to 300 ºC at 10 ºC/min with positive pressure of the reducing gas mixture (5 % H_2 in N_2). The system was held in this state for 10 mins before being cooled, under the reducing gas mixture, to 100 ºC. At this point the gaseous environment was changed to methane/air mixtures for the *in situ* experiment. 0.1 % CH_4/N_2 and dry air were used at flow rates of 154 and 103 mL/min respectively. The dry air was flowed through two bubblers to saturate it before mixing with the methane mix. A scan was then taken, of both the metal and metal oxide, (giving reduced Pd/MO standard) and the temperature was then increased by 50 ºC at 10 ºC/min. The system was then allowed to equilibrate for 10 minutes before measurements. This process was repeated until temperatures of 450 ºC. In soft X-Ray experiments (<4 keV) the cell was immersed in helium immediately before the measurement is taken and the *in situ* gases displace the helium immediately after the measurement.

All standards other than reduced Pd/MO were measured at room temperature under ambient gases. Co standards were cobalt powder, Co(0), cobalt(II) oxide, for Co(II), and lithium cobalt(III) oxide, for Co(III). SnO and SnO_2 were standards for the tin oxides. The PdO standard was synthesized during calcination of the catalyst, and thereby a measurement was taken at room temperature under ambient gases of each PdO/MO to be used as a PdO standard. Pd/MO standards were synthesized by the reduction step discussed above and the measurement was taken at 100 ºC before immersing the system in the *in situ* gas mixture.

Collected data was imported to Athena with its foil reference. Both the data and foil reference were normalized. Following this all foil references were aligned, which allows for calibration of the data. For Linear Combination Fits, all R-factors were less than 0.011, typical R-factors were less than 0.005. All data manipulation was performed following accepted practices as documented in the Athena XAS Data Processing online manual.[67]

3.3 Results and Discussion

3.3.1 Palladium

3.3.1.1 Defining *In Situ* Standards

Three standards were required for the Pd speciation: Pd, PdO and $Pd(OH)_2$. Since the target species is a supported nanoparticle, standards would ideally be supported nanoparticles. Therefore, conditions were designed such that Pd/MO (MO for generic metal oxide) and PdO/MO were synthesized and measured in the cell, and used as standards for Pd and PdO, respectively. A pathway for uniform production of $Pd(OH)_2$/MO was not as clear and therefore, a separate sample of commercial $Pd(OH)_2$ was used as a standard for $Pd(OH)_2$.

The Pd/MO standard was synthesized by the reduction of as received samples under a H_2/N_2 flow. Temperature-programmed reduction (TPR) measurements were done to determine optimal reduction conditions. Figure 3.2A presents TPR quantified by mass spectrometry measurements at room temperature of the as-synthesized samples in the presence of H_2 mix gas. The plateau that can be seen is the normal flow of H_2 and the local minima for both Pd/Al_2O_3 and Pd/SnO_2 indicate the reduction of Pd(II) to Pd(0). Pd/CoO_x is not reduced until higher temperatures, as can be seen from Figure 3.2B in which the broad feature around 90 ºC indicates consumption of H_2 from the flow. Continued TPR profiles of Pd/MO, presented in Figure 3.2C/D, indicate the reduction of the supports at 500 ºC and 150 ºC for SnO_2 and Co_3O_4, which is consistent with the literature.[112, 113] H_2 desorption occurs from the Pd catalyst around 70 ºC and other surface adsorbed oxygen species are reduced from the SnO_2 slightly below 300 ºC as indicated in Figure 3.2D as α and β.[100] To ensure these adsorbed species did not migrate on to the Pd catalyst they were also removed before the Pd/MO standard was defined, therefore, the system was heated to 300 ºC under a H_2/N_2 mix

environment to reduce the catalyst, remove or reduce surface oxide species and define a Pd/MO standard. Note at this treatment temperature, it is expected that the Co supports will be partially reduced, thereby they are termed CoO_x.

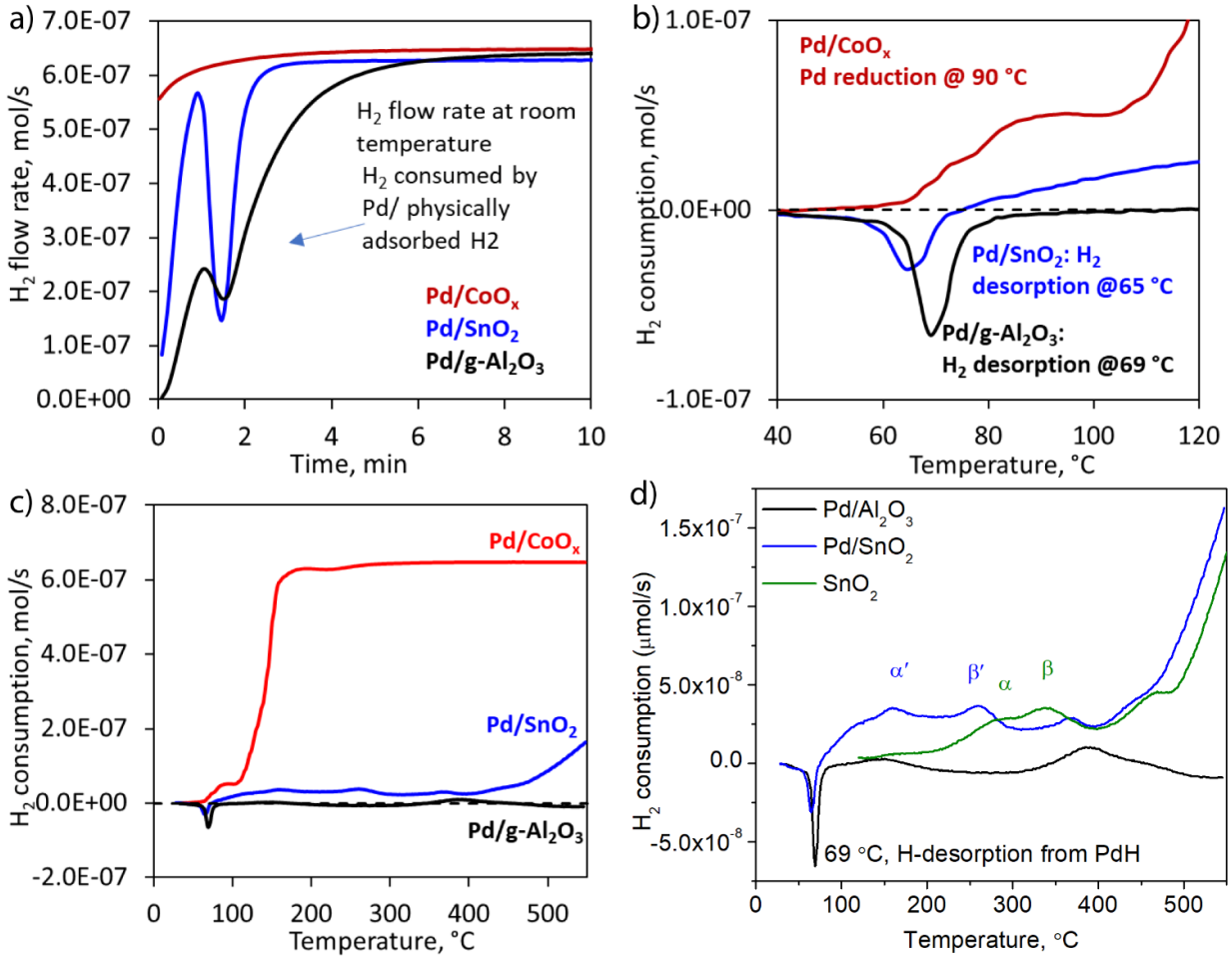

Figure 3.2. Reduction as a function of temperature in a) TPR-MS indicating PdO-Pd reduction of PdO/SnO_2 and $Pd/g\text{-}Al_2O_3$ b) TPR-MS indicating PdO-Pd reduction of Pd/CoO_x and H_2 desorption from Pd/SnO_2 and $Pd/g\text{-}Al_2O_3$ c) TPR-MS indicating reduction of Co species in Pd/CoO_x at 150 °C d) TPR-MS indicating reduction of Sn species in Pd/SnO_2 at 500 °C. Also indicating H_2 desorption from Pd/SnO_2 up to 300 °C

Figure 3.3 presents XPS characterization of the Pd(II) standards, which is a sample of Pd/SnO_2 (representative of all Pd/MO in this study) and Pearlman's Catalyst. Due to the aforementioned

synthetic process the Pd/MO after synthesis is primarily PdO, as represented in Figure 3.3, which is in agreement with the literature.[114] Figure 3.3A presents the XPS fitting of Pd/SnO_2 before the experiment with percent concentrations: Pd (~335.3 eV) 5.5 %, PdO (~336.3 eV) 88.8 % and $Pd(OH)_2$ (~337.5 eV) 5.7 %. PdO is vulnerable to X-ray photoreduction, which is the likely source of the Pd present.[99] While the deconvolution of Pd 3d into three peaks is common, the naming of the highest binding energy peak is controversial. Using Pearlman's Catalyst ($Pd(OH)_2$/Carbon) as a standard, we defined this peak as $Pd(OH)_2$, as can be seen in Figure 3.3B. Due to the majority of the sample being PdO, as-synthesized samples (before reduction) are used as the PdO standard. Pearlman's catalyst has been well characterized by Albers *et al.,* this standard was used as the $Pd(OH)_2$ standard for LCF.[49] The complexity of the $Pd(OH)_2$ species is noted and thoroughly discussed in Chapter 1. Notably, XRD was also performed on the samples, however, at such low metal concentrations and small particle sizes it was difficult to resolve separate peaks for the Pd species from background noise.

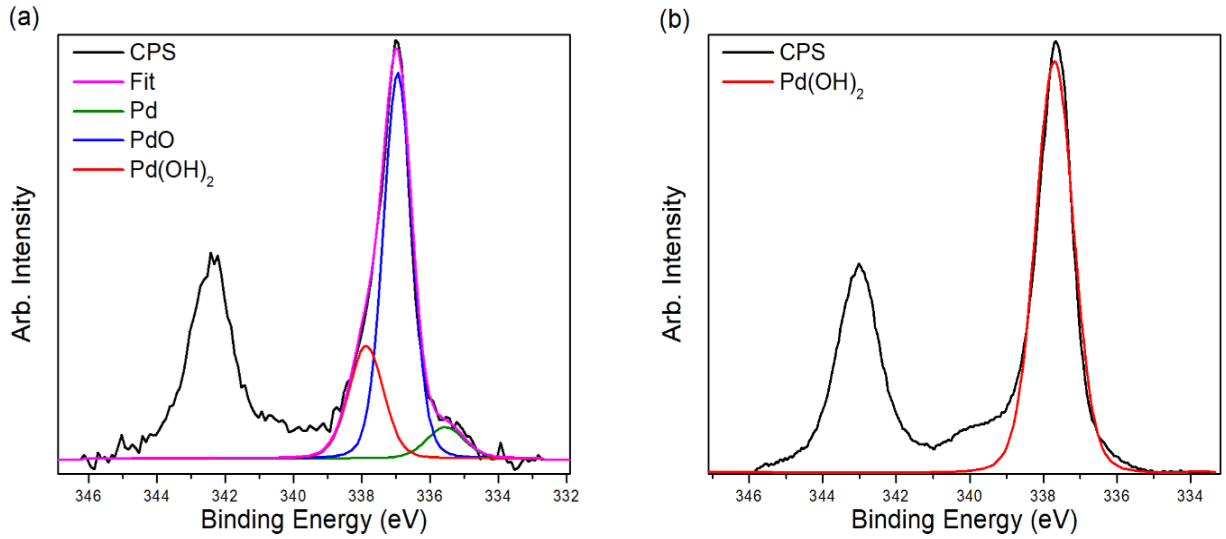

Figure 3.3. a) XPS of PdO/SnO_2 as synthesized, b) $Pd(OH)_2$/Carbon Pearlman's Catalyst.

3.3.1.2 *In Situ* Speciation of Pd by X-ray Absorption Spectroscopy

Pd K edge data, complemented with Pd L edge data was used to quantify the relative speciation of Pd(0), PdO, and $Pd(OH)_2$ as a function of temperature in methane oxidation conditions. The Pd K edge probes the 1s to 5p transition, and, therefore, is sensitive to speciation and relatively insensitive to species interacting with the surface (primarily 4d interactions). Note that the XANES region is not significantly temperature sensitive, which allows for linear combination fitting of the data over multiple temperatures. Due to the dynamic environment the Pd is present as multiple species; thus, the XANES spectrum is an amalgam of all the present Pd species in the sample. Due to conformational and oxidation state differences between the species we were able to distinguish between species via the XANES portion of the XAS data. *In situ* Pd K edge data in wet conditions is shown in Figure 3.4, along with the reference spectra used for LCF. Figure 3.4A shows changes

to the Pd/SnO_2 spectra as a function of temperature and the inset presents the XANES region. Two trends are obvious, as shown by the vertical and horizontal arrows. The horizontal arrows indicate the white line is shifting to higher energy, while the vertical arrows show the growth in the feature at *ca.* 24360 eV and loss of the feature at *ca.* 24380 eV. These changes are consistent with Pd oxidation as can be seen by comparing with Pd(0), PdO and $Pd(OH)_2$ reference spectra in Figure 3.4D. There are no major changes in spectra at low temperatures (100 ºC – 200 ºC), followed by slow oxidation at moderate temperatures (200 ºC – 350 ºC) and nearly complete oxidation at higher temperatures (400 ºC – 450 ºC). The spectra of the Pd/SnO_2 sample heated at 450 ºC under methane oxidation conditions closely resembles the spectra of the PdO standard.

In Figure 3.4B the Pd K edge of Pd/CoO_x is presented. Interestingly, there are few changes to the Pd XAS spectra as a function of temperature. This means that Pd is much more stable to oxidation on the CoO_x support, and only slight changes in Pd speciation are seen (which will be discussed in more detail below). Finally, the Pd/Al_2O_3 data is presented in Figure 3.4C. This data was previously obtained by our group under similar conditions and shows a similar trend as the Pd/SnO_2 sample which is consistent with Pd oxidation at higher temperatures.[54] The spectra seem primarily to be a convolution of Pd and $Pd(OH)_2$ at low temperatures and at high temperatures a combination of $Pd(OH)_2$ and PdO, as evidenced from a comparison of the Pd standards in Figure 3.4D.

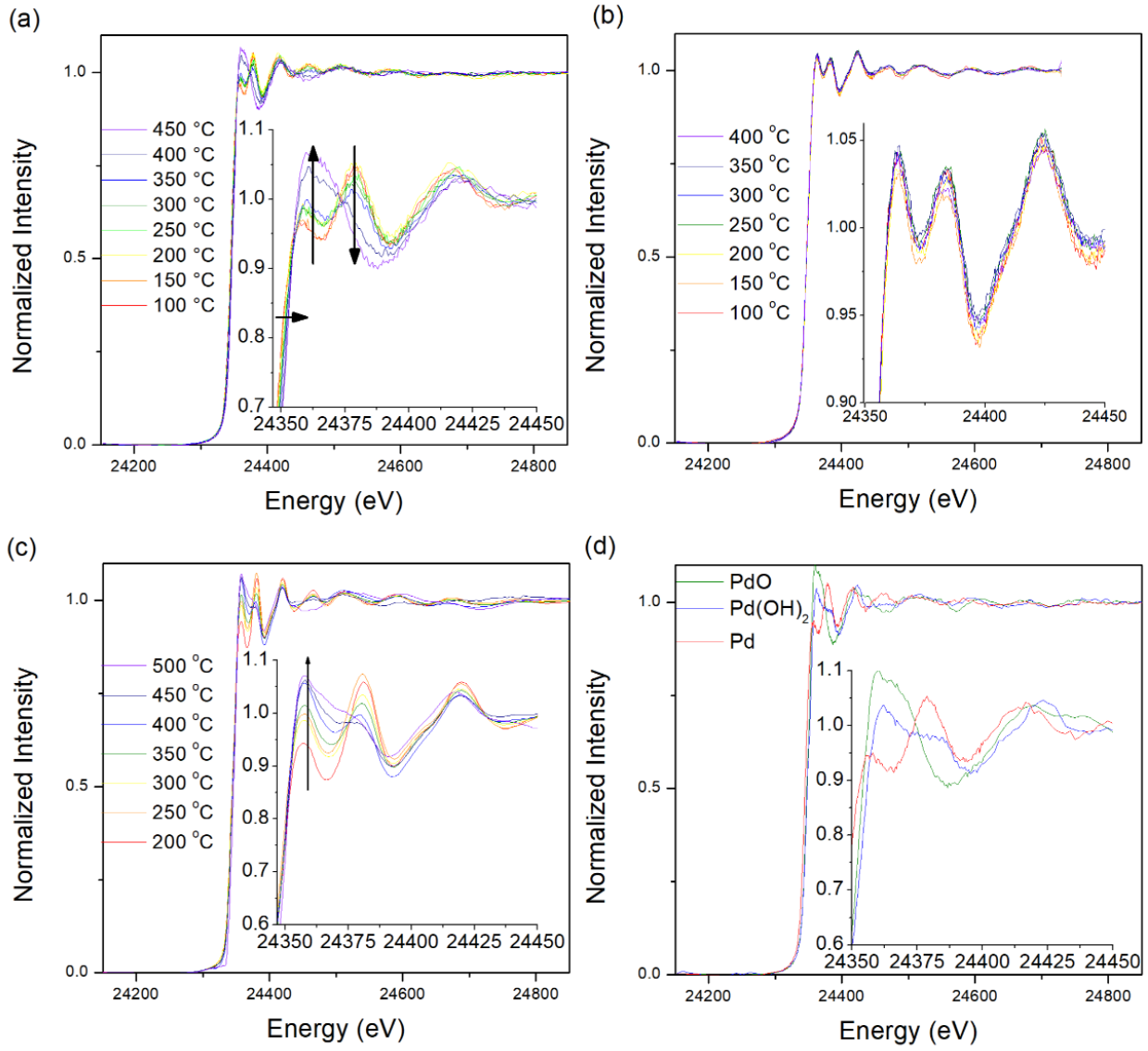

Figure 3.4. Pd K edge XAS spectra of a) Pd/SnO_2, b) Pd/CoO c) Pd/Al_2O_3 all under *in situ* wet methane oxidation conditions, and d) Pd standards.

Figure 3.5 shows the Pd L_3 edge data for Pd on SnO_2, CoO_x, and Al_2O_3 supports. The white line at the L_3 edge of Pd probes the $2p^{3/2}$ to 4d transition, and thus the occupancy of the valence 4d band of Pd, and therefore is sensitive to both Pd speciation, and to intermediates interacting with the Pd surface.[115, 116] An examination of the Pd/SnO_2 data in Figure 3.5A shows that from 100 ºC to 200 ºC, the original white line broadens slightly and the peak maxima is relatively static. At moderate temperatures, the spectra shifts to slightly higher energies (a 1.5 eV blue shift) with a slight increase in the white line intensity. Finally, beyond 350 ºC the white line shifts slightly to lower energy (a 0.5 eV red shift) and increases slightly in intensity. On comparison with Pd standards in Figure 3.5D, this suggests mild oxidation of the samples at higher temperature, until 400 ºC at which point minor reduction occurs, which is consistent with K edge data, although the Pd L_3 edge data suggests a much lesser degree of Pd oxidation. One possible rationale for the differences seen in the Pd L_3 and K edge data for Pd/SnO_2 samples is that for lower energy L_3 edge studies, the gaseous environment needed to be switched to He during measurements to prevent X-ray scattering of the gaseous atmosphere, whereas for K edge measurements, this change in atmosphere was not necessary. It is possible that some Pd photoreduction may occur while under the He atmosphere, although this has not been directly observed in this experiment.

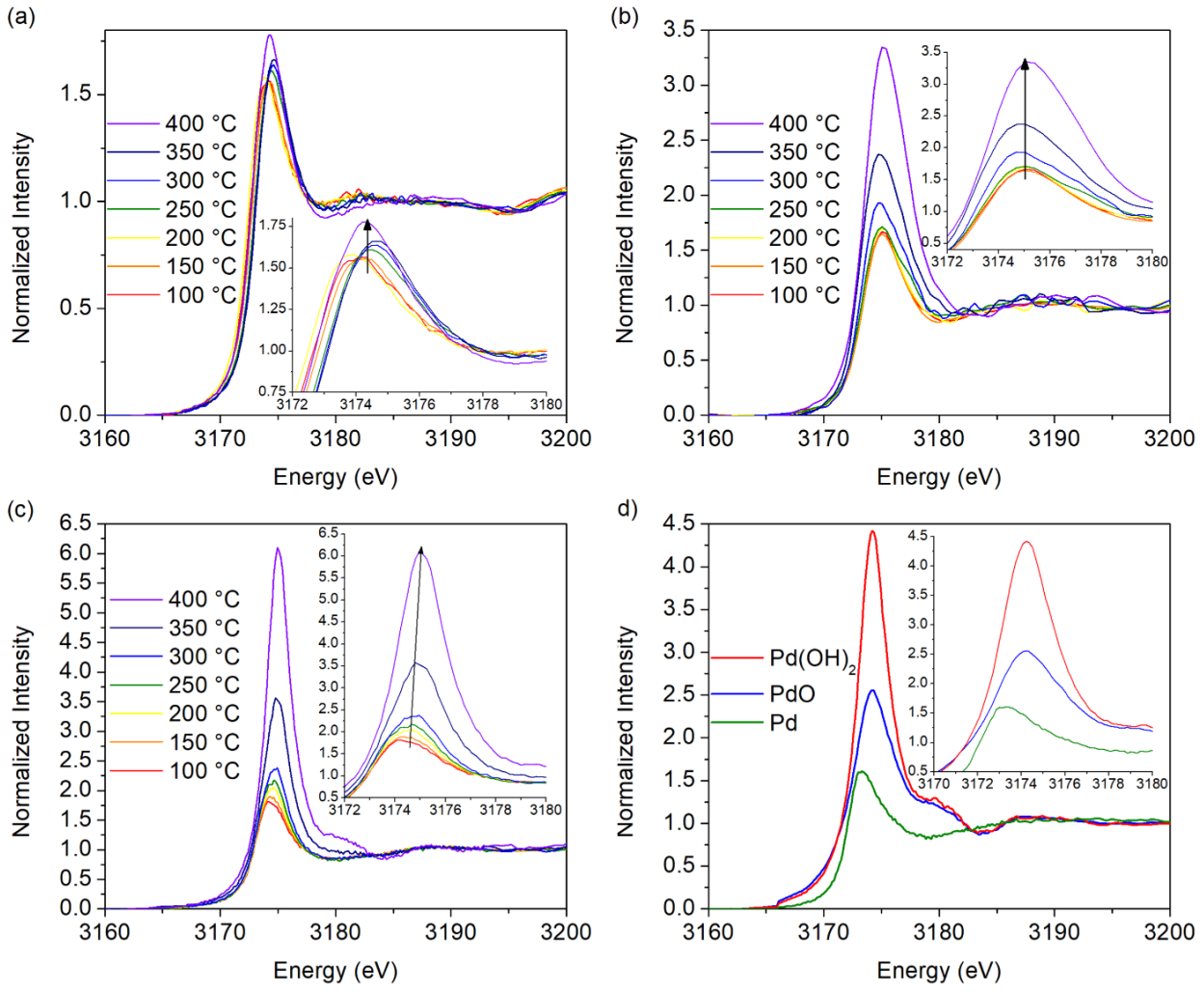

Figure 3.5. Pd L_3 edge of a) Pd/SnO_2, b) Pd/CoO_x, c) Pd/Alumina and d) Pd standards.

Figure 3.5B shows the *in situ* Pd/CoO_x data. The sample has poorer/signal noise than the other two systems due to significant scattering, likely from the support. However, this should not significantly impact data interpretation which focuses on the white line. Pd/CoO_x shows little change in the Pd L_3 edge until 300 °C, beyond which significant increases in the white line intensity are seen. Compared to the Pd K edge data for this system, at first glance this suggests a much

greater amount of oxidation for the Pd in this system at the L edge. However, the increase is essentially vertical, which may indicate that the presence of electron-withdrawing species (EWS), and not oxidation state changes, may be causing the intensity increase. This is particularly obvious as compared to the Pd/Al_2O_3 data discussed below, which shows both increases in L-edge intensity and a significant shift in the edge at higher temperatures.

Figure 3.5C presents the *in situ* Pd/Al_2O_3 L_3 edge data. As the temperature increases, the white line drifts right, ultimately by 1 eV, indicative of an oxidation state change and increases in intensity. Overall, the Pd L_3 edge data is in good agreement with the Pd K edge data for this system. The intensity of the spectrum in the Pd/Al_2O_3 is above the $Pd(OH)_2$ standard, suggesting that an EWS is also present that is more electronegative than the hydroxide. The EWS may be formate, a long living intermediate of the methane oxidation pathway.[117] The presence of this feature in the Al_2O_3 and CoO_x catalysts and not in the SnO_2 catalyst may be indicative of a longer lifetime of the formate in Pd/Al_2O_3 and Pd/CoO_x systems, however, further work would be necessary to confirm this.

The Pd L_3 standards, presented in Figure 3.5D, have a peak maxima shift from Pd(0) to Pd(II) of 1 eV. These samples were synthesized as discussed previously with the K edge, however, were not collected under *in situ* conditions. As such, given that EWS are likely affecting the white line intensities in the Pd L_3 edge data, we did not attempt to fit these spectra using LCF. In order to fit L_3 edge data, stringent control of the surface species via controlled gas environments would be required (*i.e*. Pd species in the presence of formate, *etc*.), to create a library of spectra showing Pd-EWS interactions. Since at least three variables are manipulating the peak shape (oxidation state, photoreduction and EWS presence) the data is significantly more complex to deconvolute than the K edge data.

3.3.1.3 Linear Combination Fitting – Palladium

Figure 3.6 presents the LCF fitting of the Pd K edge for the Pd/SnO_2, Pd/CoO_x and Pd/Al_2O_3 samples. These fittings quantify the anecdotal discussion above. Data used for the Pd/Al_2O_3 system is from our previous study, which used similar catalysts studied under similar reaction conditions.[53] We note that LCF was not done with Pd L_3 edge data, given the possibility that surface speciation and/or photoreduction changes may be influencing the spectra at the Pd L_3 edge. The Pd/SnO_2 data in Figure 3.6A shows that Pd metal slowly oxidizes with the formation of both PdO as a dominant oxidation product and $Pd(OH)_2$ as a minor product. At higher temperatures beyond 400 °C, complete dehydration of $Pd(OH)_2$ is seen. The maximum observed $Pd(OH)_2$ fraction on Pd/SnO_2 of 15 % at 400 °C matches the Pd dispersion of the catalyst.

The Pd/CoO_x LCF results, as seen in Figure 3.6B, show a different pattern in which a relatively stable Pd(0) to Pd(II) ratio is apparent, with a significant proportion of Pd present throughout the temperature range. The $Pd(OH)_2$ maximum abundance of 20 % resembles the dispersion, calculated by chemisorption of 17.5 %, variances may be due to both the technique differences and the environmental stresses on the system. Figure 3.6C shows the Pd/Al_2O_3 LCF results. As the temperature increases from 200 °C in the presence of water the fraction of metallic Pd on Pd/Al_2O_3 decreases in favor of $Pd(OH)_2$ formation. The dehydration of the $Pd(OH)_2$ forming PdO is seen at 450 °C. Notably, this sample is the only sample in which the $Pd(OH)_2$ concentration increased above the Pd dispersion data. Up to 350 °C the system seems to have a limit of $Pd(OH)_2$ which is the same as dispersion data. However, after 350 °C an activation barrier seems to be crossed allowing hydration of PdO within the particle. Although each Pd system has been synthesized similarly, the support dramatically alters the calculated speciation of oxidized Pd species in these

systems. All these systems have corroborating anecdotal information provided by the L_3 edge, as discussed above.

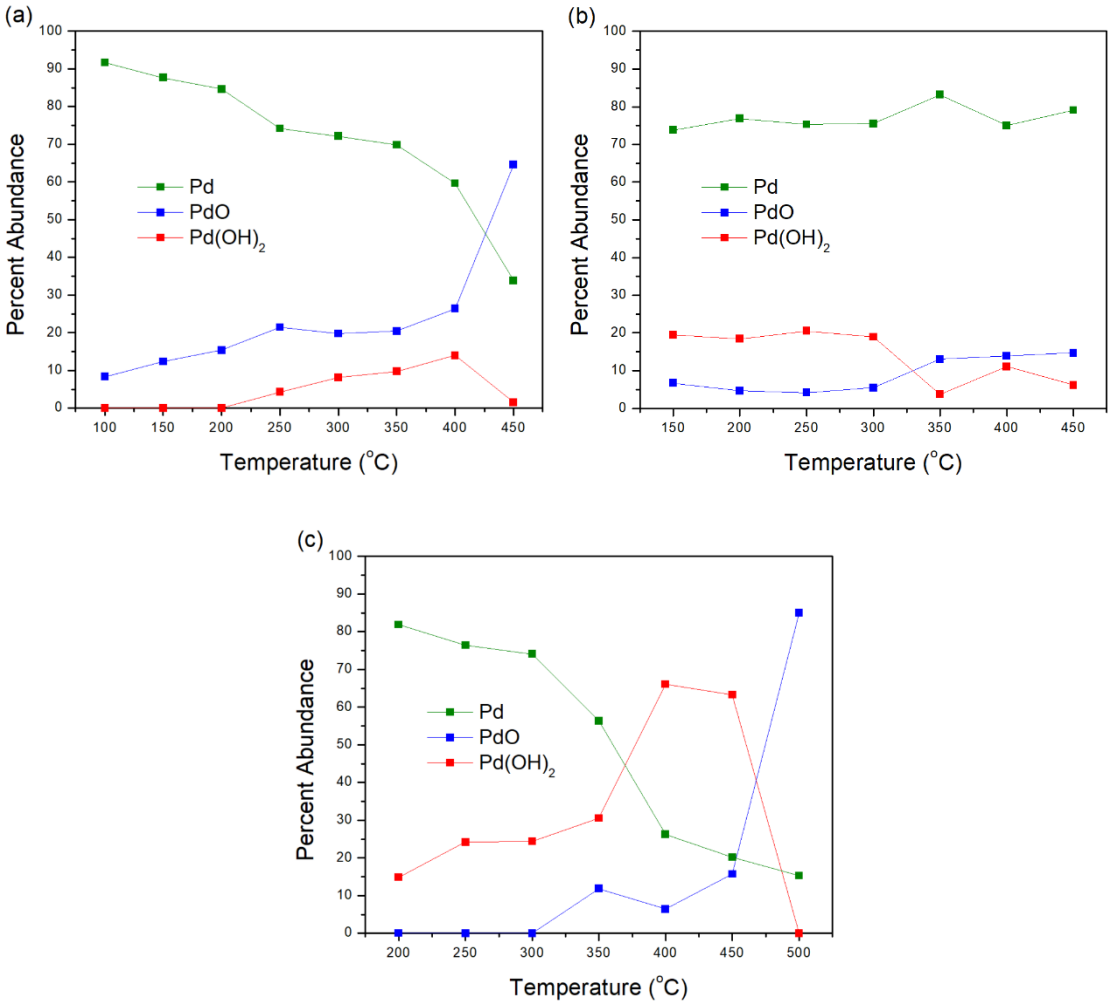

Figure 3.6. *In situ* Pd/MO LCF of Pd K-edge spectra for a) Pd/SnO_2, b) Pd/CoO_x, and c) Pd/Al_2O_3.

3.3.2 Speciation of the Metal Oxide

Sn L_3 edge XAS data is presented in Figure 3.7A. Due to the larger particle size of the SnO_2 support, the fitting of this species is significantly easier, however, is less sensitive to surface interactions. This is because the surface, typically the most active and complex part of a system,

is not a substantial percentage of the SnO_2 particles. Commercial SnO and SnO_2 were used as standards and the overlay and LCF indicate a reduction from SnO_2 to SnO between 100 ºC and 250 ºC at which point the system is relatively stable. The *in situ* analysis of Sn L_3-edge demonstrated approximately 10 % SnO at 100 ºC, which was likely induced by the catalyst pre-treatment, which increased to 30 % at 250 ºC and stabilized up to 400 ºC. The reduction of Sn(IV) could occur by electrons liberated during SnO_2 hydroxylation. This occurs as: $H_2O + Sn_{lattice} + O_{lattice} \rightleftharpoons (HO\text{-}Sn_{lattice}) + (O_{lattice}H)^+ + e^-$ and is a possible mechanism for the reduction process.[100]

Figure 3.7B presents the *in situ* XAS data at the Co K-edge for the Pd/CoO_x catalyst. Two phases are seen, firstly reduction from 100 ºC to 200 ºC indicated by a small arrow pointing to the top left of the inset. Following this, oxidation is seen from 250 ºC until 400 ºC, indicated by the long arrow pointing to the bottom right of the image. The LCF fitting is shown in Figure 3.7D using the Co(0), Co(II) and Co(III) standards. The LCF results show the appearance of a Co(III) species, starting at 300 ºC, which shows that the Co is being further oxidized during the reaction. The presence of a large amount of metallic Co at the beginning of the reaction suggests that this support, in particular, is significantly reduced in the presence of Pd when exposed to the H_2/N_2 gas used to reduce Pd.

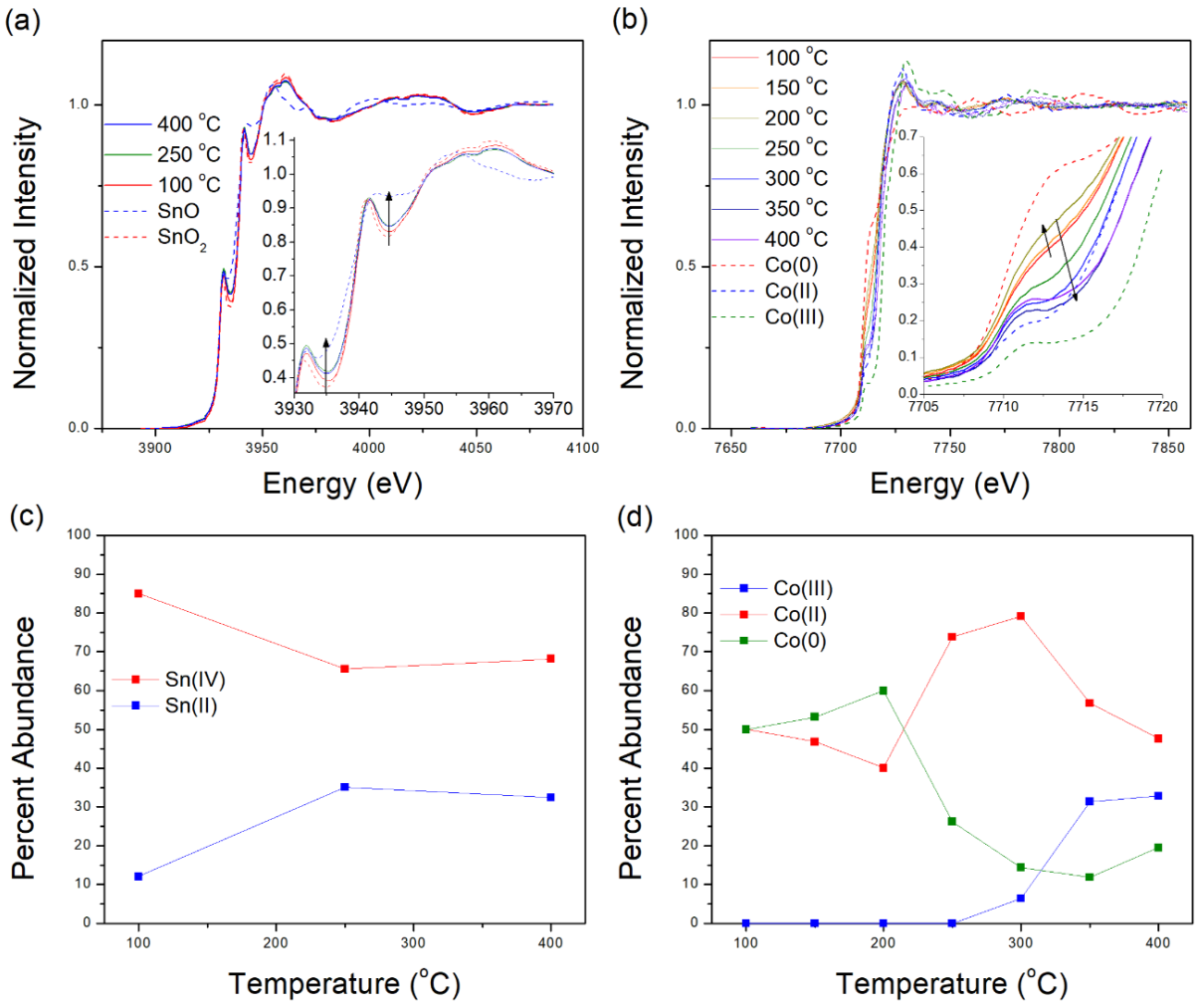

Figure 3.7. a) L_3 edge of Sn for Pd/SnO_2 b) K edge of Co for Pd/CoO_x c) LCF of SnO_2 and d) LCF of CoO_x.

3.3.3 Speciation and its Relationship to Catalytic Activity

As discussed in the introduction, $Pd(OH)_2$ is not an active catalytic species and can form passivating layers on supported Pd nanoparticles. This restricts catalytic activity until methane is able to access active sites which are blocked by the hydration of PdO.[48] Therefore, it is anticipated that $Pd(OH)_2$ dehydration and catalytic activity onset are correlated. Figure 3.8 presents methane conversion as a function of temperature for the Pd/MO species investigated in this chapter.

Recognize all species show catalytic activation curves with similar shapes, in which catalytic activity begins and within a 150 ºC temperature increase the methane conversion becomes nearly 100 %.

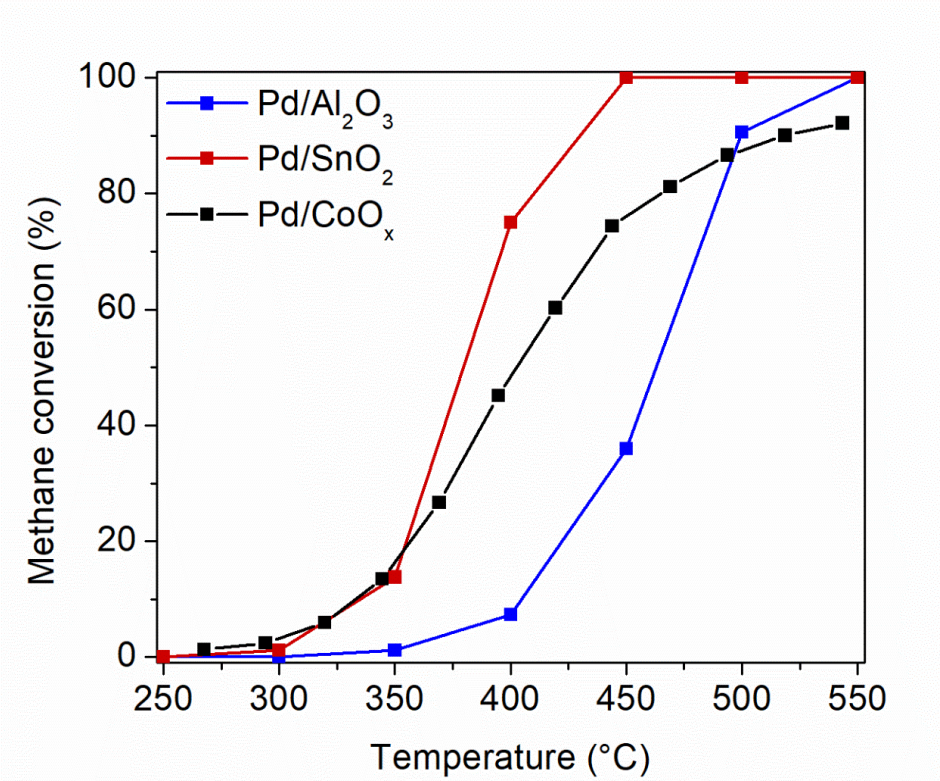

Figure 3.8. Ignition curves of the studied Pd catalysts performed by Dr. Natalia Semagina's group

The LCF results of K edge data succinctly depict a relationship in which $Pd(OH)_2$ concentration decreases at the same time that methane oxidation activity increases, however, nuances between each sample are apparent. Following is a comparison of the LCF results, in Figure 3.6, and catalytic activity, in Figure 3.8, for each Pd/MO sample:

- Pd/SnO_2 catalytic activity is seen starting at 300 ºC and is not at 100 % methane conversion until 450 ºC. LCF of the Pd/SnO_2 depicts $Pd(OH)_2$ at lower concentrations than the

dispersion of the Pd particles until 400 ºC at which point it rapidly declines to 1.5 % at 450 ºC. This occurs at the same time there is a dramatic increase in PdO concentration, and at the same time that the Pd/SnO_2 reaches 100 % methane conversion.

- For Pd/CoO_x, $Pd(OH)_2$ concentration has a slightly different relationship. Catalytic activity begins at 300 ºC at which point a corresponding equilibrium shift is seen in the LCF data, a decrease in $Pd(OH)_2$ concentration and an increase in PdO concentration. Throughout, a much higher level of Pd(0) exists in this system. The system does not reach 0 % $Pd(OH)_2$ and does not reach 100 % methane oxidation.
- Pd/Al_2O_3 catalytic activity starts at 350 ºC and climbs, initially very slowly but significantly more rapidly after 400 ºC to over 90 % methane conversion by 500 ºC. At 500 ºC no $Pd(OH)_2$ is seen and a rapid increase in PdO concentration is seen between 450 ºC and 500 ºC.

As described above, $Pd(OH)_2$ concentration changes and catalytic activity increases consistently occur at similar temperatures. The presence of some $Pd(OH)_2$ during regions of catalytic activity is explainable due to time resolution of the experiment; since the measurement occurs on the order of minutes a time average of the system may show $Pd(OH)_2$ concentrations adequately high to cover the surface, even though a PdO ⇌ $Pd(OH)_2$ equilibrium exists. If this is true, the $Pd(OH)_2$ would have to have a longer lifetime than the PdO, to show high concentrations of $Pd(OH)_2$ even though PdO is present on the surface. In the Al_2O_3 and SnO_2 systems, at close to 100 % methane conversion there is little to no $Pd(OH)_2$ present. In the CoO_x system, where persistent $Pd(OH)_2$ exists up to 450 ºC, catalytic activity does not reach 100 % methane conversion. This is suggestive that the methane and water are competing for the active sites of the

PdO. In the Al_2O_3 and SnO_2 systems the water is outcompeted, however, in the CoO_x systems, the water is continually competing for PdO on the surface.

Comparing Figure 3.7 and Figure 3.8 also gives us some information. As stated previously, due to the large size of the metal oxide supports, their surface area is a small proportion of the measured material. Therefore, the experiment is less sensitive to the surface area, a region which is likely extremely active during catalytic activity. This experiment will instead present speciation of the bulk metal oxide, which may be indicative of some surface activity.

For Pd/SnO_2 the SnO_2 reduces to SnO from 100 °C to 250 °C. This is significantly lower in temperature than the anticipated reduction of SnO_2 to SnO in similar conditions according to DFT and TPR studies, which are predicted to occur between 400 °C and 500 °C.[118] Figure 3.6 shows that in the same temperature region, 100 °C to 250 °C, the Pd is oxidized to PdO. As water then interacts with PdO, $Pd(OH)_2$ is synthesized. The presence of SnO may mitigate the $Pd(OH)_2$ buildup by forming $Sn(OH)_2$, which is supported by both thermodynamic considerations and experimental measurements.[100]

Dehydration of $Pd(OH)_2$ on CoO_x starts at 300 °C. From 300 °C to 350 °C the Co(II) concentration drops from 80 % to 56 %. Simultaneously, the Co(III) concentration increases from 6 % to 32 % and the Co(0) concentration drops from 14 % to 11 %. Overall, the CoO is therefore being preferentially oxidized, while keeping much of the Pd in a zerovalent state at much higher temperatures. Simultaneously, the $Pd(OH)_2$, as seen in Figure 3.6 is being dehydrated. This corroboration may be an indication that the CoO_x is being oxidized by the Pd, via the donation of activated oxygen to the CoO_x. The slight decrease in $Pd(OH)_2$ may be due to hydroxyl migration to the newly oxidized Co surface.

Al_2O_3 is a support generally regarded as extremely stable in these temperature regions and conditions. Therefore, the Pd speciation for Pd/Al_2O_3 is assumed to be manipulated only by the environment in these temperature regions. Pd oxidation is dominated in Figure 3.6 by $Pd(OH)_2$ formation, and after 450 ^oC a 63 % drop in $Pd(OH)_2$ corresponds to a 60 % increase in PdO concentration. Overall, the exotic supports, CoO_x and SnO_2, presents dramatically less $Pd(OH)_2$ than on Al_2O_3 supports at the same temperature and seemingly prevent $Pd(OH)_2$ concentrations from increasing above the dispersion of the particle.

3.3.4 On the Validity of Linear Combination Fitting

Linear combination fitting (LCF) is a statistical regression technique in which one attempts to reduce the R-factor value within a selected region by manipulating the weighting of the given fitting species, as discussed in Chapter 1. Thus, a variety of issues can dramatically alter the data set. Therefore, presented data must corroborate with other quantitative measurements in order to build confidence in the fittings created; LCF data is not intended to stand alone. A variety of work performed between the two groups satisfactorily corroborates with the LCF:

- Standardization of Allowed Species: the fitting program was fit with the same species consistently; Pd/MO-oxidized, Pd/MO-reduced and Pearlman's Catalyst ($Pd(OH)_2$ standard). These are the only anticipated Pd species in these conditions. In the interpretation of these data sets the fitting allowed for the weighting of any species from 0-100 % and it is recognized that the fitting differentiated between species, thereby showing it recognized a significant difference between the three species.
- Correlation with Surface Area Calculations: $Pd(OH)_2$ is often regarded as a surface species, created by adsorbed water in these conditions,[48] that can penetrate to the core under particular conditions.[49] Therefore, the $Pd(OH)_2$ percent abundance and Pd dispersion data

should corroborate. Pd/SnO_2 chemisorption data presents 16 % Pd dispersion and the maximum $Pd(OH)_2$ coverage is 15 % by LCF. In the case of the Pd/CoO_x the CO adsorption experiments calculated 17.5 % Pd dispersion, and the LCF calculations suggested a maximum of 20 % $Pd(OH)_2$. The Pd/Al_2O_3 chemisorption data suggests 40 % Pd dispersion, and LCF shows a plateau at 31 % until 350 °C at which point the $Pd(OH)_2$ is able to penetrate beyond the surface. These values closely reflect one another, even without accounting for dramatic temperature differences and condition differences that may be affecting the particle size and morphology.

- Correlation with Catalytic Data: The expectation is PdO is the active catalyst at these temperature ranges,[47] thereby, around the onset of catalytic activity a shift in the Pd species equilibrium is anticipated. Correlations of dramatic equilibrium shifts coinciding with catalytic activity changes are prevalent in each data set as discussed above.

Another notable detail of the LCF method is the window of the fit. The window was set to -15 eV and 40 eV from the E_0 position of the XAS data. This window is regarded as the XANES region: the region containing atom speciation. Beyond this region is the EXAFS region of XAS, which measures photoelectron scattering from neighbouring atoms. Remaining within the XANES region is paramount as the standards are only acceptable within this region. This is why much care was taken to attempt to synthesize standards on the support: Pd/MO-reduced and Pd/MO-oxidized. If a hydrating mechanism existed to synthesize PdO/MO-hydrated standards, this would be preferred, however, no definitive pathway to this product is known. Although valid the LCF values are not likely to be absolutely precise and should be viewed as semiquantitative and trends should be focused on rather than exact values. The dispersion vs $Pd(OH)_2$ concentration data may be

indicative of the error associated with these measurements, however, the precise error of the LCF data is difficult to exactly quantify as it involves modeling of an experimental result.

3.4 Conclusions

The ability to follow the Pd-PdO-$Pd(OH)_2$ equilibrium *in situ* via Linear Combination Fitting of K edge X-Ray Absorption Spectroscopy has been shown. *In situ* Pd L_3 edge data has been provided to corroborate with the Pd K edge data and fittings. Conventional characterization and catalytic correlations have been presented to support the speciation changes that were determined by linear combination fitting of *in situ* XAS data. The effect of the metal oxide, SnO_2, CoO_x and Al_2O_3, on the Pd speciation equilibrium was also compared. CoO_x and SnO_2 were seen to be inhibiting the amount $Pd(OH)_2$ formed, while CoO_x tremendously reduced Pd oxidation. Another notable difference is the penetration of the $Pd(OH)_2$ species within the particle which is possible in the Al_2O_3 supported sample but has presumably not occurred on the other species. Also, the extent and stability of Pd oxidation between all three species is dramatically different. This is suggestive of the electronic properties of the Pd are being manipulated by the support. Exploitation of the understanding of these phenomena may be used in order to create more rationally designed catalysts in the future.

Chapter 4 Conclusions and Future Work

4.1 Summary

The work provided in this thesis details the rational synthesis and design of Pd-based heterogeneous catalysts and *in situ* characterization of these catalysts by X-ray absorption spectroscopy. This work focused on the methane combustion reaction catalyzed by Pd nanoparticles supported on a variety of metal oxide supports. Chapter 2 presented and discussed a novel synthetic method, galvanic deposition, for the synthesis of highly dispersed Pd nanoparticles on SnO_2. The benefits of galvanic deposition are primarily the ease of the synthetic route, and the lack of organic stabilizers used in the synthesis. Chapter 3 explored the *in situ* speciation of the catalysts using XANES Spectroscopy and deconvoluted that data using Linear Combination Fitting, notably quantifying $Pd(OH)_2$, an elusive passivating species. Furthermore, Chapter 3 validated this technique by providing corroborating evidence to support the fits presented. Therefore, this work expands on both the synthesis and characterization of rationally designed catalysts.

4.2 Conclusions

4.2.1 Galvanic Deposition

Synthesis of supported nanoparticle materials from pre-fabricated nanoparticles has a variety of inherent challenges, primarily stemming from the requirement of organic stabilizers in the synthesis. Chapter 2 shows that galvanic deposition can be used as a novel alternative strategy which requires no organic species, reducing agent or protecting ligand, to synthesize metal

nanoparticles dispersed on metal oxide supports. Pd/SnO_2 was the case study of this chapter, however, work was presented on Pd/FeO as well. The chapter first showed that commercial SnO, when characterized by XPS, shows surface oxidation and disproportionation, presenting SnO_2 and Sn on the surface. The sample was heated at moderate temperatures under a flow of reducing gas, which reduced the surface from SnO_2 to SnO, and had the added benefit of reducing the Sn concentration as well, presumably due to the reverse of the disproportionation reaction. Following this, Pd was deposited on the SnO-reduced particles by a spontaneous galvanic reaction leading to the formation of Pd(0) on the SnO surface. The reaction was followed by UV-Vis of Pd(II) salts and the final materials were characterized by XPS and XRD. Results showed that the SnO partially oxidized to SnO_2 and the primary Pd species present was Pd(0). Chemisorption data showed large particles, with low dispersions. However, upon complete oxidation of the system in air, the speciation changed to PdO/SnO_2, with much improved dispersions. Characterization by XRD and XPS showed PdO species, and that the SnO_2 species was the dominant Sn species. Chemisorption data suggested that dramatic particle morphology changes happened during the oxidation step, presumably due to strong Metal Support Interactions inducing a wetting type effect, forming higher surface area Pd nanoparticles. The final calculated particle size by chemisorption was comparable to conventionally synthesized metal nanoparticles on metal oxides, and the benefit of reducing the SnO before galvanic deposition is seen as higher dispersity is seen for such samples.

Finally, to show generality of the concept, a brief description of the Pd/FeO system was presented. These particles were synthesized similarly, showing the generalizability of the reaction. Another key benefit of presenting this reaction was the atomic number differences between Pd and Fe allowed TEM to have some contrast between the FeO nanoparticles and the Pd nanoparticles. This allowed TEM characterization of the Pd decorated FeO nanoparticles, something unattained

with the Pd/SnO_x system due to the similarity of the atomic numbers of Pd and Sn. Thus, this project showed the promise of using galvanic deposition techniques as a method to expand the repertoire of synthetic techniques available to catalysis researchers and presents a technique which may be simpler and more accessible to industry for larger scale applications. Furthermore, the final materials have an unhindered metal to metal oxide interaction, which may have other possible advantage over synthesizing supported nanoparticles from pre-fabricated nanoparticles stabilized by organic ligands. Unfortunately, due to time constraints of an MSc, the Galvanic Deposition synthesized particles were not able to be used in the XAS and LCF work presented in Chapter 3. This leaves an open question: does galvanic deposition promote strong metal-support interactions?

4.2.2 *In Situ* Speciation of Methane Oxidation Catalysts by X-ray Absorption Spectroscopy

Pd-based methane oxidation catalysts are typically hampered by water poisoning, which can only be alleviated by operating at high temperatures. Water exposure leads to $Pd(OH)_2$ formation, which is a difficult species to characterize, as traditional IR methods cannot easily distinguish hydroxides on the PdO surface vs. those on the metal oxide support surface and also struggle to differentiate between the hydroxides in the dynamic environment of *in situ* methane oxidation. The change in coordination environment from PdO to $Pd(OH)_2$ allows the utilization of X-Ray Absorption Near Edge Structure Spectroscopy (XANES), the region near the absorption edge of an element in X-Ray Absorption Spectroscopy (XAS), to distinguish between the species. Chapter 3 is about the design, standards and use of an *in situ* cell for *in situ* speciation of Pd catalysts using XANES. The K and L_3 Pd XAS edges of Pd nanoparticles deposited on a variety of metal oxide supports was analyzed. Furthermore, the XAS edges of metal oxide supports themselves were analyzed for both the Sn and Co oxide systems.

The Pd K edge is sensitive to Pd speciation. Three species were distinguishable; Pd, PdO, and $Pd(OH)_2$. On different supports in situ Pd speciation during methane oxidation with respect to temperature was dramatically different. Pd/Al_2O_3 samples showed extensive oxidation at moderate temperatures, producing the largest amount of $Pd(OH)_2$, approximately 65 % of the Pd species at 400 ºC, and showed the most oxidation, 85 %, at 500 ºC. Meanwhile, the Pd/CoO_x system was significantly more stable, with only mild oxidation, 25 % Pd(II) species, occurring as the system was heated from 150 ºC to 450 ºC. A speciation change was measured between 300 ºC and 350 ºC as the equilibrium shift favored PdO from the dehydration of $Pd(OH)_2$, which is correlated with the onset of catalytic activity. The Pd/SnO_2 system was different for two reasons. First, from the onset of the experiment, the PdO concentration was increasing, juxtaposed to other systems in which $Pd(OH)_2$ was the primary oxidation product at low-moderate temperatures. $Pd(OH)_2$ was only seen in the Sn system at low concentrations and, like the Co system, the concentration of $Pd(OH)_2$ never surpassed the dispersion of the Pd. The Sn system did undergo extensive oxidation throughout the experiment, starting at 90 % Pd and oxidizing to 30 % Pd. The XAS data was correlated with both chemisorption, temperature programmed reduction data, and catalytic methane oxidation results.

The Pd L_3 edge is a lower energy edge that probes the $2p_{3/2}$ to 4d transitions. The 4d orbital is available for and utilized in surface interactions, therefore, surface adsorbed species can extensively affect the spectra. In the dynamic *in situ* environment this creates complex spectra to deconvolute. However, a variety of conclusions were still able to be drawn from white line position and height. First, the L_3 and K edge trends were fairly consistent, reinforcing previous work on the K edge. Second, different trends were noticed after the onset of catalytic activity. The Pd L_3 edge for Pd nanoparticles supported on alumina showed incredibly strong white line

intensity, surpassing even the intensity of the $Pd(OH)_2$ standard, suggesting that potentially other species, likely formates, also formed on the Pd nanoparticle surface during methane oxidation. For the Co oxide system, the spectra showed an increasing white line, primarily at and after 300 ºC, consistent with surface species accumulating on the Pd surface. This was not seen in the Sn oxide system, which showed only very modest changes to the Pd L_3 edge, suggesting very little $Pd(OH)_2$ and/or electron withdrawing species formed in this system.

Co and Sn metal oxide speciation were also measured at the Co K and Sn L_3 edge. The Co oxide was significantly more affected by the catalytic environment. For example, the initial system was 50 % Co(0) and 50 % Co(II). At 250 ºC the system was 26 % Co(0) and 74 % Co(II). At 400 ºC the system was 20 % Co(0), 32 % Co(III), and 48 % Co(II). The dominant oxidation state varied throughout the temperature range and showed that Co itself was oxidizing during the reaction, while Pd stayed mostly in the zerovalent state. The Sn oxide system was significantly more stable, with a slight reduction of SnO_2 seen throughout the experiment. The metal oxide supports used had particle sizes that were significantly larger than the Pd nanoparticles supported on their surfaces, and therefore measurements were less surface sensitive.

4.2.3 Significance and Implications

The principle theme of the presented work is to assist in the synthesis of rationally designed catalysts, by diversifying and furthering our understanding of these systems. While the presented work focused on methane oxidation as the catalyst system of interest, much of the work has broader consequences.

Galvanic deposition diversifies the repertoire of synthetic processes targeting heterogeneous supported nanoparticle catalysts on metal oxide systems. While galvanic reactions of metal

nanoparticles are common in the literature, galvanic reactions have yet to be utilized to design supported metal on metal oxide catalysts. Galvanic deposition fills this gap by utilizing redox potentials to directly synthesize metal nanoparticle catalysts on metal oxides, simply, with few reagents and in a presumably scalable process. By thoroughly characterizing the synthetic process of a case study system, Pd/SnO_2, the necessary information is provided to generalize galvanic deposition to a variety of different catalytic systems. Currently high quantity supported-nanoparticle heterogeneous catalysts with highly monodisperse and compositionally uniform nanoparticles are difficult to obtain in the catalysis industry. While a route to make these particles was shown in Chapter 3 starting from colloidal Pd nanoparticles stabilized by polymer stabilizers, this route is not easily scalable as it uses large amounts of solvent and organic stabilizer in the synthesis of the catalyst. In principle, the galvanic reaction is much more scalable, though more work needs to be done to control final particle sizes in this synthesis.

The understanding of Pd catalysts during methane oxidation *in situ* analysis, sensitive to all expected Pd species, is now attainable. *In situ* XAS measurements at both the Pd K and L_3 edge, have been able to show that one can reliably distinguish between PdO and $Pd(OH)_2$, and furthermore, to quantify the presence of all Pd species. This work furthers both our understanding and ability to understand the speciation of Pd, and other species, while doing *in situ* measurements in adverse environments. Chapter 3 shows that one is able to quantify the $Pd \rightleftharpoons PdO \rightleftharpoons Pd(OH)_2$ equilibrium in a variety of catalyst systems. The focus on the XANES region of XAS allows the speciation and quantification of catalyst systems in dynamic conditions with high sensitivity to species.

The rational design of catalytic systems is bolstered by this work. The synthetic and catalytic understanding of methane oxidation catalysts, and, by extension, heterogeneous catalysts has been furthered by the presented work.

4.3 Future Work

Although interesting avenues of investigation existed, time did not allow to chase all possible insights. Following is a discussion of work that may be performed in order to expand our understanding of the synthetic methods provided and to further utilize the *in situ* XAS cell at the Canadian Light Source.

4.3.1 Galvanic Deposition

The design of the galvanic deposition reaction seems to be specifically suitable for industrial purposes. A simple reaction, reduced number of reactants, reduced cleaning requirements and more, make galvanic deposition a convenient approach to industrial synthesis of supported-nanoparticle catalysts than other alternative synthetic approaches. Further simplification of this method would be beneficial. Two approaches have become evident that will need further exploration:

- Within the current synthetic technique Pd/SnO_x is calcined to PdO/SnO_2. This step is required to synthesize a product that is more comparable to catalysts designed using wetness impregnation strategies or other techniques that involve pre-synthesis of nanoparticles followed by activation. In the latter techniques, one typically needs to remove the ligand groups by calcination in order to open up surface area on the nanoparticle

surfaces and increase the activity of the catalyst. However, in galvanic deposition this calcination step is not required, as there are no organic groups to remove. An open question is how active are the final Pd/SnO_x and Pd/SnO_2 catalysts as made by galvanic reactions, compared to other techniques? In particular, is the last oxidation step necessary for Pd/SnO_x materials, or would they be useful catalysts at that stage. In some environments, it is likely that the gas mixture will oxidize the system to Pd/SnO_2. This would skip the synthetic step of calcination of the Pd/SnO_x. Notably, the *in situ* XAS technique presented in Chapter 3 would be a strong characterization technique to analyze this step.

- An even more simple approach may exist. Currently the technique involves purchasing or making SnO, reducing the surface of this SnO to remove any SnO_2 and Sn states produced via oxidation and/or disproportionation, and then to proceed with the Pd galvanic deposition. An alterative approach may exist in which SnO_2 supports are used and the surface of the support is partially reduced. Once that step is performed, the galvanic deposition step can be executed. Based on Chapter 2 evidence the step will then produce Pd/SnO_2, and not require calcination at all, as the galvanic reaction and/or oxygen will oxidize any surface SnO. As can be seen in Chapter 2 by XRD, the bulk SnO/SnO_2 ratio is relatively consistent throughout the synthetic process, suggesting that it is not a part of the catalytic reaction and therefore, using surface reduction may be sufficient to synthesize the desired catalysts.

As evidenced by the chemisorption and UV-Vis spectroscopy data presented in Chapter 2, varying concentrations of Pd in solution produce variable loadings of Pd on the SnO support. This is likely due to competition between oxidation of SnO by oxygen and oxidation of SnO by Pd(II); as the SnO oxidizes in solution the amount of Pd(II) ions available for interaction seems to

correlate with the final loading of the SnO: higher Pd(II) concentrations in solution produce higher Pd loadings on the SnO. It therefore seems that, if the Pd concentration is varied, varied loading of the SnO will be produced. With careful work, this could be calibrated in order to produce targeted loadings.

Characterization of the Pd/SnO_x species by electron microscopy techniques would also be beneficial. This technique would give information about particle morphology, specifically interesting would be that of the Pd morphology during the Pd/SnO_x phase. This information could be confirmed using electron microscopy, specifically, energy dispersive X-ray spectroscopy (EDX) and electron energy loss spectroscopy (EELS) mapping. Both EDX and EELS allow for elemental mapping, while EELS allows atom speciation, and has been used in similar systems.[32] Enhanced TEM techniques that allow elemental mapping are required due to the similar atomic numbers of $_{50}$Sn and $_{46}$Pd which means the contrast between Sn and Pd is too low to differentiate using typical electron microscopy techniques.

Elemental mapping was attempted during this project, however, obstacles arose in getting good images for the Pd/SnO_x system. Synthesizing SnO was an early goal of this project, in order to create SnO nanoparticles that could then be decorated with Pd. Solvothermal synthesis of SnO utilized Sn (II) oxalate dissolved in degassed ethylenediamine and reacted at 100 °C in an autoclave for 24 h, following a procedure reported by Han *et al.*.[119] Difficulties in making pure SnO via this synthesis made the project not feasible to continue, however, preliminary elemental speciation by electron microscopy was performed. EDX, was able to provide some data, as shown in Figure 4. HAADF, high angle annular dark-field imaging, is a TEM technique focused on measuring incoherently scattered electrons, and thereby produces high Z contrast. This technique was used for the initial image in Figure 4. The other three images are produced via EDX and show

the Pd and Sn X-ray fluorescence signals, and a computer generated overlay of Pd and Sn. These images show a high Pd distribution and small size of Pd particles on the SnO.

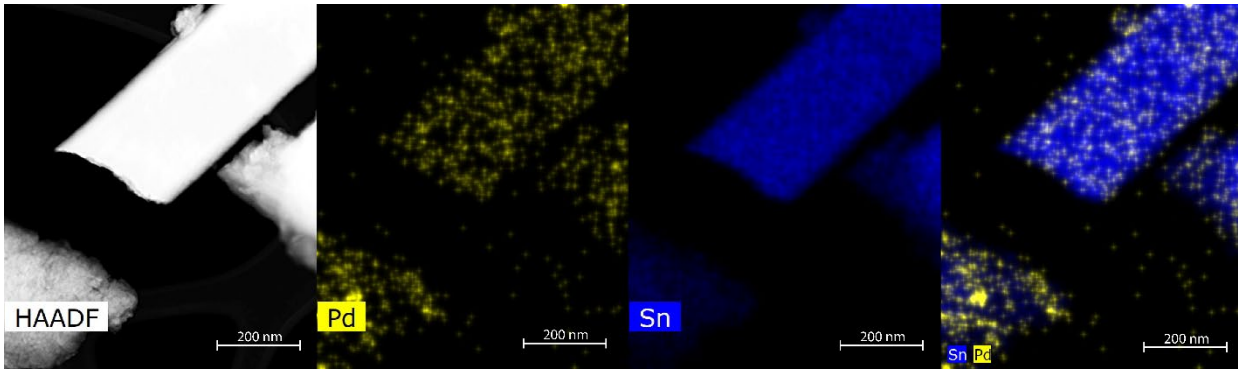

Figure 4.1. HAADF and Energy-Dispersive X-Ray Spectroscopy of Pd/SnO_x using synthesized, nanoparticle SnO.

Figure 4.1. HAADF and Energy-Dispersive X-Ray Spectroscopy of Pd/SnO_x using synthesized, nanoparticle SnO.

Oxygen X-ray fluorescence maps were also measured, and the relative Sn to O signals provided a relative value of the Sn/O ratio in one location compared to another. The expectation is that in a region with high Pd content, high O content would be correlated, indicative of the galvanic method. Oxygen contents two to three times higher in high Pd concentration areas was seen in some areas, indicative of formation of SnO_2 in areas of Pd deposition. However, this correlation was not consistently seen throughout the sample. This inconsistency was not thoroughly investigated, however, is likely due to surface oxidation on some areas of the sample. Further work is recommended in this area as the information would allow further support for characterization of the galvanic deposition products.

In the future, for EELS data, it is recommended to use the synthesis protocols shown in Chapter 2 with high surface area SnO supports. If the intent is to synthesize SnO nanoparticles, a different synthetic method would be recommended, as the carbon species are difficult to remove after the solvothermal synthesis without further oxidizing the SnO nanoparticles.

Lastly, more work should be performed with different metal on metal oxides to show the generalizability of the galvanic deposition protocol. Early work was shown for Pd/FeO, however, other metal on metal oxides are possible. Au nanoparticles are pervasive in literature and the Au(I) → Au(0) half cell potential is 1.692 V, significantly greater than that of Pd. Au(I) bromides including $AuBr_2^-$ and $AuBr_4^-$ have high potentials of 0.959 and 0.854 V respectively.[88] This suggests that synthesis of Au on metal oxides, including SnO_2 via galvanic deposition should be accessible. Furthermore, Rh is a prominent catalyst in organic reactions, has also been used in applications for catalytic converters, like Pd. Its half cell potential for Rh(I) and Rh (III) are 0.600 V and 0.758 V, suggestive that this metal could be used in the reaction as well.[120, 121] Mixtures of metals could potentially be used to attempt to make bimetallic systems as well.

4.3.2 *In Situ* Speciation of Methane Oxidation

Two Pd XAS edges were interrogated under *in situ* conditions in this thesis, the Pd K and L_3 edge. As discussed in Chapter 1 and Chapter 3, different edges are measured at different energies, and involve different atomic transitions at the edge, and thus can give complementary information about the system. The K edge of Pd is almost only sensitive to the speciation of Pd and therefore assisted in the *in situ* speciation of Pd. The L_3 edge had the added complication of also being sensitive to adsorbed surface species that interact with the Pd 4d band, as discussed in Chapter 3. While this may make quantitative speciation from the L_3 edge difficult, interesting information can be gleaned from the L_3 edge. Surface species will be representative of a variety of interesting species including catalytic intermediates and catalyst poisons. A full understanding of the Pd L_3 edge spectra would require diligent standards to be synthesized. Although the standards would be a key difficulty in the work the yielded information would be extraordinary.

The speciation of the metal oxide support was also investigated *in situ*. The metal oxides used were purchased and therefore we had very little choice as to the particle size and surface area of the support, particularly for CoO_x and SnO_x species. This is problematic as the support contains large particle sizes, and thus much of the XAS signal for the support materials is a measure of the bulk support rather than what is happening at the surface. Thus, the exact interaction between metal nanoparticles and the metal oxide support is not easily determined from our work. However, synthesis of metal oxide nanoparticle supports for the Pd nanoparticles would allow better measurements and understanding of the interaction between the metal and its surrounding metal oxide. The heterogeneous supported nanoparticle system could then be synthesized using the galvanic deposition method discussed previously. Upon doing so both metal nanoparticles on metal oxide nanoparticles and just metal oxide nanoparticles could be analyzed in the *in situ* environment and compared. The effect of the metal and the catalytic reaction on the metal oxide speciation could then be measured. With a thorough understanding of the metal oxide surface speciation, the effect of the support on the metal could then be rationalized. This would assist in the understanding of what exactly was involved in support-metal nanoparticle interactions, and particularly if there was migration of species between the metal nanoparticle catalysts and metal oxide support. In addition, one might be able to understand the mechanism of the methane oxidation reaction and whether it involves spillover of species from the support to the catalysts, or reaction sites at the boundary of the metal nanoparticle and metal oxide support.

Chapter 5 References

1. Dept. of Energy, International Energy Outlook 2016. *US EIA* **2016**.

2. Pegov, S. A., Methane in the Atmosphere. In *Encyclopedia of Ecology*, Jørgensen, S. E.; Fath, B. D., Eds. Academic Press: Oxford, **2008**; pp 2325-2328.

3. Canada, C. E. Canada's Energy Future 2019. (accessed 16 February 2020).

4. US EIA, Annual Energy Outlook 2019. **2019**.

5. Hayes, R. E., Catalytic solutions for fugitive methane emissions in the oil and gas sector. *Chem. Eng. Sci.* **2004,** *59* (19), 4073-4080.

6. Lashof, D. A.; Ahuja, D. R., Relative contributions of greenhouse gas emissions to global warming. *Nature* **1990,** *344* (6266), 529-531.

7. Forzatti, P.; Groppi, G., Catalytic combustion for the production of energy. *Catal. Today* **1999,** *54* (1), 165-180.

8. Marchetti, L.; Forni, L., Catalytic combustion of methane over perovskites. *Appl. Catal. B* **1998,** *15* (3), 179-187.

9. Gélin, P.; Primet, M., Complete oxidation of methane at low temperature over noble metal based catalysts: a review. *Appl. Catal. B* **2002,** *39* (1), 1-37.

10. Baldwin, T. R.; Burch, R., Catalytic combustion of methane over supported palladium catalysts: I. Alumina supported catalysts. *Appl. Catal.* **1990,** *66* (1), 337-358.

11. Khoa, N. T.; Kim, S. W.; Yoo, D.-H.; Kim, E. J.; Hahn, S. H., Size-dependent work function and catalytic performance of gold nanoparticles decorated graphene oxide sheets. *Appl. Catal. A* **2014,** *469*, 159-164.

12. Galilei, G., Two New Sciences, translated by Henry Crew and Alfonso de Salvio. Dover Publications, New York, NY, **1954**.

13. Brust, M.; Walker, M.; Bethell, D.; Schiffrin, D. J.; Whyman, R., Synthesis of thiol-derivatised gold nanoparticles in a two-phase Liquid–Liquid system. *J. Chem. Soc. Chem. Comm.* **1994,** (7), 801-802.

14. Goulet, P. J. G.; Lennox, R. B., New Insights into Brust−Schiffrin Metal Nanoparticle Synthesis. *J. Am. Chem. Soc.* **2010,** *132* (28), 9582-9584.

15. Saldan, I.; Semenyuk, Y.; Marchuk, I.; Reshetnyak, O., Chemical synthesis and application of palladium nanoparticles. *J. Mater. Sci.* **2015,** *50* (6), 2337-2354.

16. Cookson, J., The Preparation of Palladium Nanoparticles. *Platinum Met. Rev.* **2012,** *56* (2), 83-98.

17. Rivero, P. J.; Goicoechea, J.; Urrutia, A.; Arregui, F. J., Effect of both protective and reducing agents in the synthesis of multicolor silver nanoparticles. *Nanoscale Res. Lett.* **2013,** *8* (1), 101-101.

18. Roduner, E., Size matters: why nanomaterials are different. *Chem. Soc. Rev.* **2006,** *35* (7), 583-592.

19. Weckhuysen, B. M., Snapshots of a working catalyst: possibilities and limitations of in situ spectroscopy in the field of heterogeneous catalysis. *Chem. Commun.* **2002,** (2), 97-110.

20. Sankar, M.; Dimitratos, N.; Miedziak, P. J.; Wells, P. P.; Kiely, C. J.; Hutchings, G. J., Designing bimetallic catalysts for a green and sustainable future. *Chem. Soc. Rev.* **2012,** *41* (24), 8099-8139.

21. Narayanan, R.; El-Sayed, M. A., Shape-Dependent Catalytic Activity of Platinum Nanoparticles in Colloidal Solution. *Nano. Lett.* **2004,** *4* (7), 1343-1348.

22. Xue, T.; Lin, Z.; Chiu, C.-Y.; Li, Y.; Ruan, L.; Wang, G.; Zhao, Z.; Lee, C.; Duan, X.; Huang, Y., Molecular ligand modulation of palladium nanocatalysts for highly efficient and robust heterogeneous oxidation of cyclohexenone to phenol. *Sci. Adv.* **2017,** *3* (1), e1600615.

23. Niu, Z.; Li, Y., Removal and Utilization of Capping Agents in Nanocatalysis. *Chem. Mater.* **2014,** *26* (1), 72-83.

24. Kahsar, K. R.; Schwartz, D. K.; Medlin, J. W., Selective Hydrogenation of Polyunsaturated Fatty Acids Using Alkanethiol Self-Assembled Monolayer-Coated Pd/Al2O3 Catalysts. *ACS Catal.* **2013,** *3* (9), 2041-2044.

25. Corthey, G.; Rubert, A. A.; Picone, A. L.; Casillas, G.; Giovanetti, L. J.; Ramallo-López, J. M.; Zelaya, E.; Benitez, G. A.; Requejo, F. G.; José-Yacamán, M.; Salvarezza, R. C.; Fonticelli, M. H., New Insights into the Chemistry of Thiolate-Protected Palladium Nanoparticles. *J. Phys. Chem. C* **2012,** *116* (17), 9830-9837.

26. Chen, A.; Ostrom, C., Palladium-Based Nanomaterials: Synthesis and Electrochemical Applications. *Chem. Rev.* **2015,** *115* (21), 11999-12044.

27. Qiu, C.; Dong, X.; Huang, M.; Wang, S.; Ma, H., Facile fabrication of nanostructured Pd–Fe bimetallic thin films and their electrodechlorination activity. J. Mol. Catal. A: Chem. **2011,** *350* (1), 56-63.

28. Yao, Y.; Rubino, S.; Gates, B. D.; Scott, R. W. J.; Hu, Y., In situ X-ray absorption spectroscopic studies of magnetic Fe@FexOy/Pd nanoparticle catalysts for hydrogenation reactions. *Catal. Today* **2017,** *291*, 180-186.

29. Yao, Y.; Patzig, C.; Hu, Y.; Scott, R. W. J., In Situ X-ray Absorption Spectroscopic Study of Fe@FexOy/Pd and Fe@FexOy/Cu Nanoparticle Catalysts Prepared by Galvanic Exchange Reactions. *J. Phys. Chem. C* **2015,** *119* (36), 21209-21218.

30. Bansal, V.; O'Mullane, A. P.; Bhargava, S. K., Galvanic replacement mediated synthesis of hollow Pt nanocatalysts: Significance of residual Ag for the H2 evolution reaction. *Electrochem. Commun.* **2009,** *11* (8), 1639-1642.

31. da Silva, A. G. M.; Rodrigues, T. S.; Haigh, S. J.; Camargo, P. H. C., Galvanic replacement reaction: recent developments for engineering metal nanostructures towards catalytic applications. *Chem. Commun.* **2017,** *53* (53), 7135-7148.

32. Oh, M. H.; Yu, T.; Yu, S. H.; Lim, B.; Ko, K. T.; Willinger, M. G.; Seo, D. H.; Kim, B. H.; Cho, M. G.; Park, J. H.; Kang, K.; Sung, Y. E.; Pinna, N.; Hyeon, T., Galvanic Replacement Reactions in Metal Oxide Nanocrystals. *Science* **2013,** *340* (6135), 964-968.

33. Yin, Y.; Rioux, R. M.; Erdonmez, C. K.; Hughes, S.; Somorjai, G. A.; Alivisatos, A. P., Formation of Hollow Nanocrystals Through the Nanoscale Kirkendall Effect. *Science* **2004,** *304* (5671), 711-714.

34. Groppi, G.; Cristiani, C.; Lietti, L.; Ramella, C.; Valentini, M.; Forzatti, P., Effect of ceria on palladium supported catalysts for high temperature combustion of CH4 under lean conditions. *Catal. Today* **1999,** *50* (2), 399-412.

35. Ciuparu, D.; Bozon-Verduraz, F.; Pfefferle, L., Oxygen Exchange between Palladium and Oxide Supports in Combustion Catalysts. *J. Phys. Chem. B* **2002,** *106* (13), 3434-3442.

36. Ciuparu, D.; Perkins, E.; Pfefferle, L., In situ DR-FTIR investigation of surface hydroxyls on γ-Al2O3 supported PdO catalysts during methane combustion. *Appl. Catal. A* **2004,** *263* (2), 145-153.

37. Ciuparu, D.; Pfefferle, L., Support and water effects on palladium based methane combustion catalysts. *Appl. Catal. A* **2001,** *209* (1), 415-428.

38. Schwartz, W. R.; Ciuparu, D.; Pfefferle, L. D., Combustion of Methane over Palladium-Based Catalysts: Catalytic Deactivation and Role of the Support. *J. Phys. Chem. C* **2012,** *116* (15), 8587-8593.

39. Schwartz, W. R.; Pfefferle, L. D., Combustion of Methane over Palladium-Based Catalysts: Support Interactions. *J. Phys. Chem. C* **2012,** *116* (15), 8571-8578.

40. Fu, Q.; Wagner, T., Interaction of nanostructured metal overlayers with oxide surfaces. *Surf. Sci. Rep.* **2007,** *62* (11), 431-498.

41. Pan, C.-J.; Tsai, M.-C.; Su, W.-N.; Rick, J.; Akalework, N. G.; Agegnehu, A. K.; Cheng, S.-Y.; Hwang, B.-J., Tuning/exploiting Strong Metal-Support Interaction (SMSI) in Heterogeneous Catalysis. *J. Taiwan Inst. Chem. E* **2017,** *74*, 154-186.

42. Ioannides, T.; Verykios, X. E., Charge Transfer in Metal Catalysts Supported on Doped TiO2: A Theoretical Approach Based on Metal–Semiconductor Contact Theory. *J. Catal.* **1996,** *161* (2), 560-569.

43. Gonzalez-delaCruz, V. M.; Pereñiguez, R.; Ternero, F.; Holgado, J. P.; Caballero, A., In Situ XAS Study of Synergic Effects on Ni–Co/ZrO2 Methane Reforming Catalysts. *J. Phys. Chem. C* **2012,** *116* (4), 2919-2926.

44. Kalamaras, C. M.; Panagiotopoulou, P.; Kondarides, D. I.; Efstathiou, A. M., Kinetic and mechanistic studies of the water–gas shift reaction on Pt/TiO2 catalyst. *J. Catal.* **2009,** *264* (2), 117-129.

45. Mihai, O.; Smedler, G.; Nylén, U.; Olofsson, M.; Olsson, L., The effect of water on methane oxidation over Pd/Al2O3 under lean, stoichiometric and rich conditions. *Catal. Sci. Technol.* **2017,** *7* (14), 3084-3096.

46. Nassiri, H.; Lee, K.-E.; Hu, Y.; Hayes, R. E.; Scott, R. W. J.; Semagina, N., Platinum Inhibits Low-Temperature Dry Lean Methane Combustion through Palladium Reduction in Pd−Pt/Al2O3: An In Situ X-ray Absorption Study. *ChemPhysChem* **2017,** *18* (2), 238-244.

47. Burch, R.; Urbano, F. J.; Loader, P. K., Methane Combustion over Palladium Catalysts - the Effect of Carbon-Dioxide and Water on Activity. *Appl. Catal. A* **1995,** *123* (1), 173-184.

48. Kan, H. H.; Colmyer, R. J.; Asthagiri, A.; Weaver, J. F., Adsorption of Water on a PdO(101) Thin Film: Evidence of an Adsorbed HO−H2O Complex. *J. Phys. Chem. C* **2009,** *113* (4), 1495-1506.

49. Albers, P. W.; Mobus, K.; Wieland, S. D.; Parker, S. F., The fine structure of Pearlman's catalyst. *Phys. Chem. Chem. Phys.* **2015,** *17* (7), 5274-8.

50. Cullis, C. F.; Nevell, T. G.; Trimm, D. L., Role of the catalyst support in the oxidation of methane over palladium. *J. Chem. Soc., Faraday Trans. 1 F* **1972,** *68* (0), 1406-1412.

51. Kikuchi, R.; Maeda, S.; Sasaki, K.; Wennerström, S.; Eguchi, K., Low-temperature methane oxidation over oxide-supported Pd catalysts: inhibitory effect of water vapor. *Appl. Catal. A* **2002,** *232* (1), 23-28.

52. Burch, R.; Crittle, D. J.; Hayes, M. J., C–H bond activation in hydrocarbon oxidation on heterogeneous catalysts. *Catal. Today* **1999,** *47* (1), 229-234.

53. Nassiri, H.; Lee, K.-E.; Hu, Y.; Hayes, R. E.; Scott, R. W. J.; Semagina, N., Platinum Inhibits Low-Temperature Dry Lean Methane Combustion through Palladium Reduction in Pd−Pt/Al2O3: An In Situ X-ray Absorption Study. *ChemPhysChem* **2016,** *18* (2), 238-244.

54. Nassiri, H.; Lee, K.-E.; Hu, Y.; Hayes, R. E.; Scott, R. W. J.; Semagina, N., Water shifts PdO-catalyzed lean methane combustion to Pt-catalyzed rich combustion in Pd–Pt catalysts: In situ X-ray absorption spectroscopy. *J. Catal.* **2017,** *352*, 649-656.

55. Persson, K.; Jansson, K.; Järås, S. G., Characterisation and microstructure of Pd and bimetallic Pd–Pt catalysts during methane oxidation. *J. Catal.* **2007,** *245* (2), 401-414.

56. Coq, B.; Figueras, F., Bimetallic palladium catalysts: influence of the co-metal on the catalyst performance. *J. Mol. Catal. A: Chem.* **2001,** *173* (1), 117-134.

57. Nassiri, H.; Hayes, R. E.; Semagina, N., Tin Dioxide as an Alternative to Platinum Promoter in Palladium-Catalyzed Wet Lean Methane Combustion. *Top. Catal.* **2019,** *62* (1), 386-390.

58. Osman, A. I.; Abu-Dahrieh, J. K.; Laffir, F.; Curtin, T.; Thompson, J. M.; Rooney, D. W., A bimetallic catalyst on a dual component support for low temperature total methane oxidation. *Appl. Catal. B* **2016,** *187*, 408-418.

59. Konno, H., Chapter 8 - X-ray Photoelectron Spectroscopy. In *Materials Science and Engineering of Carbon*, Inagaki, M.; Kang, F., Eds. Butterworth-Heinemann: 2016; pp 153-171.

60. Metson, J. B., Charge Compensation and Binding Energy Referencing in XPS Analysis. *Surf. Interface Anal.* **1999,** *27*, 1069-1072

61. Jun Kawai, H. A., Yoshinori Kitajima, Kuniko Maeda, Shinjiro Hayakawa and Yohichi Gohshi, Inelastic Mean Free Path of Photoelectrons in Ag Determined by Total Reflection X-Ray Photoelectron Spectroscopy. *Anal. Sci.* **1997,** *13*, 797-801.

62. Carlson, T. A.; McGuire, G. E., Study of the x-ray photoelectron spectrum of tungsten—tungsten oxide as a function of thickness of the surface oxide layer. *J. Electron. Spectrosc. Relat. Phenom.* **1972,** *1* (2), 161-168.

63. Kim, K. J., Characteristics of synchrotron radiation. *AIR Conf. Proc.* **1989,** *184* (1), 565-632.

64. Bilderback, D. H.; Elleaume, P.; Weckert, E., Review of third and next generation synchrotron light sources. *J. Phys. B: At. Mol. Opt. Phys.* **2005,** *38* (9), S773-S797.

65. McRee, D. E., 2 - DATA COLLECTION TECHNIQUES. In *Practical Protein Crystallography (Second Edition)*, McRee, D. E., Ed. Academic Press: San Diego, 1999; pp 23-90.

66. McNaught, A. D.; Wilkinson, A.; Jenkins, A. D.; International Union of, P.; Applied, C., *IUPAC compendium of chemical terminology : the gold book*. International Union of Pure and Applied Chemistry: [Research Triangle Park, N.C.], 2006.

67. Newville, B. R. a. M., ATHENA, ARTEMIS, HEPHAESTUS: data analysis for X-Ray absorption spectroscopy using IFEFFIT. *J. Synchrotron Radiat.* **2005,** *12*, 537-541.

68. Goulon, J.; Goulon-Ginet, C.; Cortes, R.; Dubois, J. M., On experimental attenuation factors of the amplitude of the EXAFS oscillations in absorption, reflectivity and luminescence measurements. *J. Phys. France* **1982,** *43* (3), 539-548.

69. Henderson, G., The effects of absorption and self-absorption quenching on fluorescent intensities. *J. Chem. Educ.* **1977,** *54* (1), 57.

70. Trevorah, R. M.; Chantler, C. T.; Schalken, M. J., Solving self-absorption in fluorescence. *IUCrJ* **2019,** *6* (4), 586-602.

71. Tröger, L.; Arvanitis, D.; Baberschke, K.; Michaelis, H.; Grimm, U.; Zschech, E., Full correction of the self-absorption in soft-fluorescence extended x-ray-absorption fine structure. *Phys. Rev. B* **1992,** *46* (6), 3283-3289.

72. Newville, M., Fundamentals of XAFS. *Rev. Mineral. Geochem.* **2014,** *78* (1), 33-74.

73. Wagner, T.; Bauer, M.; Sauerwald, T.; Kohl, C. D.; Tiemann, M., X-ray absorption near-edge spectroscopy investigation of the oxidation state of Pd species in nanoporous SnO2 gas sensors for methane detection. *Thin Solid Films* **2011,** *520* (3), 909-912.

74. Müller, J. E.; Jepsen, O.; Wilkins, J. W., X-ray absorption spectra: K-edges of 3d transition metals, L-edges of 3d and 4d metals, and M-edges of palladium. *Solid State Commun.* **1982,** *42* (5), 365-368.

75. Singh, J.; Lamberti, C.; van Bokhoven, J. A., Advanced X-ray absorption and emission spectroscopy: in situ catalytic studies. *Chem. Soc. Rev.* **2010,** *39* (12), 4754-66.

76. Grunwaldt, J.-D.; Maciejewski, M.; Baiker, A., In situ X-ray absorption study during methane combustion over Pd/ZrO2 catalysts. *Phys Chem Chem Phys* **2003,** *5* (7), 1481-1488.

77. Bhatia, S.; Beltramini, J.; Do, D. D., Temperature programmed analysis and its applications in catalytic systems. *Catal. Today* **1990,** *7* (3), 309-438.

78. Ragaini, V.; Giannantonio, R.; Magni, P.; Lucarelli, L.; Leofanti, G., Dispersion measurement by the single introduction method coupled with the back-sorption procedure: A chemisorption and TPD study of the different chemisorbed hydrogen species: II. Pd on Alumina. *J. Catal.* **1994,** *146* (1), 116-125.

79. Prado-Burguete, C.; Linares-Solano, A.; Rodriguez-Reinoso, F.; De Lecea, C. S.-M., Effect of carbon support and mean Pt particle size on hydrogen chemisorption by carbon-supported Pt ctalysts. *J. Catal.* **1991,** *128* (2), 397-404.

80. Pérez, O.-L.; Romeu, D.; Yacamán, M. J., The relation between dispersion and particle size on supported catalysts. *J. Catal.* **1983,** *79* (1), 240-241.

81. Mehrabadi, B. A. T.; Eskandari, S.; Khan, U.; White, R. D.; Regalbuto, J. R., Chapter One - A Review of Preparation Methods for Supported Metal Catalysts. In *Advances in Catalysis*, Song, C., Ed. Academic Press: 2017; Vol. 61, pp 1-35.

82. Hansen, T. W.; DeLaRiva, A. T.; Challa, S. R.; Datye, A. K., Sintering of Catalytic Nanoparticles: Particle Migration or Ostwald Ripening? *Acc. Chem. Res.* **2013,** *46* (8), 1720-1730.

83. Dhall, S.; Kumar, M.; Bhatnagar, M.; Mehta, B. R., Dual gas sensing properties of graphene-Pd/SnO2 composites for H2 and ethanol: Role of nanoparticles-graphene interface. *Int. J. Hydrogen Energy* **2018,** *43* (37), 17921-17927.

84. Zhang, W.; Qin, Q.; Dai, L.; Qin, R.; Zhao, X.; Chen, X.; Ou, D.; Chen, J.; Chuong, T. T.; Wu, B.; Zheng, N., Electrochemical Reduction of Carbon Dioxide to Methanol on Hierarchical Pd/SnO2 Nanosheets with Abundant Pd–O–Sn Interfaces. *Angew. Chem. Int. Edit.* **2018,** *57* (30), 9475-9479.

85. Sekizawa, K.; Widjaja, H.; Maeda, S.; Ozawa, Y.; Eguchi, K., Low temperature oxidation of methane over Pd/SnO2 catalyst. *Appl. Catal. A* **2000,** *200* (1), 211-217.

86. Hou, Y.; Xu, Z.; Sun, S., Controlled synthesis and chemical conversions of FeO nanoparticles. *Angew. Chem. Int. Ed.* **2007,** *46* (33), 6329-32.

87. Kraus, W.; Nolze, G., POWDER CELL - a program for the representation and manipulation of crystal structures and calculation of the resulting X-ray powder patterns. *J. Appl. Crystallogr.* **1996,** *29* (3), 301-303.

88. Haynes, W. M., CRC Handbook of Chemistry and Physics: a Ready-Reference Book of Chemical and Physical Data. Raton, B., Ed. CRC Press: 2009.

89. Cho, S.; Yu, J.; Kang, S. K.; Shih, D.-Y., Oxidation study of pure tin and its alloys via electrochemical reduction analysis. *J. Electron. Mater.* **2005,** *34* (5), 635-642.

90. Giefers, H.; Porsch, F.; Wortmann, G., Kinetics of the disproportionation of SnO. *Solid State Ionics* **2005,** *176* (1), 199-207.

91. Schenk-Meuser, K.; Duschner, H., ESCA-Analysis of tin compounds on the surface of hydroxyapatite. *Fresnius J. Anal. Chem.* **1997,** *358* (1), 265-267.

92. Kövér, L.; Moretti, G.; Kovács, Z.; Sanjinés, R.; Cserny, I.; Margaritondo, G.; Pálinkás, J.; Adachi, H., High resolution photoemission and Auger parameter studies of electronic structure of tin oxides. *J. Vac. Sci. Technol. A* **1995,** *13* (3), 1382-1388.

93. Renard, D.; McCain, C.; Baidoun, B.; Bondy, A.; Bandyopadhyay, K., Electrocatalytic properties of in situ-generated palladium nanoparticle assemblies towards oxidation of multi-carbon alcohols and polyalcohols. *Colloids Surf., A* **2014,** *463*, 44-54.

94. Shen, Y.; Xu, Q.; Gao, H.; Zhu, N., Dendrimer-encapsulated Pd nanoparticles anchored on carbon nanotubes for electro-catalytic hydrazine oxidation. *Electrochem. Commun.* **2009,** *11* (6), 1329-1332.

95. Ye, H.; Scott, R. W. J.; Crooks, R. M., Synthesis, Characterization, and Surface Immobilization of Platinum and Palladium Nanoparticles Encapsulated within Amine-Terminated Poly(amidoamine) Dendrimers. *Langmuir* **2004,** *20* (7), 2915-2920.

96. Mäki-Jaskari, M. A.; Rantala, T. T., Density functional study of Pd adsorbates at SnO2(110) surfaces. *Surf. Sci.* **2003,** *537* (1), 168-178.

97. Mallard, P. J. L. a. W. G., NIST Chemistry WebBook, NIST Standard Reference Database Number 69. National Institute of Standards and Technology.

98. Torrente-Murciano, L., The importance of particle-support interaction on particle size determination by gas chemisorption. *J. Nanopart. Res.* **2016,** *18* (4), 87.

99. Fleisch, T. H.; Zajac, G. W.; Schreiner, J. O.; Mains, G. J., An XPS study of the UV photoreduction of transition and noble metal oxides. *Appl. Surf. Sci.* **1986,** *26* (4), 488-497.

100. Barrett, W.; Shen, J.; Hu, Y.; Hayes, R. E.; Scott, R. W. J.; Semagina, N., Understanding the role of SnO2 support in water-tolerant methane combustion: In

situ observation of Pd(OH)2 and comparison with Pd/Al2O3. *ChemCatChem* https://doi.org/10.1002/cctc.201901744.

101. Grosvenor, A. P.; Kobe, B. A.; Biesinger, M. C.; McIntyre, N. S., Investigation of multiplet splitting of Fe 2p XPS spectra and bonding in iron compounds. *Surf. Interface Anal.* **2004,** *36* (12), 1564-1574.

102. Cathles, L. M.; Brown, L.; Taam, M.; Hunter, A., A commentary on "The greenhouse-gas footprint of natural gas in shale formations" by R.W. Howarth, R. Santoro, and Anthony Ingraffea. *Climatic Change* **2012,** *113* (2), 525-535.

103. U.S. Energy Information Administration How much carbon dioxide is produced when different fuels are burned? https://www.eia.gov/tools/faqs/faq.php?id=73&t=11 (accessed October 1).

104. Gholami, R.; Alyani, M.; Smith, J. K., Deactivation of Pd Catalysts by Water during Low Temperature Methane Oxidation Relevant to Natural Gas Vehicle Converters. *Catalysts* **2015,** *5* (2), 561-594.

105. Zhang, F.; Hakanoglu, C.; Hinojosa, J. A.; Weaver, J. F., Inhibition of methane adsorption on PdO(101) by water and molecular oxygen. *Surf. Sci.* **2013,** *617*, 249-255.

106. Ciuparu, D.; Katsikis, N.; Pfefferle, L., Temperature and time dependence of the water inhibition effect on supported palladium catalyst for methane combustion. *Appl. Catal. A* **2001,** *216* (1), 209-215.

107. F. H. Ribeiro, M. C. a. R. A. D. B., Kinetics of the Complete Oxidation of Methane over Supported Palladium Catalysts. *J. Catal.* **1993,** *146*, 537-544.

108. Persson, K.; Ersson, A.; Jansson, K.; Iverlund, N.; Järås, S., Influence of co-metals on bimetallic palladium catalysts for methane combustion. *J. Catal.* **2005,** *231* (1), 139-150.

109. Ercolino, G.; Grzybek, G.; Stelmachowski, P.; Specchia, S.; Kotarba, A.; Specchia, V., Pd/Co3O4-based catalysts prepared by solution combustion synthesis for residual methane oxidation in lean conditions. *Catal. Today* **2015,** *257*, 66-71.

110. Wang, Y.; Toshima, N., Preparation of Pd−Pt Bimetallic Colloids with Controllable Core/Shell Structures. *J. Phys. Chem. B* **1997,** *101* (27), 5301-5306.

111. Hadia, N.; V. Ryabtsev, S.; Domashevskaya, E.; Seredin, P., *Investigation of Structural and Optical Properties of Powder Tin Oxide (SnOx) Annealed in Air*. Cond. Mat. and Inter., **2009,** 1, 10-15.

112. Potoczna-Petru, D.; Kępiński, L., Reduction study of Co3O4 model catalyst by electron microscopy. *Catal. Lett.* **2001,** *73* (1), 41-46.

113. Farrauto, R. J.; Hobson, M. C.; Kennelly, T.; Waterman, E. M., Catalytic chemistry of supported palladium for combustion of methane. *Applied Catalysis A: General* **1992,** *81* (2), 227-237.

114. Shimizu, K.-I.; Kamiya, Y.; Osaki, K.; Yoshida, H.; Satsuma, A., The average Pd oxidation state in Pd/SiO sub(2) quantified by L sub(3)-edge XANES analysis and its effects on catalytic activity for CO oxidation. *Catal. Sci. Technol.* **2012,** *2* (4), 767-772.

115. Tew, M. W.; Miller, J. T.; van Bokhoven, J. A., Particle size effect of hydride formation and surface hydrogen absorption of nanosized palladium catalysts : L_3 edge vs K edge x-ray absorption spectroscopy. *J. Phys. Chem. C* **2009,** *113* (34).

116. Stotz, H.; Maier, L.; Boubnov, A.; Gremminger, A. T.; Grunwaldt, J. D.; Deutschmann, O., Surface reaction kinetics of methane oxidation over PdO. *J. Catal.* **2019,** *370*, 152-175.

117. Ha, H.; Yoo, M.; An, H.; Shin, K.; Han, T.; Sohn, Y.; Kim, S.; Lee, S.-R.; Han, J. H.; Kim, H. Y., Design of Reduction Process of SnO2 by CH4 for Efficient Sn Recovery. *Sci. Rep.* **2017,** *7* (1), 14427.

118. Han, Z.; Guo, N.; Li, F.; Zhang, W.; Zhao, H.; Qian, Y., Solvothermal preparation and morphological evolution of stannous oxide powders. *Mater. Lett.* **2001,** *48* (2), 99-103.

119. Amatayakul, W.; Ramnäs, O., Life cycle assessment of a catalytic converter for passenger cars. *J. Clean. Prod.* **2001,** *9* (5), 395-403.

120. Heck, R. M.; Farrauto, R. J., Automobile exhaust catalysts. *Appl. Catal. A* **2001,** *221* (1), 443-457.